Fatigue Behaviour of a Barely Visible Impact Damaged Carbon Fibre Reinforced Epoxy Laminate

by

Alastair Komus

A Thesis submitted to the Faculty of Graduate Studies of

The University of Manitoba

in partial fulfillment of the requirements of the degree of

Master of Science

Department of Mechanical and Manufacturing Engineering

University of Manitoba

Winnipeg

ABSTRACT

Composite materials have high in-plane mechanical properties, but are susceptible to out-of-plane impact damage. The use of non-destructive evaluation techniques, combined with mechanical testing, was investigated to characterize the progression of post-impact static and fatigue damage of composite laminates. Quasi-isotropic carbon/epoxy specimens were impacted at energy levels of 35 J and 50 J. The initial damage was characterized using ultrasonic C-scan and thermography. Residual strength testing revealed that the compressive static strength of the test specimens was reduced by over 50%. Digital image correlation was used to characterize the growth of damage and the local strain during compression-compression fatigue tests. Initially, no significant statistical trend could be measured when the fatigue data was plotted as a stress-life curve. When stress concentration factors were used to calculate and plot the local stress amplitude, a correlation with fatigue life was observed. The undamaged fatigue data was altered using damage factors which allowed for post-impact fatigue life predictions.

ACKNOWLEDGEMENTS

I would like to acknowledge the following organizations and people for their support in completing this project.

- National Sciences and Engineering Research Council of Canada and Boeing Canada Technology for their financial support
- University of Manitoba Mechanical and Manufacturing Engineering Department's technical staff
- Daniel Godin and the Industrial Technology Centre for their testing assistance
- Chad Ulven from North Dakota State University for lending the ASTM 7137 fixture
- Saeed Nojavan and Raymond Wong from Boeing for their technical advice
- Andrew Johnston, Yunfa Zhang, Marc Genest, and the National Research Council Canada – Institute for Aerospace Research for producing the ultrasonic C-scan and thermography images, as well as providing technical guidance
- Sean McKay, Michael Hudek, and the rest of the staff at the Composites Innovation Centre for their advice and support
- Eugene Rothwell at the Composites Innovation Centre for his help preparing the specimens
- Eugene Manchur, Loren Hendrickson, and Boeing Canada Technology for their technical assistance
- Mark Shead from Boeing Canada Technology for his help in preparing and testing the specimens and acting as technical liaison with Boeing
- Dr. Meera Singh for acting as my advisor for this study and providing extremely valuable input and feedback throughout this project
- Finally, to all of my family and friends who have constantly supported me during this process

TABLE OF CONTENTS

LIST OF TABLES

LIST OF FIGURES

ABBREVIATIONS AND SYMBOLS

DIC – Digital Image Correlation

CFRP – Carbon Fibre Reinforced Plastic

CAI – Compression After Impact

FEA – Finite Element Analysis

GFRP – Glass Fibre Reinforced Plastic

CDS – Characteristic Damage State

S-N – Stress-Life

CLC – Combined Loading Compression

DAQ – Data Acquisition

P_E – Potential energy (J)

m_h – Mass of the hail (kg)

V_r – Resultant velocity (m/s)

V_t – Terminal velocity (m/s)

V_w – Wind velocity (m/s)

r – Radius (m)

H – Drop height (m)

m_d – Mass of the impactor (kg)

g – Acceleration of gravity (m/s^2)

B_y – Percent bending (%)

ε_f – Strain recorded by the front gauge

ε_b – Strain recorded by the back gauge

S – Stress (MPa)

P – Applied load (N)

w – Specimen gauge width (m)

t – Specimen gauge thickness (m)

E_X – Longitudinal modulus (GPa)

E_Y – Transverse modulus (GPa)

$\varepsilon_{x,3000}$ – Actual measured longitudinal strain closest to 3000 με

$\varepsilon_{y,3000}$ – Actual measured transverse strain that corresponds to $\varepsilon_{x,3000}$

$\varepsilon_{x,1000}$ – Actual measured longitudinal strain closest to 1000 με

$\varepsilon_{y,1000}$ – Actual measured transverse strain that corresponds to $\varepsilon_{x,1000}$

P_{3000} – Applied load at $\varepsilon_{x,3000}$ (N)

P_{1000} – Applied load at $\varepsilon_{x,1000}$ (N)

ν_{xy} – Poisson's ratio

G_{xy} – Shear modulus (GPa)

γ_{5500} – Actual measured engineering shear strain closest to 5500 με

γ_{1500} – Actual measured engineering shear strain closest to 1500 με

P_{5500} – Applied load at $\gamma_{x,5500}$ (N)

P_{1500} – Applied load at $\gamma_{x,1500}$ (N)

d_l – Width across the notch (m)

A_D – Damage area (mm^2)

S_{ult} – Ultimate compressive strength (MPa)

P_{MAX} – Maximum applied force (N)

A – Cross-sectional area

E_{CAI} – Effective compressive modulus (GPa)

S_{CAI} – Compression after impact strength (MPa)

SCFε – Strain concentration factor

ε_{local} – Strain at the damage location

$\varepsilon_{farfield,DIC}$ – Far-field strain as measured by the DIC system

$SCF\varepsilon_{linear}$ – Linear strain concentration factor

$SCF\sigma$ – Stress concentration factor

d – Damage depth (mm)

R – Stress ratio (S_{MIN} / S_{MAX})

ε_a - Axial strain

N – Number of cycles

S_{MAX} – Maximum applied stress (MPa)

S_{MIN} – Minimum applied stress (MPa)

S_a – Stress amplitude (MPa)

S_{Norm} – Normalized stress

N_{imp} – Fatigue life of impacted specimen

N_f – Fatigue life of undamaged specimen

σ_o – Strength of unimpacted laminate

σ_R – Residual strength of impacted laminate

σ_{max} – Maximum applied stress level

$S_{a,\ local}$ – Local stress amplitude

1 BACKGROUND AND INTRODUCTION

A composite is the combination of two or more materials of different properties to form a new material that has enhanced properties. Usually a composite material consists of fibres and a resin. The fibres provide strength to the composite, especially in tension. The resin, or matrix, holds the fibres together and transfers the load to the fibres. The matrix also plays an important role in the compression and shear strength of the composite.

A variety of materials are used as fibres in composite materials. They include glass, carbon, Kevlar, ceramics, and recently bio-based fibres including flax and hemp. Common thermoset resins include varieties of polyester, vinyl ester, and epoxy. There are also many types of thermoplastic resins that include polyethylene, polystyrene, polypropylene, and polyetheretherketone. Different combinations of fibres and resin have varying cost, density, strength, stiffness, electrical properties, and thermal properties.

Composite materials are produced by a variety of methods. Liquid resin that has been combined with a catalyst can be applied to raw fibres by hand or by resin transfer moulding and then allowed to cure. In the aerospace industry pre-preg material is often used. In this form, the fibres are embedded by the manufacturer in the resin which has already been partially cured. This results in slightly tacky flat plies that can be laid up next to and on top of each other. The specimen is then usually cured under heat and pressure in an autoclave.

Fibre reinforced composites are a relatively new and developing material. One of the problems with the use of composites, unlike their metal counterparts, is that there is a lack of historical design data. As well, reliable analytical tools are not yet fully developed. Instead, extensive physical testing of material coupons, components, and assemblies is conducted to characterize the material's mechanical behaviour. These test programs are costly and time consuming. Accurate analysis tools would allow for multiple iterations early in the design phase and reduce costs.

Composite materials are increasingly being used in primary structural components in the aerospace industry. This is primarily due to their high strength-to-weight ratio and the ability to tailor their mechanical properties. Initially composite materials were only used in the secondary structure of aircraft, including fairings, ailerons, elevators, and the rudder. Now composite materials are being used in primary structures that include the horizontal tail, vertical fin, wing box, and fuselage. A prime example is the Boeing 787 Dreamliner that uses 50% composite materials by weight.

With the increased use of composite materials in aerospace structures, the analysis and prediction of the post-impact static and fatigue behaviour of composites has become a critical concern. Although composite materials have very high in-plane mechanical properties, they are susceptible to out-of-plane impact damage. Impact damage can be caused by a variety of sources. In aerospace structures, such damage can be a result of hail, ballistics, runway debris, and tool drop. Numerous authors have shown that the damage caused by impacts can have a severe effect on the in-plane properties of composite laminates. Often the damage on the surface is invisible or barely visible to the eye, but the internal damage may be severe.

When a part is loaded and then unloaded in a repetitive fashion it is said to be undergoing fatigue loading. Fatigue loading is inherent in all aircraft structures undergoing ground-air-ground loading cycles throughout their service life. Parts may fail after repeated cyclic loading, even when the applied loads are below the ultimate strength of the material. Fatigue damage initiates at cracks, delaminations, and other stress concentrations that are caused by impact loads. With repeated loading the cracks and delaminations grow until a critical damage size is reached. At this point failure often occurs suddenly, with little or no warning, lowering the service life of the aircraft component relative to an undamaged part. For safety reasons, it is critical that parts are analyzed and tested for durability under this type of loading.

Post -impact fatigue damage of composite materials can be difficult to predict because the damage appears in a variety of forms. This can include matrix cracking, delaminations, fibre-matrix debonding, and fibre breakage. Researchers have attempted to provide analytical tools to describe impact and fatigue damage of composite materials and their effects using a variety of techniques that include continuum damage mechanics, fracture mechanics, and empirical methods.

As stated above, impact damage and the corresponding damage from fatigue loading can often severely affect the properties of a part without being visible to the eye. Non-destructive testing techniques allow engineers to observe the internal characteristics of the damage without having to destroy the part. These methods can provide critical insight into the modes and growth of damage in composite laminates. A multitude of inspection methods have been tested including ultrasonic C-scan, thermography, digital image correlation, X-ray radiography, acoustic emission, thermoelastic stress analysis,

electronic speckle pattern interferometry, and shearography. There is a great deal of promise in using the information gathered from these non-destructive evaluations, in conjunction with analytical techniques, to predict the remaining fatigue life of a component.

The objective of the current research project was to experimentally examine how barely visible impact damage affects the static and fatigue properties of carbon fibre reinforced epoxy composites. Analytical models that characterize the progression of post-impact fatigue damage and make use of results from non-destructive inspections and mechanical properties were also evaluated.

A 24 ply quasi-isotropic lay-up of carbon fibre reinforced epoxy pre-preg was chosen for static and fatigue testing because this material and lay-up are commonly used in aerospace structures. The quasi-isotropic laminates were impacted at two energy levels, 35 J and 50 J, with a drop weight impact tester to represent barely visible impact damage that may be caused by tool drop or hail. Non-destructive test methods that included ultrasonic C-scan and thermography were used to characterize the length, width, diameter, and area of the damage. Static compressive tests were performed on both undamaged and damaged panels to determine the residual compressive modulus and strength of the laminates after impact. The static test results were compared to the non-destructive evaluation data to determine if there was a relationship between the damage area and residual strength.

Compression-compression fatigue tests were performed on undamaged specimens to understand the fatigue behaviour of this material and lay-up and to determine the

fatigue limit. Fatigue tests were also performed on damaged laminates to see how the post-impact fatigue life compared to the fatigue life of the undamaged specimens.

Two methods from the literature, detailed in Section 2.4, were examined for their suitability for post-impact fatigue life predictions of the chosen material and laminate stacking sequence. The first method normalized the post-impact fatigue data using the residual strength of the damaged specimens. The second method relies on residual strength data, as well as fatigue results from undamaged specimens. Finally, stress concentration factors calculated from strains measured by digital image correlation were used to correlate the post-impact fatigue behaviour of the damaged carbon/epoxy laminates.

The following chapters describe the work completed during this research project. Chapter 2 provides an overview of the relevant literature regarding the static and fatigue performance of impact damaged composite laminates. Chapter 3 describes the experimental setup, including the material and specimen fabrication, required test equipment, and test procedures. Chapter 4 presents the results and corresponding discussion for the mechanical property evaluation, drop-weight impact testing, and static and fatigue testing of both the undamaged and damaged specimens. Chapter 5 summarizes the testing, results, and conclusions, and also explains potential future work.

2 LITERATURE REVIEW AND THESIS OBJECTIVES

In this chapter the literature that is relevant to this project is examined and the objectives of the thesis are outlined. In the first section the characterization of impact damage is discussed including damage forms and analytical models that describe the damage. In the next section models that describe the relationship between impact energy levels and residual strength are examined. The third section describes how damage forms and progresses during fatigue cycling and provides information on models that describe these processes. The next section brings together many of the ideas from the first three sections and discusses post-impact fatigue damage progression and models that are used to predict the fatigue life of impacted laminates. At the end of this chapter conclusions from the literature review are stated and then the thesis objectives are detailed.

2.1 Characterizing Impact Damage

A number of authors have examined the effects of low-velocity impacts on composite laminates. Buggy and McNamara [1] tested $[+45/-45]_{4S}$ carbon/epoxy specimens after impact and showed that the damage envelope through the thickness of the specimen was in the shape of a cone with the largest extent of damage near the back face. They also demonstrated that a threshold level of impact energy exists below which no impact damage occurs.

Tai et al. [2] used ultrasonic C-scan on carbon/epoxy composites and showed that the damage zone size increased with an increase in energy. Siow and Shim [3] performed tests on woven carbon/epoxy specimens and observed that the damage area varied

linearly with impact energy. They also found that a small diameter impactor caused more delamination than a blunt impactor.

Other researchers have examined ways of improving the impact resistance of composite laminates. Moon and Kennedy [4] found that dry preform stitching significantly improved the damage tolerance and damage resistance properties of carbon/epoxy composites. Cantwell et al. [5] concluded that the inclusion of a woven lamina improved the impact resistance of a laminate.

Non-destructive testing methods have been used to characterize impact damage in composite laminates. Amaro et al. [6] compared the ability of three different types of non-destructive testing to characterize damage in carbon/epoxy specimens. They found that electronic speckle pattern interferometry and shearography were not as accurate as the ultrasonic C-scan method. However, the C-scan technique requires a coupling agent and does not provide great information in terms of the depth of the damage in the specimen. Genest et al. [7] showed that pulsed thermography can be used to detect disbonds in composite bonded repairs. They also found that the results had similar accuracy to ultrasonic pulse-echo C-scan inspection.

Russell et al. [8] showed that flaws and impact damage appeared as anomalies in the strain and displacement fields produced by digital image correlation (DIC) for glass/epoxy specimens undergoing tensile loading. Bisagni and Walters [9] used a digital image correlation system to map strains during the biaxial static compression testing of carbon/epoxy specimens. They found that delamination propagation, fibre breakage, and fibre-matrix shear failure contributed to the failure of the specimen. Stelzer et al. [10]

showed that the major strain amplitude as measured by DIC corresponded well with the major strain amplitude measured by thermoelastic stress analysis.

There has also been an effort to find ways of analytically modelling impact damage. Delfosse and Poursartip [11] found that the area of delamination after impact was much larger for a brittle laminate than for a tough laminate, but the amount of fibre damage was comparable. The authors proposed that an energy balance for impacted carbon fibre reinforced plastic (CFRP) consists of three terms; elastically stored energy, energy absorbed in creating matrix damage, and energy absorbed in creating fibre damage. The amount of energy absorbed in creating matrix and fibre damage can be calculated from the total matrix damage area, total fibre damage area, and energy release rates.

Kim and Kedward [12] showed that a progression of failure modes exist, starting with delamination, when ice is impacted into a composite laminate. They also were able to create a numerical simulation that successfully modelled ice impacting a structure.

Williams et al. [13] developed a continuum damage mechanics model for use in finite element software to predict damage growth and its effects on the response of laminated composites. It is based on two phases. In the first phase matrix cracking and delamination is dominant, while both matrix and fibre damage growth is observed in the second phase.

2.2 Post-Impact Residual Strength

Many researchers have examined the relationship between impact damage and residual strength. Saito and Kimpara [14] observed a linear relationship between impact energy level and compression after impact (CAI) strength for a multi-axial stitched CFRP laminate. Siow and Shim [3] showed that both the tensile and compressive residual strengths decreased with an increase in impact energy for woven carbon/epoxy specimens. However the authors noted that tensile residual strength was dependent on both delamination area and the amount of fibre breakage whereas the compressive residual strength was only dependent on the delamination area. They also found that the compressive residual strength was lower than the tensile residual strength for a given impactor mass and size.

Dost et al. [15] found that laminate stacking sequence was critical to compression after impact strength. They concluded that the CAI strength was negatively affected when plies of the same orientation were grouped together. They also found that the asymmetry of the damage through the thickness increased during these cases. The data was then examined using a sublaminate stability analysis to find the effective reduced stiffness of the impact damage zone. A stress concentration associated with the reduced stiffness was calculated and then a maximum strain failure criteria was applied to predict CAI strength. The authors found that for specimens with a relatively symmetric distribution of damage through the laminate thickness the model worked well. They also found that $[45/90/-45/0]_{3S}$ stacking sequence had relatively high CAI strength.

Hitchen and Kemp [16] also studied the effect of stacking sequence on impact damage of carbon/epoxy laminates. They found that 45 degree surface plies increased the energy required to initiate delamination. The initiation energy was also increased by increasing the number of dissimilar interfaces within the laminate. More energy was required to initiate delamination so there was less energy for delamination extension. This resulted in the total delamination area being smaller in laminates with 45 degree surface plies. CAI strength decreased as the maximum delamination area increased but no relation between the two factors was determined. As well, the CAI strength did not show any trend with the surface ply orientation or the number of dissimilar interfaces.

The residual tensile strength of an impacted specimen was analyzed by Husman et al. [17] by converting the impact damage to an equivalent crack of known dimensions and using a fracture mechanics model. Avva and Padmanabha [18] found that the compressive residual strength of an impacted carbon/epoxy specimen could be modelled using linear elastic fracture mechanics if the undamaged strength, threshold level, and the residual strength at a few velocities were measured.

Caprino [19] also used a model based on linear elastic fracture mechanics to predict the tensile residual strength of CFRP laminates. He found that the tensile residual strength was related to the impact energy. He stated that the tensile residual strength could be predicted by performing a static force-displacement test to measure the applied energy and by knowing the unnotched strength of the laminate. Found et al. [20] confirmed Caprino's model for residual tensile and compressive strength of a woven carbon/epoxy laminate. Ding et al. [21] also confirmed Caprino's model.

Some authors have modelled the residual strength by modelling the damage as a soft inclusion and examining local buckling. El-Zein and Reifsnider [22] modelled the damage zone as an elliptical inclusion. They measured the dimensions of the damage area using ultrasonic C-scan and used the results to reduce the average effective stiffness in that region. This data was then used as an input into the stress analysis of an elastic inclusion. The authors concluded that the high sensitivity of composite specimens to impact damage is due to the high stress concentration value that is caused by the abrupt change in elastic properties at the damage zone and not by the loss of strength at the damage region.

An analytical method to predict residual compressive strength was developed by Xiong et al. [23]. Their model is based on the largest sublaminate near the back surface of the specimen buckling, which is followed by the buckling of other sublaminates in the damage area. This results in a reduction in the elastic modulus at the damage area and causes the load to be redistributed to undamaged areas. This causes a stress concentration to develop at the edge of the damage and reduces the compressive strength of the specimen. Using this knowledge the authors simulated the impact damage as an elliptical soft inclusion.

Nyman et al. [24] however found that modelling the damage as a soft inclusion with conservative assumptions of stiffness reduction resulted in unconservative predictions of residual strength. The authors observed that the residual strength of carbon/epoxy laminates damaged by low-velocity impact could be accurately predicted using delamination buckling theory coupled with an approximation of the strain energy release rate. The damage was characterized by measuring the projected area by C-scan.

Then the energy release rate of one delamination that buckled was calculated. The delamination was placed at different interfaces through the thickness of the laminate and the failure load was calculated as the lowest load at which a delamination would grow.

Soutis and Curtis state in Ref. [25] that carbon/epoxy specimens fail in compression due to mircrobuckling of the fibres. They adapted a fracture toughness model [26] originally developed to estimate the notched compressive strength of plates with an open circular hole to predict the compressive residual strength of impact damaged specimens. The model requires knowledge of the unnotched strength, damage width, and the compressive in-plane fracture energy. The fracture energy is determined from a separate experiment on a laminate with a sharpened long slit. This model is extended in Ref. [27] where the unnotched strength is predicted using the matrix shear strength, fibre waviness, and kink band inclination angle.

Wang et al. [28] used a finite element analysis (FEA) to model low-velocity impact damage and tensile residual strength of carbon fibre composites. The analysis showed that the degradation of strength could be divided into three stages based on the impact energy levels. Matrix shear cracking occurs at low energy levels. The matrix cracks result in a stress concentration and decrease the residual strength of the specimen. In stage two the residual tensile strength is relatively constant over a large range of impact energy levels. Damage is mainly in the form of matrix cracks and delaminations and not fibre failure. During stage three the fibres begin to break and this causes a severe reduction in the residual strength because the tensile strength of the composites is mainly dependent on the tensile strength of the fibres.

A damage mechanics model developed by Papanicolaou and Stavropoulos [29] assumes that the degradation of the flexural stiffness of a damaged laminate is related to the residual compressive strength. It uses a bending stiffness mismatching coefficient which expresses the bending stiffness difference between two adjoining plies. Empirical parameters are derived from a graph of the normalized residual strength versus the impact energy. The results of the model are correlated based on the percentage of +/- 45 degree plies.

In Ref. [30] Neveb-Hashemi et al. found that the elastic moduli, strength, and toughness properties of carbon/epoxy specimens varied linearly when a laminate was impacted repeatedly. It was found that attenuation changes in the ultrasonic signal were not a good parameter for estimating the degradation of properties. However the stress wave factor proved to be a good parameter for predicting the residual strength of the laminates after impact.

2.3 Fatigue of Undamaged Composites

Research efforts are underway to understand the fatigue process of undamaged composite laminates. Varvani-Farahani et al. [31] state that in compression-compression fatigue loading the fatigue life will decrease with an increase in the load ratio, R, the ratio of the minimum applied load over the maximum applied load. They also found that during tension-compression and tension-tension fatigue loading of glass fibre reinforced plastic (GFRP) the fatigue strength decreased as stress ratio was increased.

However, Kawai and Suda [32] found that for tension-tension and tension-compression fatigue loading decreasing the stress ratio decreased the fatigue strength of carbon/epoxy laminates at multiple off-axis angles. They developed a damage mechanics model to describe the stress ratio effect on the off-axis fatigue behaviour of unidirectional carbon/epoxy laminates with non-negative mean stress. Epaarachchi and Clausen [33] also found this to be true for GFRP laminates. They also state that increasing frequency increases the fatigue life as long as the temperature rise due to hysteresis is not significant.

A number of authors have attempted to describe the damage progress during fatigue loading. Poursartip et al. [34] demonstrated that damage accumulation during fatigue loading could be described by a damage function. The damage has an initial value and increases during cycling until the final damage level is reached and fast fracture occurs. The damage function was calculated based on measurements of the change in modulus.

Xiong and Shenoi [35] state that the fatigue damage process could be divided into two stages. The first stage consisted of damage formation while the second stage consisted of damage propagation. In the first stage multiple matrix cracks develop along fibres in off-axis plies. These cracks then link up by debonding the ply-ply interfaces. In the second stage delaminations grow and coalesce leading finally to fibre breakage in the longitudinal plies. They found that during the damage formation stage there is negligible effect on the stiffness of the specimen, but during the damage propagation stage the stiffness rapidly decreases. They developed a mathematical model based on phenomenological methodology and continuum damage mechanics for compressive

fatigue loading of notched and unnotched specimens and found that the model was conservative when compared with experimental data.

Haque et al. [36] also found that tensile residual strength and stiffness degradation was insignificant during the first 50% of cycles when matrix cracking in the transverse plies was the primary damage mode.

Plumtree and Shen [37] described a similar damage progression as [35]. The first stage displays a decelerating rate of damage that is described by a two-parameter Weibull model. The second stage demonstrates an accelerating rate of damage that is modelled using continuum damage mechanics. The results of these two stages can be summed together in order to model the entire fatigue process. The first stage finishes and the second begins when the characteristic damage state (CDS) is reached. This occurs when the decelerating rate of damage from the first stage is equal to the accelerating rate of damage from the second stage.

Varvani-Farahani et al. [31] described similar damage mechanisms but separated the damage progression during fatigue loading of GFRP laminates into 3 stages. The initial damage forms as micro-cracks within the matrix during the first 20% of life. These cracks tend to form at defects such as misaligned fibres and resin rich areas. The cracks grow and multiply in this region until they reach a fibre. In the second stage damage continues to grow and appears as fibre-matrix debonding. This eventually leads to the last stage where fibre fracture occurs during a short time period. The proposed model calculates an energy-based parameter that incorporates stress and strain within the

calculations. This parameter helps to describe the energy dissipation that occurs as a composite specimen suffers fatigue damage.

Toubal et al. [38] used thermography techniques to measure the temperature increase in carbon/epoxy specimens during tension-tension fatigue testing. They found that the increase in temperature matched the damage profile as measured by the decrease in Young's modulus. They also found that the damage evolution was split into three stages. In the first stage damage grows rapidly due to the occurrence of multiple damage modes. In the second stage the damage steadily and slowly increases. In the final stage the damage grows rapidly due to the fracture of fibres.

The 3-stage damage accumulation model was also found to be true for uniaxial tensile fatigue testing of nylon fibre-reinforced elastomer matrix composites in Ref. [39]. As well, Mao and Mahadevan [40] developed a damage accumulation model that is used to describe all three stages of damage during tensile fatigue testing.

Azouaoui et al. [41] showed that damage evolution also occurred in three stages for repeated impact loading of a glass/epoxy laminate. The stages are similar as for the tensile and compressive fatigue loading cases. In the first stage the delamination process initiates and the delaminations grow. In the second stage delamination saturation appears, meaning that the creation of new delaminated areas stops. In the last stage ply cracking and fibre breakage occurs.

Steinberger et al. [42] tested two thermographic techniques for damage characterization during tensile fatigue loading. They found that a passive thermographic approach could be used to measure the temperature increase due to hysteretic heating of a

CRFP laminate. The damage could be quantified by calculation of a loss factor via the hysteretic heating. The second technique that they utilized was an active method which utilized pulse thermography with photothermal heating to characterize the impact damage by changes in heat conduction. The measured change of heat conductivity was small and requires further research.

Liu and Lessard [43] provide four choices for predicting the fatigue life under tension-tension loading. The four choices include residual modulus, matrix-cracking criterion, delamination area criterion, and residual strength. The required constants are found by performing fatigue tests on unidirectional laminates.

A residual stiffness model of woven glass/epoxy laminates undergoing bending fatigue was developed by Van Paepegem and Degrieck [44]. Xiong et al. [45] developed a residual strength model that is based on fatigue strains. Kim and Hwang [46] showed that the change of maximum impact force in a laminate is related to the decrease in stiffness during fatigue testing. They then used a residual stiffness versus cycles curve to predict the remaining fatigue life of the specimen.

Work has also been performed to model two-stage fatigue loading in composites. Epaarachchi and Clausen [47] developed a fatigue damage accumulation model for GFRP composites undergoing discrete loading. Damage was defined based on strength degradation. The results of the model matched well with experimental results for 2 step tension-tension and fully reversed loading. The model also appears promising for use with CFRP laminates. Gao [48] developed a nonlinear cumulative damage model that used the stiffness reduction properties of a critical laminae to predict the failure of the

laminate under 2-stage loading. The model was tested on graphite/epoxy cross-ply laminates under tension-tension fatigue loading. Whitworth [49] developed a phenomenological cumulative damage model that is based on a residual stiffness model to predict the fatigue life of composite specimens undergoing multi-stress level fatigue loading.

In Ref. [50] Hwang and Han defined fatigue modulus as the slope of applied stress and resultant strain at a specific fatigue cycle. They assumed that the fatigue modulus degradation rate followed a power function of fatigue cycle. The degradation rate combined with strain failure criterion was used to predict the fatigue life of glass fibre reinforced epoxy specimens. They extended their damage model to two-step loading in Ref. [51].

The creation of stress-life (S-N) curves to describe the fatigue life of composite specimens has been used by some researchers. Conle and Ingall [52] found that plots of maximum stress (S_{MAX}) and stress amplitude (S_a) versus number of cycles often showed a large amount of data scatter. They found that plotting $\sqrt{S_{MAX}S_a}$ for specimens that fail in tension and plotting $-\sqrt{|S_{MAX}|S_a}$ for compressive failures helped to correlate the data.

Gao and Reifsnider [53] used a micromechanics approach to create S-N curves for E-glass/epoxy specimens under tensile fatigue loading. Rotem [54] used the S-N curves of tension-tension and compression-compression fatigue tests to predict the fatigue behaviour of graphite/epoxy laminates under any stress ratio. In Ref. [14] the S-N curve of a tension-compression fatigue test at three energy levels of a multi-axial stitched CFRP laminate did not show a linear relationship.

Kawai and Koizumi [55] developed a method to create constant fatigue life diagrams based on experiments that determine the static tensile and compressive strengths, and the S-N curve at a critical stress ratio. The critical stress ratio is defined as the static compression strength over the static tensile strength. The peak alternating stress on the diagram occurs at the critical stress ratio. The shape of the curves in the constant life diagram change from straight lines to nonlinear curves that can be estimated as parabolas as the fatigue life is increased.

Some authors have examined the use of Miner's sum, popular for metallic fatigue, to analyse cumulative fatigue damage in composites caused by loading at multiple stress levels. Broutman and Sahu [56] showed that for E-glass/epoxy laminates undergoing dual-level tension-tension fatigue testing the Miner's sum was greater than 1 for a high-low stress test and less than 1 for low-high stress test. They explained these observations based on the reduction of the tensile strength during fatigue cycling and developed a new theory to predict the cumulative fatigue damage.

Noda et al. [57] applied the statistical linear cumulative damage rule to predict the flexural fatigue life of CFRP laminates undergoing variable frequency and loading amplitudes. They found that the conservative linear cumulative damage rule was not applicable for the CFRP laminates, but the statistical linear cumulative damage rule was applicable.

Epaarachchi and Clausen [33] developed an empirical based fatigue model for GFRP that is applicable for both tension-tension and compression-compression fatigue loading. It considers the effects of both stress ratio and frequency on fatigue life.

Material constants are determined from a few fatigue tests at a constant stress ratio and varying stress levels.

Andersons et al. [58] used a fracture mechanics approach to estimate the growth rate of delamination at various stress ratios based on the test results at one stress ratio. The model was compared to experimental results for unidirectional laminates with a variety of reinforcements under both mode I and mode II loading. Fujii and Maekawa [59] developed a model for tension fatigue of fibre reinforced composites that uses linear elastic fracture mechanics.

O'Brien et al. [60] developed a methodology to predict fatigue life under tension-tension loading. The delamination behaviour under fatigue was characterized in conjunction with strain energy release rates and stiffness loss measured in real time. The increase in global strain resulting from the decrease in stiffness was compared to the decrease in laminate failure strain caused by the formation of delaminations in order to predict laminate fatigue failure.

2.4 Post-Impact Fatigue

A number of researchers have focused their studies on the post-impact fatigue process of composites. There is some debate regarding which stress ratio is the most severe for impact damaged laminates. Melin et al. [61] concluded that during tension-compression fatigue loading of impact damaged carbon/epoxy specimens, the compressive part of the cycle had a larger role in failure then the tensile part. Similarly, Ding et al. [21] found that tension-compression loading (R = -1) had a more negative

effect on fatigue life than tension-tension loading (R = 0). They also observed that impact followed by load cycling was more damaging than cycling followed by impact.

Rosenfeld and Gause [62] found that tension-compression loading of graphite/epoxy laminates with R = -1 was worst then for compression-compression loading with R = 0. However, both showed significant reductions in fatigue life when compared to tension-tension fatigue testing. Beheshty et al. [63] observed that the effects of impact damage on carbon/epoxy and glass/epoxy specimens were more severe for compression-compression fatigue loading then for tension-compression loading.

Buggy and McNamara [1] showed that the tension-tension fatigue life of carbon/epoxy specimens was reduced when impact energy exceeded the minimum threshold energy level to cause damage. No changes in residual strength or fatigue life were observed for impact energy levels below the threshold value.

Some authors have found that the tensile residual strength of damaged specimens increased after fatigue cycling. Cantwell et al. [5] stated that the residual strength of impact damage carbon/epoxy laminates increased after tension fatigue cycling. Found et al. [20] also observed an increase in residual tensile strength after fatigue loading.

Ambu et al. [64] performed tension-tension fatigue tests on CFRP samples while examining them using digital image correlation. They found that DIC was a useful method for clarifying the roles of different failure modes on the residual properties of notched samples and providing insight into the mechanisms of damage development and strain distribution around a hole.

Ha et al. [65] performed tension-tension fatigue tests on short fibre notched GFRP laminates. They found that the stress concentration at the notch tip was relieved when the short fibres were aligned in the direction parallel to loading due to multiple crack initiations. However the stress concentration was increased when the fibres were aligned in the perpendicular direction.

For carbon/epoxy laminates, median rank and Weibull distribution were used to describe the failure probabilities under both monotonic and tension-tension fatigue loading by Tai et al. [2]. After impact, the number of fatigue life cycles until failure was reduced as well as the scatter in the data. It was found that stiffness increased in the early stages of fatigue testing but then decreased. The rate of decreasing stiffness increased with increasing stress level. For tension-compression fatigue testing of CFRP, Symons and Davis [66] found that there was a slow decrease in coupon modulus as the test proceeded. They also found that the delamination area as measured by C-scan increased very little as the test proceeded.

Mitrovic et al. [67] performed residual and fatigue tests on graphite/epoxy specimens. They discovered that for two-stage loading the high/low testing sequence causes more damage than the low/high. The authors also state that delamination growth governs the fatigue response and when the delamination area doesn't grow the fatigue life doesn't change. However, they stated that overall delamination area alone does not represent a reliable damage parameter for residual strength. The extent of damage through the thickness is also required. The researchers also found that residual compressive strength was diminished by impact, but did not further decrease after fatigue loading.

Krafchak et al. [68] performed a limited number of compression-compression fatigue tests on impact damaged composite tubes. They found that very little damage growth or change in stiffness occurred during the testing. They also found that the fatigue lives of identical tubes with impact damage varied greatly. The failure modes of the tubes included a combination of delamination buckling and shear crippling.

Katerelos et al. [69] calculated the strain energy release rate that corresponds to the propagation of delaminations during fatigue testing using the experimentally defined dimensions of the delamination as measured by ultrasonic C-scan. The model predicts the direction of delamination propagation as well as the weakest interface.

For two different types of CFRP, Uda et al. [70] found that the delamination area was larger and the residual compressive strength was lower for the material with the lower toughness value. It was observed that the specimens with the tougher resin were less likely to fail due to propagation of delaminations during compression fatigue testing, and more likely to fail by kink banding within individual laminae at a stress concentration.

Rosenfeld and Gause [62] found that the failure mode during primarily compressive fatigue loading was local failure of the matrix near the stress raiser that caused fibre splitting, delamination, and finally fibre buckling. They also found that the size of delaminations, as measured by C-scan, did not grow during axial compressive fatigue cycling for impact damaged CFRP laminates.

Freitas and de Carvalho [71] measured delamination growth during compressive fatigue testing of CFRP's using ultrasonic C-scanning. They found that the compressive

residual strength of carbon/epoxy specimens with circular holes drilled into them, could be predicted based on the damage size. They were able to establish a correlation between the area of delamination, fatigue life, and residual strength.

Minak et al. [72] used acoustic emission techniques to measure the damage progression during quasi-static transverse loading of carbon/epoxy specimens. The authors were then able to relate the tensile fatigue residual strength of damaged specimens to the tensile fatigue strength of undamaged specimens.

Attia et al. [73] used a finite element model to predict the strain energy release rate of an impact damaged CFRP skin/stringer panel. The strain energy release rate was then used to predict cycles to failure based on experimental fracture-mechanics data.

Butler et al. [74] developed an analytical model that can be used to predict the compressive fatigue limit strain of a carbon/epoxy laminate that contains barely visible impact damage. The damage is represented by a single circular delamination and the strain is calculated at which thin-film buckling of the region occurs. The fatigue limit strain is then defined as the strain at which the strain energy release rate of the thin post-buckled region is equal to the critical mode I value of the resin.

A few authors have attempted to create models to predict the fatigue life of impact damaged composite laminates. Melin et al. [61] determined that predictions of static compressive failure strain and fatigue limit were improved when the buckling area as measured by digital image correlation was used instead of the damage area measured by C-scan. They found that the S-N curve for damaged laminates under tension-compression loading, drawn by connecting the quasi-static strength with the fatigue limit

load, were conservative when compared to experimental results. However, they found that no statistically significant correlation could be found between damage size and the fatigue life of impact damaged carbon/epoxy laminates.

Yuanjian and Isaac [75] developed a residual strength model for an impact damaged stitched glass material. The tension-tension fatigue data at multiple impact energy levels were normalized using their residual strength and this caused the data to collapse onto a single S-N curve. Fatigue life predictions could therefore be made by knowing the residual strength of the damaged specimen and the S-N curve of undamaged specimens. The authors also found that low energy impact affected the tensile properties of the matrix dominated 45 degree lay-up, but a larger impact energy was required to affect the tensile properties of the fibre dominated 0/90 degree lay-up.

Kang and Kim [76] developed a fatigue life prediction model for impact damaged carbon/epoxy laminates under constant amplitude tension-tension loading using residual strength and unimpacted fatigue life data. The model was based on Broutman and Sahu's two-stage loading model [56]. The strength reduction due to the first stage of loading was replaced by the residual strength of the laminate after impact. The residual strength was solved for using Caprino's model [19]. It was found that these specimens exhibited a threshold impact energy level below which no degradation of residual strength was observed. The unimpacted fatigue life was modelled using Hwang's equation [50]. The authors performed a statistical analysis of the results and showed that the scattering of fatigue life was reduced as impact energy increased. They attributed this result to the stress concentration caused by the impact damage.

Kang and Kim successfully extended their model [77] to cover the case of two-stage tension-tension loading by using Broutman and Sahu's model under three-stage loading. The authors also developed a method [78] for predicting the fatigue life of impact damaged laminates undergoing variable amplitude loading. An equivalent constant amplitude stress is calculated based on the residual strength of the impacted laminate and the constant amplitude fatigue data of the unimpacted laminate.

Harris et al. [79] developed an empirical based fatigue life prediction model that is valid for CFRP. The authors found that there is a relationship between the alternating and mean component of stress and the data can be used to create constant-life diagrams across a range of stress ratios. The model is based on the static tensile and compressive strengths of the laminate and three empirical parameters. Two of the parameters have relatively constant values for a given class of material and lay-up, but the third parameter appears to be related to the ratio of compressive over tensile strength [63].

Beheshty and Harris extended the model [80] to cover impact damaged laminates. They found that low levels of impact energy had minimal effect on the tensile residual strength of carbon/epoxy laminates, but had a significant effect on the compressive residual strength. They concluded that this was due to delaminations at low energy levels reducing the shear and compression strengths. The tensile strength is not affected until greater energy levels that cause fibre breakage are applied. Plots of the impact damaged constant-life diagram showed a substantial change in the left hand quadrant (compression dominated) when compared to the undamaged plot. The right hand side (tension dominated) showed very little change.

Horn et al. [81] created a fatigue prediction model for tension-tension fatigue of impact damaged glass reinforced laminates using thermoelastic stress analysis. A small amplitude sinusoidal load was applied to an impact damaged specimen while the temperature distribution of the specimen was monitored using an infrared camera. The stress tensor at the damaged region, as measured by thermoelastic stress analysis, was compared to the farfield stress tensor to create a modified stress concentration factor. When the applied stress was plotted against cycles to failure for 3 different impact energies, no correlation could be found in the data. However, when the applied stress values were multiplied by the modified stress concentration factor the data collapsed onto a single S-N curve. The results were found to be slightly conservative when compared to the baseline data. The authors proposed that this non-destructive method could be applied in the field by using in-service vibration loads.

The authors also found that impact damaged laminates had a shorter fatigue lifetime then those laminates that contained a circular hole [82]. They attributed this to the fact that impacted laminates only needed to propagate cracks while the circular notched samples spent a significant number of cycles nucleating cracks.

2.5 Conclusions of the Literature Review

From the literature, it can be concluded that a threshold level of impact energy exists below which no impact damage will occur in a composite laminate. At energy levels above the threshold limit, damage will appear in a variety of modes that include matrix cracking, delamination, and at higher energy levels, fibre breakage.

A variety of non-destructive techniques have been used to observe damage in composite specimens. Ultrasonic C-scan has been successful at measuring the delamination area but does not provide any information about how the damage varies through the thickness of the specimen. Both digital image correlation and thermography have been used to help characterize the damage and strain patterns caused by impact damage. However, little work has been done to directly correlate the non-destructive test data with fatigue life predictions.

Barely visible impact damage that may be very difficult to observe with the naked eye can cause a severe reduction in the residual strength of a laminate. Researchers found that the tensile residual strength after impact was dependent on both delamination area and the amount of fibre breakage whereas the compressive residual strength was only dependent on the delamination area. They also found that the compressive residual strength was lower than the tensile residual strength for a given impactor mass and size.

Many researchers have observed that there are 3 stages of damage accumulation during the fatigue of undamaged composites. For this reason there are a multitude of cumulative damage models available in the literature. Attempts have also been made to correlate the fatigue data using S-N curves, as well as models based on empirical and fracture mechanics methodologies.

When studying the fatigue of impact damaged composites all researchers appear to agree that the compression part of the fatigue cycle is more severe then the tensile portion. However there is some disagreement over whether compression-compression or tension-compression loading is the worst case.

A small number of models, based on a variety of methods, have been developed to predict the post-impact fatigue life of composite specimens. One method is an empirical model that used a relationship between the alternating and mean component of stress to predict fatigue life at any stress ratio. Another method used the residual strength to normalize the tension-tension fatigue data of damaged specimens. The data from multiple impact energy levels collapsed onto a single S-N curve after the normalization process. A third model used the residual strength of the specimen, as predicted by Caprino [19], and unimpacted fatigue life data, to predict the post-impact life during constant amplitude tension-tension loading. The final model used a stress concentration factor measured by thermal elastic stress analysis to collapse the tension-tension fatigue data onto a single S-N curve. Post-impact life predictions could then be made based on the undamaged fatigue curve.

Only one of the methods examined compressive fatigue cycling despite the fact that, as stated previously, the compression part of the fatigue cycle is more severe then the tensile portion for impact damaged laminates. As well, only one model used data gained through non-destructive testing techniques to predict post-impact fatigue life.

2.6 Thesis Objectives

The literature review has shown that barely visible impact damage can severely affect the static and fatigue properties of composite laminates. However there is currently no consensus on how best to model the post-impact fatigue behaviour and damage progression. The objective of this study is to examine the effects of barely visible impact damage on carbon fibre reinforced epoxy composites under static and

fatigue loading conditions and to use non-destructive testing techniques to predict their fatigue life.

A 24 ply quasi-isotropic lay-up of carbon fibre reinforced epoxy pre-preg was chosen for static and fatigue testing because this material and lay-up are commonly used in aerospace structures. The tests were performed under compressive loading due to the fact that many authors have concluded that compression loading is more severe then tensile loading for both static and fatigue tests of impacted laminates.

The quasi-isotropic laminates were impacted at two energy levels, 35 J and 50 J, with a drop weight impact tester to represent barely visible impact damage that may be caused by tool drop or hail. Non-destructive test methods that included ultrasonic C-scan and thermography were used to characterize the height, width, and area of the damage. Static compressive tests were performed on both undamaged and damaged panels to determine the residual modulus and strength of the laminates after impact. Previous research has indicated that compressive residual strength is dependent on the damage area. Therefore, the static test results were compared to the non-destructive evaluation data to determine if there was a relationship between the damage area and residual strength.

Compression-compression fatigue tests were performed on undamaged specimens to understand the fatigue behaviour of this material and lay-up and to determine the fatigue limit. Fatigue tests were also performed on damaged laminates to see how the post-impact fatigue life compared to the fatigue life of the undamaged specimens.

Two methods currently available in the literature were examined for their suitability for post-impact fatigue life predictions of the chosen material and laminate stacking sequence. The first method was developed by Yuanjian and Isaac [75] who normalized the post-impact fatigue data using the residual strength of the damaged specimens. The second method was developed by Kang and Kim [76] and relies on residual strength data, as well as fatigue results from undamaged specimens. Finally, stress concentration factors calculated from strains measured by digital image correlation were used to correlate the post-impact fatigue behaviour of the damaged carbon/epoxy laminates in a method similar to Horn et al. [81].

3 EXPERIMENTAL SETUP

To achieve the objectives stated in Chapter 2, a variety of experiments were performed. Tests included the creation of impact damage, ultrasonic C-scan and thermographic non-destructive inspection, evaluation of the ply mechanical properties, static residual strength testing, and fatigue testing. This chapter provides descriptions of the specimens, equipment, and test procedures used during this study. In the first section the material and specimen fabrication are discussed. In the second section each piece of equipment is described. In the last section the test procedures for each of the tests listed above are detailed.

3.1 Material and Specimen Fabrication

3.1.1 Material and Lay-up Schedules

The material that was tested was a toughened 180°C epoxy with Toray T800 unidirectional carbon fibre reinforcement. The examination of this material is important as it is used in aircraft primary structural components. The test specimens for static and fatigue testing consisted of a quasi-isotropic, 24 ply stacking sequence of $[+45/90/-45/0]_{3S}$. Two different lay-up sequences were required to test for the lamina properties of the material. To determine the longitudinal and transverse modulus of the individual plies of the material, a $[0]_{16}$ unidirectional stacking sequence was chosen. A $[+45/-45]_{4S}$ lay-up was selected to test for the shear modulus properties of the material.

3.1.2 Panel Fabrication

Two quasi-isotropic panels measuring 1524 mm by 914.4 mm were manufactured at the Winnipeg plant of Boeing Canada Technology. Two additional panels were fabricated. The $[0]_{16}$ panel had dimensions of 330.2 mm by 304.8 mm, and the $[+45/-45]_{4S}$ panel measured 457.2 mm by 304.8 mm. All four panels were laid up by hand using the same technique.

The roll of unidirectional pre-preg tape had a width of 304.8 mm. The material was cut into appropriate lengths depending on the dimensions of each panel and laid onto an aluminum caul plate by hand at the proper orientation angle. This process is shown in Figure 3.1. When a joint occurred in a ply that had the same orientation angle as a previous ply, the location of the joint was offset by 25.4 mm from the previous ply of the same orientation angle. The same location for a joint wasn't used until 6 plies at the same orientation angle had been laid up.

Figure 3.1 – Pre-Preg Material Laid Up on Aluminum Caul Plate

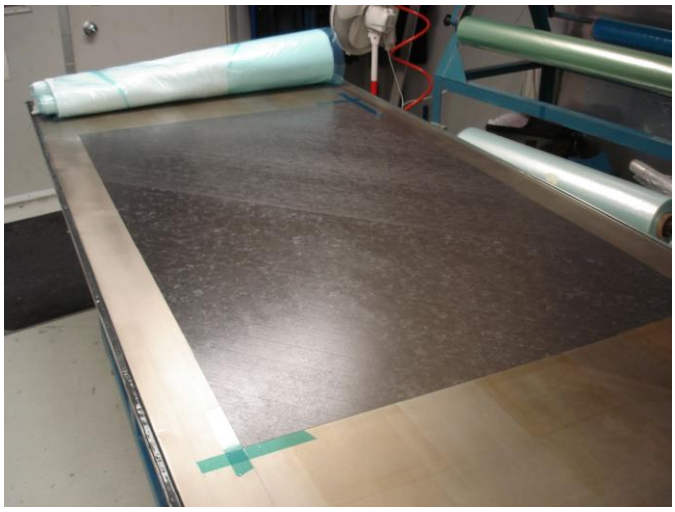

After the panel lay-up was completed the caul plate was covered by release film, breathing material, and a disposable bag. Figure 3.2 shows the panel after the vacuum was applied. Once it was ensured that the vacuum seals were secure the panels were subjected to a 2 hour, 180°C, 586 kPa vented autoclave cure. After curing, the panels were examined using Boeing Canada Technology's ultrasonic C-scan to ensure that no obvious defects were present.

Figure 3.2 – Vacuum Applied During Laminate Manufacture

3.1.3 Test Specimen Trimming and Dimensions

Rough cutting of the specimens from the panels was performed using either a carbide grit band saw or diamond grit wheel. The final dimensions of the test specimens were cut using a computer numerical controlled machine. In order to reduce scatter in the test data many of the tolerances for these test specimens were very small and required the use of diamond grit tooling.

The tests described in the following sections required different size test specimens. The dimensions and number of specimens for each test are summarized in Table 3.1.

Table 3.1 – Summary of Test Specimen Dimensions

Test	Lay-Up	Length (mm)	Width (mm)	Thickness (mm)	Number of Specimens
Longitudinal Modulus	$[0]_{16}$	139.7	12.7	3.1	5
Transverse Modulus	$[90]_{16}$	139.7	12.7	3.1	5
Shear Modulus	$[0/90]_{4S}$	76.2	55.9	3.1	5
Undamaged Static Compression	$[+45/90/-45/0]_{3S}$	139.7	12.7	4.7	5
Damaged Static Compression	$[+45/90/-45/0]_{3S}$	152.4	101.6	4.6	5 per energy level
Undamaged Fatigue Compression	$[+45/90/-45/0]_{3S}$	139.7	12.7	4.6	17
Damaged Fatigue Compression	$[+45/90/-45/0]_{3S}$	152.4	101.6	4.6	16 per energy level

Figure 3.3 shows the 139.7 mm by 12.7 mm rectangular specimen used to test the $[0]_{16}$ panel for the longitudinal and transverse modulus of the plies as described in Sections 3.3.3.1 and 3.3.3.2. This same size of test specimen was cut from the quasi-isotropic panel and used for static and fatigue testing of undamaged specimens described in Sections 3.3.4.1 and 3.3.5.1.

Figure 3.3 – Undamaged Test Specimen Dimension (mm)

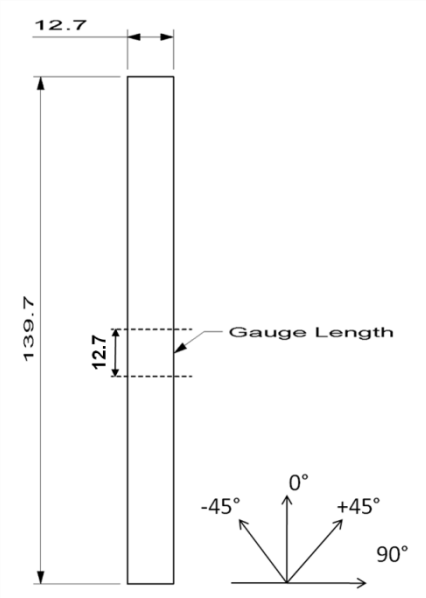

The 76.2 mm by 55.9 mm rectangular V-notched specimen cut from the $[0/90]_{4S}$ panel and used for shear modulus testing as will be explained in Section 3.3.3.3 is shown in Figure 3.4.

Figure 3.4 – Shear Test Specimen Dimensions (mm)

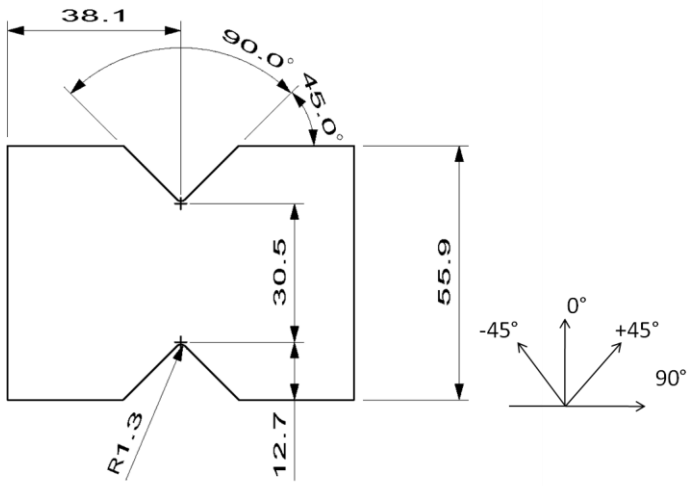

Finally, the 152.4 mm by 101.6 mm rectangular specimen used for the impacted static and fatigue tests of the quasi-isotropic panels described in Sections 3.3.4.2 and 3.3.5.2 is shown in Figure 3.5.

Figure 3.5 – Damaged Test Specimen Dimensions (mm)

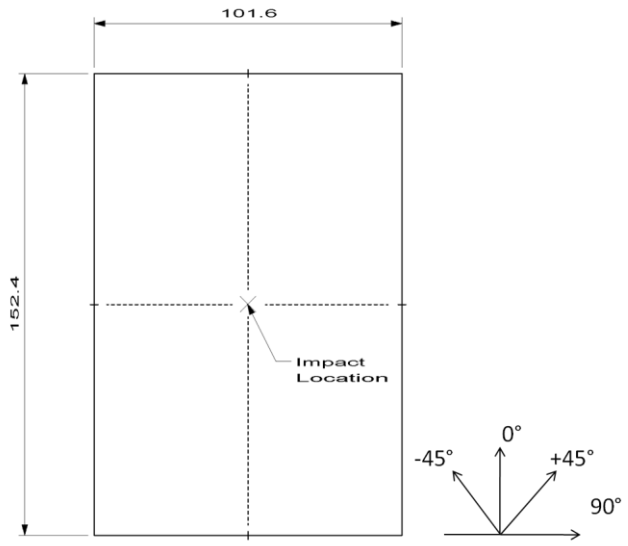

3.2 Test Equipment

In order to perform the testing a variety of equipment was required. The main equipment included a drop-weight impact tester, ultrasonic C-scan and thermography scanners, Instron 8822 servohydraulic load frame, a variety of compression and shear test fixtures, digital image correlation system, and the Vishay 7000 data acquisition system. Details on each piece of equipment are provided in the following sections.

3.2.1 Drop-Weight Impact Tester

The drop-weight impact device, shown in Figure 3.6, consisted of two guide rails on which the impactor mass slid. The impactor had a mass of 3.355 kg and a smooth

hemispherical striker tip with a diameter of 25.4 mm. The impact support fixture is shown in Figure 3.7. The support fixture had a cut-out of 75 mm by 125 mm and the specimen was centred and secured over the cut-out using four rubber tipped clamps.

Figure 3.6 – Drop-Weight Impact Device

Figure 3.7 – Impact Support Fixture

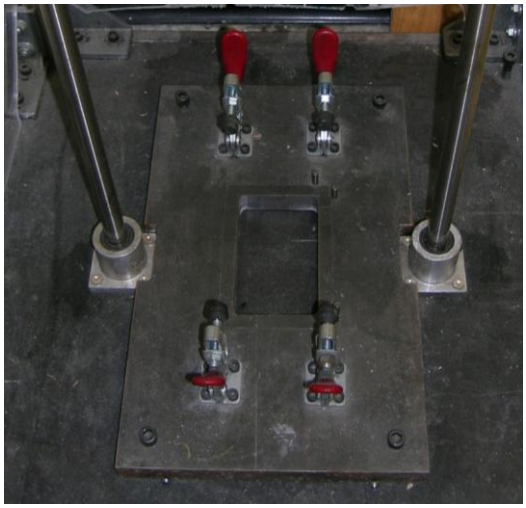

3.2.2 Non-Destructive Evaluation

The impacted specimens were inspected before static and fatigue testing using two non-destructive evaluation techniques. The ultrasonic C-scan and pulsed thermography equipment is described below.

3.2.2.1 Ultrasonic C-Scan

The ultrasonic inspections were carried out at the National Research Council Canada – Institute for Aerospace Research in Ottawa, ON. The scans were performed using an automated seven axis ultrasonic immersion system in pulse-echo mode, with step and index increments of 0.102 cm. The samples were inspected using a 2.25 MHz 0.635 cm diameter transducer with a 7.62 cm focus and full waveform data, containing 492 points, was recorded at 100 MHz.

3.2.2.2 Pulsed Thermography

The pulsed thermography inspections were also performed at the National Research Council Canada – Institute for Aerospace Research in Ottawa, ON. The tests used a 240x320 pixels infrared camera that had a thermal sensitivity of 20 mK at 303 K and a spectral response in the long wave infrared from 8.0 to 8.8 μm. Two xenon flash lamps, each powered by a 2400 J power supply, were used as energy sources. Each sample was inspected from both front and back surfaces, and each thermogram contained 740 frames that were acquired at 20 Hz.

3.2.3 Load Frame

The majority of mechanical tests were performed using the Instron 8822 servohydraulic load frame [83] shown in Figure 3.8. The load frame is capable of applying an axial force of ±250 kN and a torsional force of ±2.5 kN·m. The load frame contains collet grips shown in Figure 3.9 that are suitable for gripping cylindrical or tubular specimens.

Figure 3.8 – Instron 8822 Servohydraulic Load Frame

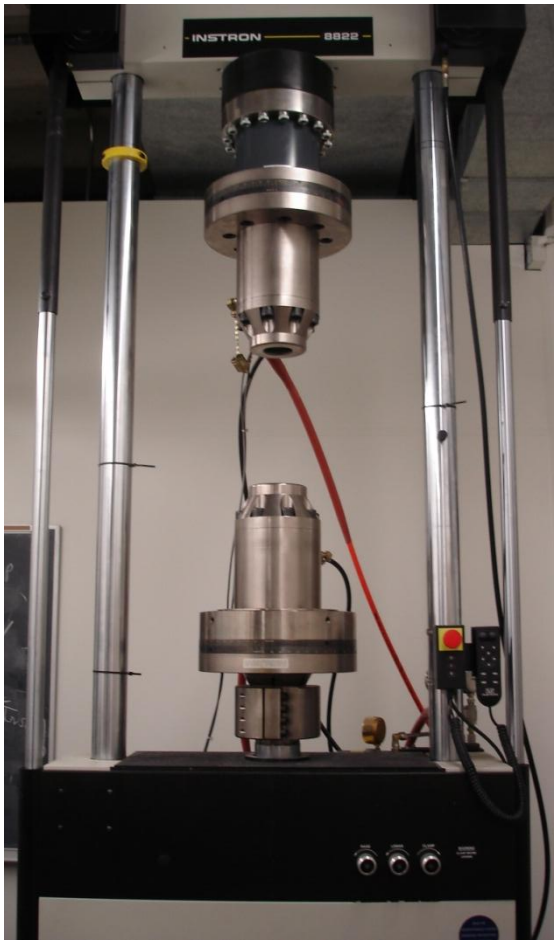

Figure 3.9 – Collet Grips

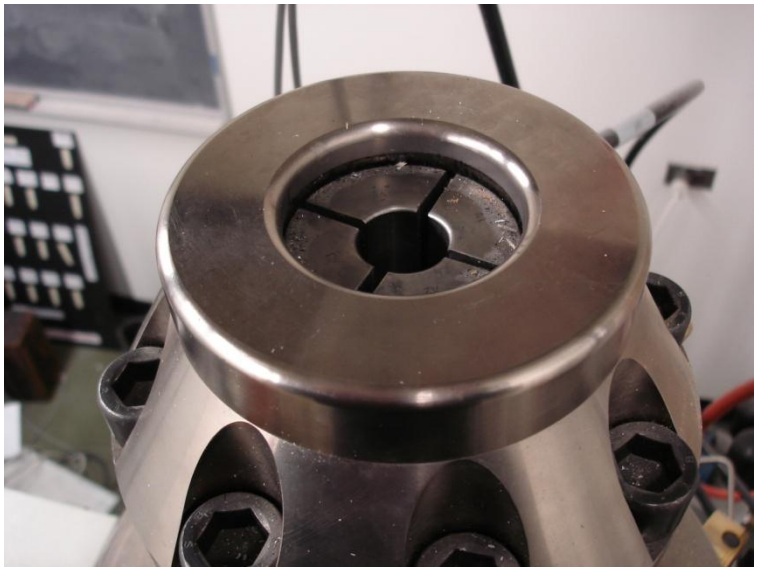

Inputs to the load frame were entered using the Instron 8800 control panel. For safety considerations maximum and minimum limits were set on both the applied loads and displacements before each test. The load frame could be operated in either load or position control with a variety of ramp rates or wave signals available depending on the desired loading configuration.

During the testing two parameters that affected the control loop had to be adjusted depending on the test setup. During loading the waveform generator produces a demand signal output that is compared to the actual applied load. The difference between these two values is the error signal and is used to adjust the system in order to correct the error [84]. The proportional gain amplifies the error signal before it is applied to the servovalve. A higher proportional gain will increase the accuracy of the system. However, if the value is too high the system will become unstable and unwanted vibrations will appear in the loading signal. The lag setting applies a phase lag to the signal.

For all position control tests the proportional gain was set between 40 and 42, and the lag was set to 0.8 ms. For the fatigue testing of damaged specimens under load control the proportional gain was set between 14 and 15, and the lag set to 0.8 ms. The loads applied during the undamaged fatigue tests were at the low end of the load cell's capability and decreased the accuracy of the response. To compensate for this, the proportional gain was increased to between 23 and 24. The lag value was also increased and was set to 5.0 ms.

3.2.4 Load Frame Fixtures

Fixed compression platens were required in order to perform compression testing on non-cylindrical specimens and can be seen in Figure 3.10. The 152.4 mm diameter platens were made from fully heat-treated tool steel and were chrome plated in order to provide high surface hardness, durability, and corrosion resistance [85]. Shallow concentric rings were engraved on the surface to help centre the test fixtures. The platens were equipped with a 25.4 mm diameter adapter to interface with the cylindrical grips of the load frame.

Figure 3.10 – Fixed Compression Platens

The combined loading compression test fixture is shown in Figure 3.11. This fixture applies a controllable ratio of end loading to shear loading into the specimen depending on the amount of torque applied to the clamping screws. This fixture was used for all tests of the 139.7 mm by 12.7 mm rectangular specimens.

Figure 3.11 – Combined Loading Compression Test Fixture

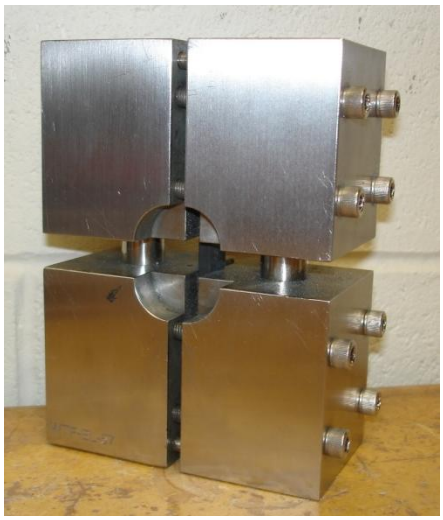

The V-notched rail shear test fixture is shown in Figures 3.12 and 3.13. Each half of the fixture had a side rail and two gripping plates. Each gripping plate was tightened by three bolts. Figure 3.12 also shows the white spacer blocks that were used to maintain alignment when installing the specimen.

Figure 3.12 – V-Notched Rail Shear Fixture and Spacer Blocks

Figure 3.13 – V-Notched Rail Shear Fixture Assembled

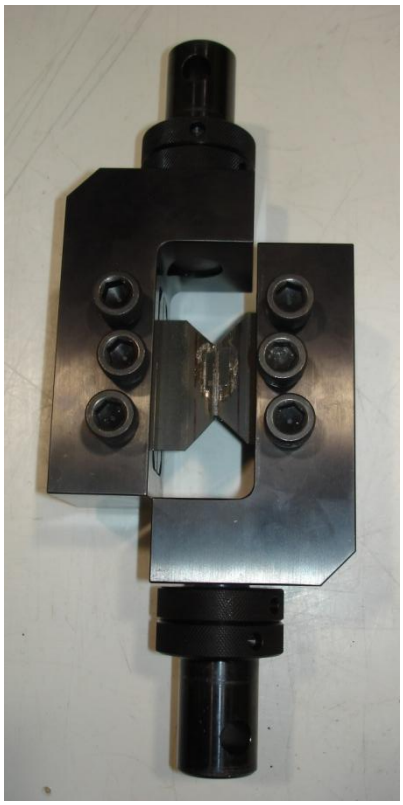

The fixture used for the compression after impact testing is shown in Figure 3.14. The fixture is designed so that the adjustable retention plates support the specimen edges and inhibit buckling as the specimen is end-loaded. Local out-of-plane rotation is not prevented by the knife edges of the side supports. Some rotational restraint is provided by the top and bottom supports due to the fixture geometry but these supports provide no clamp-up. The gripping length of the top, bottom, and side plates is 7.6 mm.

Figure 3.14 – Compression After Impact Fixture

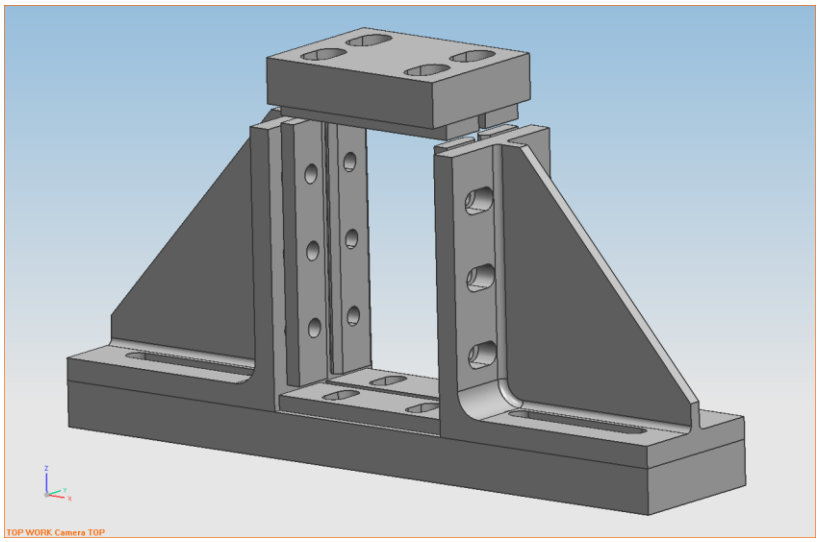

3.2.5 Strain Measurement

In the vicinity of simple surface strain fields, strains were measured using strain gauges. Strain gauge types were selected based on the testing performed and are described in the procedures section. The measurement of strains in the vicinity of the damage was conducted using a digital image correlation device called the ARAMIS [86].

The ARAMIS digital image correlation system shown in Figure 3.15 provides three dimensional non-contact measurements of deformation fields and surface strain fields. In order to use the system a random speckle paint pattern of white and black dots,

as seen in Figure 3.16, is applied to the test specimen using spray paint. Two high resolution charge coupled device cameras are used to capture images of the specimen as it deforms. Care must be taken to sufficiently illuminate the test specimen to obtain clear images, but also avoid heating the specimen. After the test is completed the ARAMIS software tracks each pixel as it moves in the captured images. This allows the software to produce a map of the specimen deformation. The analysis software then allows the user to track the deformation and surface strain fields as the test progresses.

Figure 3.15 – ARAMIS Digital Image Correlation System

Figure 3.16 – Speckle Paint Pattern

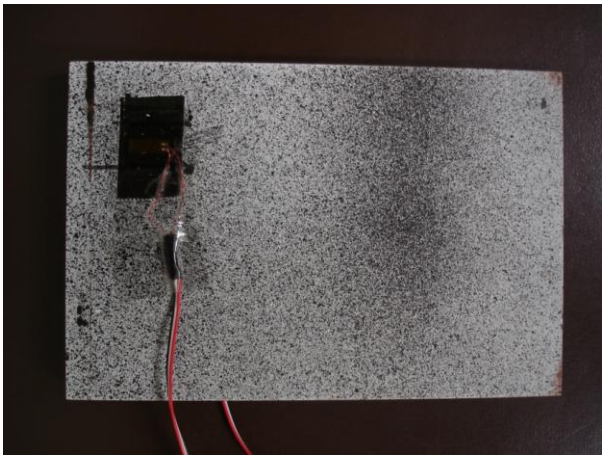

Apart from the sample prep described above, in general, the following steps are taken in using the system.

3.2.5.1 Calibration

In order to produce accurate results the cameras must be positioned correctly and calibrated before running a test. The camera positions are decided based on the desired size of the field of view. For these tests the cameras were positioned 225 mm from each other on the camera bar and the tripod was located 500 mm from the specimen. This resulted in a field of view of 60 by 45 by 30 mm.

A calibration panel was then placed at the specimen location. As shown in Figure 3.17, the calibration panel consists of a rectangular grid of small white dots that are precisely placed. The cameras were then rotated and locked into place once both of their field of views aligned with the centre of the calibration panel. The focus of the cameras was adjusted and then the apertures moved to their furthest closed position.

Figure 3.17 – ARAMIS Calibration Panel

The calibration process consisted of capturing various images of the calibration panel. The position of the panel in relation to the cameras was rotated and translated with an image captured each time. The software then automatically calculated the height, width, and depth of the field of view.

Before each set of tests a full calibration was performed on the system. At the start of each day of testing a quick calibration that consisted of only a few captured images was performed. It was discovered that the location of the tripod in relation to the load frame had a major effect on the accuracy of the calibration over time. If the tripod was placed too near to the supports of the load frame the vibrations produced by the servohydraulic system caused the camera system to lose its calibration in a very short time. To prevent this from occurring the position of the tripod had to be carefully monitored.

3.2.5.2 Setting the Acquisition Rate (Creating a Trigger List)

The ARAMIS system allows the users to manually record an image whenever they choose. However, manual image capture was not sufficient during the static and fatigue tests. Instead a triggerlist was programmed in the software that told the system when to capture images based on certain inputs. One triggerlist was created for the static tests and another for the fatigue tests.

The static test triggerlist was very simple. The system was set to record one image every second. Each time an image was captured the system also recorded the load that was currently applied to the specimen.

The fatigue triggerlist was more complicated. Similar to the static triggerlist the ARAMIS system was programmed to record an image at a set time interval, however the image was not to be captured until a specified load was applied. Due to limited computer memory the time interval had to be adjusted for each run depending on the estimated length of the test. The time interval ranged anywhere from 2 seconds to 300 seconds.

During a fatigue test each image would ideally be recorded only at the maximum applied load. In reality the trigger value was usually set about 2 kN lower than the actual maximum load. This was due to the possibility of small fluctuations in the load levels. If the actual applied load was lower than the load programmed in the triggerlist an image would not be recorded. However, by setting the trigger load slightly lower than the maximum it ensured that an image would always be recorded despite any small fluctuations in the applied load. Due to the fast load cycling the shutter speed of the cameras had to be increased in order to capture a clear image. The shutter speed was set between 24 ms and 29.5 ms depending on the paint pattern and lighting of each specimen.

3.2.5.3 Post Processing

After the data was collected the images were processed using the ARAMIS software. The software tracks every pixel's location in each of the images and from this data creates a three dimensional map of the deformation. From the deformation values the software also computes the strain in each direction, minor strain, major strain, and shear strain. The user can then specify points on the specimen to obtain the numerical value of the strain at that location. Cross-sections through the specimen can also be

selected in order to observe how deformation or strain changes across the face of the specimen. The software also displays graphs that show how the deformation and strain change with time or with applied load.

3.2.6 Data Acquisition System (DAQ)

The Vishay 7000 data acquisition system [87] shown in Figure 3.18 was used to record strains and applied loads during the testing. This system contains one 8-channel strain gauge board and one 8-channel high level voltage board. The strain gauge board has a measurement resolution of 0.5 microstrain and an electronically selectable, built-in bridge completion for 120, 350, or 1000 Ω strain gauges [88]. The high level voltage board was used to measure the applied load that was output as a ±10 V signal from the load frame. Both cards have a maximum scanning rate of 2048 scans per second.

Figure 3.18 – Vishay 7000 Data Acquisition System

3.3 Test Procedures

The test procedures for creating the impact damage, ultrasonic C-scan and thermography inspection, mechanical property evaluation, residual strength testing, and fatigue testing are detailed in the following sections.

3.3.1 Creating the Damage – Drop-Weight Impact Testing

Damage was applied to the specimens through the use of a drop-weight impact testing apparatus located at the Boeing Canada Technology - Winnipeg facility. The test method was based on ASTM D7136 – Standard Test Method for Measuring the Damage Resistance of a Fiber-Reinforced Polymer Matrix Composite to a Drop-Weight Impact Event [89].

The impact energy, P_E, of hail can be calculated from the mass of the hail, m_h, and the resultant velocity, V_r:

$$P_E = \frac{m_h V_r^2}{2} \ . \tag{3.1}$$

From Ref. [90] the mass of the hail is calculated using:

$$m_h = 3850r^3 \ , \tag{3.2}$$

where r is the radius of the hail. Also from [90], the resultant velocity is calculated using the terminal velocity, V_t, and the wind velocity, V_w:

$$V_R = \sqrt{V_t^2 + V_w^2} \ , \tag{3.3}$$

where the terminal velocity is equal to:

$$V_t = 140.4\sqrt{2r}\,. \tag{3.4}$$

It is possible during severe storms to observe hail with a radius of 19.3 mm travelling with a wind velocity of 37.5 m/s. Under these conditions the resulting hail impact energy is 30 J. This value assumes that the aircraft is completely stationary at the time of impact. If the aircraft is moving, then the velocity component of the aircraft will increase the energy of the hail impact.

Based on the above calculations the specimens were impacted at two different energy levels, 35 J and 50 J in order to be conservative. The required drop height, H, was calculated as:

$$H = \frac{P_E}{m_d g}\,, \tag{3.5}$$

where H is the drop height of the impactor, P_E is the potential energy of the impactor, m_d is the mass of the impactor (3.355 kg), and g is the acceleration of gravity ($9.81 m/s^2$). The required drop heights for the 35 J and 50 J energy levels were 1.06 m and 1.51 m respectively.

The dimensions of the specimens impacted during this testing are defined in Figure 3.5. Before the tests were conducted the length, width, and thickness of the specimens were measured near the anticipated damage location. The specimen was then secured in the support fixture and the impactor was raised to the desired drop height and released. To prevent additional impacts due to the rebound of the impactor, a rubber pad

affixed to a piece of wood was slid between the impactor and the specimen after the initial contact. The dent depth, height, width, and maximum damage diameter were measured after the impact event.

3.3.2 Non-Destructive Evaluation

3.3.2.1 Ultrasonic C-scan

The ultrasonic C-scans were performed at the National Research Council Canada – Institute for Aerospace Research in Ottawa, ON. Ultrasonic testing pulse echo inspection method uses beams of high-frequency sound waves for the detection of surface and subsurface flaws in solid laminates. The sound waves travel through the laminate facing the transducer and are reflected at interfaces perpendicular to the beam. The reflected beam is displayed and then analyzed to define the presence and location of discontinuities. This method was used for inspecting the solid laminate coupons for delamination and impact damage.

In ultrasonic testing an increase in frequency leads to increased detection sensitivity and higher resolution while reducing the depth of penetration. Therefore, low frequencies are used for thick composites or sandwich structures that attenuate the signal whereas for thin laminates, as was the case in this project, higher frequencies are employed to obtained optimal resolution.

3.3.2.2 Pulsed Thermography

The thermographic images were obtained at the National Research Council Canada – Institute for Aerospace Research in Ottawa, ON. In pulsed thermography, energy is applied to the specimen using a pulsed excitation. Typically, the energy sources are flash lamps whose flash duration varies from a few milliseconds for good thermal conductors to a few seconds for low-conductivity materials. The applied energy creates a thermal front that propagates from the specimen's surface throughout the specimen. During the cool-down process the surface temperature decreases uniformly for a sample without internal flaws. When the thermal front intersects an interface from a high to low conductivity layer, like in the case of delamination, disbond, or porosity, the cooling rate is locally disrupted. This results in an accumulation of heat above the flaw that is also manifested at the specimen's surface and can be detected by an infrared camera. Therefore, the defective areas can be distinguished from healthy areas.

3.3.3 Mechanical Property Evaluation

The processes for measuring and calculating the longitudinal, transverse, and shear modulus values of the individual plies are described below.

3.3.3.1 Longitudinal Compressive Modulus

The longitudinal compressive modulus of the individual plies was calculated by measuring the longitudinal modulus of 16 ply unidirectional specimens. The tests were performed according to ASTM D6641 – Standard Test Method for Determining the

Compressive Properties of Polymer Matrix Composites Using a Combined Loading Compression (CLC) Test Fixture [91].

The specimen dimensions are given in Figure 3.3 and resulted in a gauge length of 12.7 mm. Biaxial strain gauges were mounted on the front and back of the gauge section of each of the specimens. The C2A-06-125-LT-350 gauge from Vishay Micro-Measurements was chosen due to its 350 Ω resistance and 3.175 mm gauge length. Due to the lack of available biaxial gauges only some of the specimens had biaxial gauges on the front and the back faces. The remaining specimens had biaxial gauges on the front face and uniaxial gauges on the back face. The chosen uniaxial gauge was the C2A-06-062LW-350, also from Vishay Micro-Measurements, which has a 350 Ω resistance and a 1.588 mm gauge length.

Before the tests were performed the length of each specimen was measured, as well as the width and thickness of the gauge section. The specimen was then installed in the fixture shown in Figure 3.11 and the clamping screws were tightened to a torque of 5.08 N·m. The fixture was then placed between two fixed flat platens in the load frame and the strain gauges were attached to the DAQ system. In order to maintain contact between the compression platens and the fixture, a small compressive force of approximately -150 N was applied. The strain gauge readings were then set to zero.

ASTM D6641 [91] states that the percent bending, as measured by the difference in the strain values on the front and back face of the specimen, should not exceed 10%. To ensure the specimen was properly aligned within the fixture the load was increased to -1 kN and increased in -2 kN intervals until a load of -9 kN was applied. The strain on

the front and back faces were measured during this test and used to calculate the percent bending using Eqn (3.6):

$$B_y = \frac{\varepsilon_f - \varepsilon_b}{\varepsilon_f + \varepsilon_b} \times 100 , \qquad (3.6)$$

where B_y is the percent bending, ε_f is the strain recorded by the front gauge, and ε_b is the strain recorded by the back gauge. If the percent bending exceeded 10%, the fixture was removed from the load frame and the specimen position was adjusted. This process was repeated until the specimen was aligned properly in the fixture and the percent bending was less than 10%.

After the alignment check was successfully performed the load frame was set to work in position control and the specimen was loaded in compression at a rate of -0.3 mm/min. During the test the load and strain values were recorded by the DAQ system 10 times every second. The test was stopped when the measured strain was approximately -3300 με. After the testing was complete the percent bending was calculated to ensure that this value did not exceed 10%.

3.3.3.2 Transverse Modulus

The testing which was performed to calculate the transverse modulus of the individual plies was performed using the same method as was used to calculate the longitudinal modulus (Section 3.3.3.1). The only difference was that specimens with a $[90]_{16}$ laminate schedule were tested. For this testing, C2A-06-125LT-350 strain gauges were applied to both the front and back faces of all of the specimens.

3.3.3.3 Shear Modulus

The shear modulus of the individual plies was calculated from data produced by testing $[0/90]_{4S}$ panels. The test method was based on ASTM D7078 – Standard Test Method for Shear Properties of Composite Materials by V-Notched Rail Shear Method [92]. This test was performed at the Industrial Technology Centre, located in Winnipeg, Manitoba, using their load frame and data acquisition systems. The load frame used was a MTS Landmark 100kN universal test machine [93] with a 22.2 kN load cell. The data acquisition system was a National Instruments SCXI system [94].

The test specimens were rectangular and had symmetric centrally located V-notches as shown in Figure 3.4. Strain gauges were bonded to the front and back of the gauge section of each specimen and oriented ±45° to the loading direction. The CEA-06-187UV-350/P2 stain gauge produced by Vishay Micro-Measurements was chosen for this purpose. These gauges have a 350 Ω resistance and a gauge length of 4.763 mm. Each ±45 gauge was wired in a half bridge configuration that recorded strain as the sum of the absolute value of the response of each gauge element. This resulted in the engineering shear strain being measured directly.

Before the testing was performed the width across the notch and the thickness at the notch were measured for each specimen. The two fixture halves shown in Figures 3.12 and 3.13 were gripped in the load frame and then the specimen was installed in the fixture. This was done by inserting the specimen into one fixture half with the spacer block in place and ensuring that the specimen was aligned with the centring marks on the spacer. Each bolt on the fixture half was then tightened. The specimen was then placed

in the second fixture half while the spacer blocks were used to ensure the proper spacing between the two fixture halves. The clamping bolts were then tightened on the second half of the fixture. The spacer blocks were removed and the strain gauges were attached to the data acquisition system and set to zero. The test was run in position control at a rate of +2 mm/min. The test was run until failure occurred in the specimen.

3.3.4 Residual Strength Tests

3.3.4.1 Undamaged Specimens

The strength and modulus values of the undamaged $[+45/90/-45/0]_{3S}$ laminate were measured using a test method based on ASTM D6641 – Standard Test Method for Determining the Compressive Properties of Polymer Matrix Composites Using a Combined Loading Compression (CLC) Test Fixture [91]. The test method was very similar to that described in Section 3.3.3.1 with a few key differences.

This test used the same specimen dimensions and fixture that was specified in Section 3.3.3.1. The strain gauges applied to the front and back faces of the specimens were C2A-06-062LW-350 uniaxial gauges made by Vishay Micro-Measurements. This gauge type was chosen due to its 350 Ω resistance and its 1.588 mm gauge length that was small enough to fit within the 12.7 mm gauge section of these specimens.

The length, width, and thickness of each specimen were measured and then the test was setup in the same manner described in Section 3.3.3.1. After the alignment check was completed the load frame was set in position control and the specimen was

loaded in compression at a rate of -1.3 mm/min with the strain and load values recorded by the DAQ system 10 times every second. The load was applied until failure occurred in the specimen.

The specimen was examined after removal from the load frame and the fixture to determine the failure mode. Any specimens that failed due to end crushing or failed at the grips were discarded and another test was run in its place. The strain values were also examined for percent bending values exceeding 10% as calculated by Eqn (3.6).

3.3.4.2 Damaged Specimens

The test procedure for measuring the residual strength of the impacted panels was based on ASTM D7137 – Standard Test Method for Compressive Residual Strength Properties of Damaged Polymer Matrix Composite Panels [95].

The test specimens used during this test were those that were damaged using the drop-weight impactor as described in Section 3.3.1. After the impact testing was completed, a speckled paint pattern, shown in Figure 3.16, was applied to the specimens for use with the DIC equipment. Once the paint had dried, strain gauges were applied 25.4 mm from the top and side edges of the front and back faces of the specimen. For this application the C2A-06-250LW-350 uniaxial gauge from Vishay Micro-Measurements was chosen. This gauge has a 350 Ω resistance and a 6.35 mm gauge length.

For each test the specimen was first clamped between the slide plates of the top plate of the fixture shown in Figure 3.14. The specimen was then placed in the bottom

half of the fixture and aligned perpendicular to the base plate using the side plates attached to the angles and the slide plates attached to the base of the fixture. All of the screws were hand tightened and then torqued to 6.78 N·m.

The fixture was then placed in between the flat platens in the load frame and centred. The strain gauges were hooked up to the DAQ system and a small compressive load of - 150 N was applied. At this point the strain gauges were zeroed. Force was then applied in -10 kN increments and the strain recorded until a force of -60 kN was applied. The strain values were examined to determine if the percent bending as defined in Eqn (3.6) exceeded 10% at the maximum applied load. If the percent bending exceeded 10% the fixture was removed from the load frame and the side and slide plates were adjusted in order to better align the specimen. The fixture was then placed back in the load frame and the alignment test was performed again. This procedure was repeated until the percent bending was less than 10%.

After the alignment procedure was complete a -150 N compressive load was applied and the data acquisition system zeroed. Before the residual strength test was performed the DIC system was setup. The position of the tripod was adjusted until the damage was centred in the field of view of the cameras. A pre-test was performed to ensure that the DIC system was working properly and that the size of the paint pattern was appropriate. This consisted of taking a picture and immediately taking another picture without applying any additional load. The processing algorithms were run and the results reviewed to ensure that the pictures were producing usable data. After successful completion of the pre-test the DIC system was set to record one picture every second for the duration of the test.

After all of the pre-tests were successfully completed the load frame was set to work in position control and apply a compressive load at a rate of -0.3 mm/min while the strain and load data were recorded by the DAQ system 10 times per second. The displacement was continuously increased until specimen failure occurred.

The specimen was examined after removal from the load frame and the fixture to determine the failure mode. Any specimens that failed at the grips were discarded and another test was run in its place. The strain values were also examined for percent bending values exceeding 10%.

3.3.5 Fatigue Testing

3.3.5.1 Undamaged Specimens

There is currently no published standard for performing compression-compression fatigue testing of composite materials. The procedure for fatigue testing the undamaged specimens was loosely based on ASTM D6641 – Standard Test Method for Determining the Compressive Properties of Polymer Matrix Composites Using a Combined Loading Compression (CLC) Test Fixture [91]. Many of the steps were the same as used to perform the static testing described in Sections 3.3.3.1 and 3.3.4.1. The same specimen dimensions, fixture, and strain gauges (C2A-06-062LW-350) were used. The specimen was installed in the fixture in the same manner and the alignment check was performed using the same steps. The only difference in test setup was the torque value used to secure the clamping screws of the fixture. A torque of 4.86 N·m was used for the

majority of tests. To help prevent premature failure at the grips during longer duration tests the torque was lowered to 4.63 N·m for some tests.

For these fatigue tests a type K thermocouple was attached to the gauge section of each specimen using 5-minute epoxy. The thermocouple was then attached to a temperature data logger to record hysteretic heating.

After the alignment check described in Section 3.3.3.1 was completed a load of -150 N was applied to the specimen and the strain gauges were zeroed. The DAQ system was set to record the load and strain values 100 times every second. A faster recording time then for the static tests was required in order to capture the highs and the lows of the cyclic loading. Next, the temperature data logger was turned on to record the temperature data. A fan was turned on and aimed at the fixture in order to dissipate some of the heat caused by hysteresis.

Load ratio is defined as the ratio of the minimum applied load over the maximum applied load during a fatigue test. The chosen load ratio for this study was R = 10. In order to observe how the fatigue life changed with varying maximum compressive stress, the minimum compressive stress also had to change for each test in order to maintain the load ratio of 10.

Once all of the setup had been completed the minimum compressive load was then applied to the specimen. This load was usually in the range of -2.7 kN to -4 kN. MIL-HDBK-17-1F [96] recommends that a testing frequency of 5 to 10 Hz is usually appropriate for fatigue testing of composite materials. Therefore, the load frame was set to run in load control and apply a sine wave at a frequency of 5 Hz. Next, the amplitude

of the sine wave (calculated based on the desired maximum compressive stress) for each test was entered.

The minimum applied loads during these tests were at the bottom 1.5% of the capacity of the loadcell. It was discovered that the loadcell was not capable of hitting these loads consistently without adjusting the proportional gain and lag values as described in Section 3.2.3. The proportional gain was increased to between 23 and 24, and the lag value was increased to 5 ms. After these adjustments the loadcell was capable of reaching the minimum specified loads. After all of the values were set, the test was started and ran until either specimen failure occurred or the test exceeded 10^6 cycles.

3.3.5.2 Damaged Specimens

As stated in Section 3.3.5.1 there is currently no published standard for performing compression-compression fatigue testing of composite materials. The test method used for fatigue testing of the damaged specimens was loosely based on ASTM D7137 – Standard Test Method for Compressive Residual Strength Properties of Damaged Polymer Matrix Composite Panels [95]. A lot of the steps to perform the fatigue tests were the same as those described in Section 3.3.4.2. The fatigue tests used the same fixture, specimen dimensions, paint pattern, strain gauges, alignment procedures, and DIC pre-test procedures.

In addition to the specimen preparations described previously, a type K thermocouple was attached to the specimen using 5-minute epoxy. The thermocouple

was hooked up to a temperature data logger to measure hysteretic heating during the fatigue test.

After the alignment check and DIC pre-test were completed one additional measurement was made before the fatigue test was run on the 35 J specimens. A compressive load of -60 kN was applied in -10 kN intervals. At each interval a picture was taken using the DIC system. The specimen was then unloaded to the -150 N pre-load.

After all of the preliminary tests were completed the strain gauges were zeroed again. The DAQ system was set to record the load and strain values 100 times every second. Next, the temperature data logger was turned on. Finally, the DIC fatigue triggerlist described in Section 3.2.5.2 was set to run.

Before starting the fatigue cycling the minimum compressive load was applied to the specimen. This was usually in the range of -11 kN to -15 kN. The load frame was set to run in load control and apply a sine wave at a frequency of 5 Hz. Next, the amplitude of the sine wave for each test was entered. The proportional gain was set to between 14 and 15, and the lag value was set at 0.8 ms for all of the damaged fatigue tests. Once all of the loadframe input values were set the test was started and ran until either specimen failure occurred or the test exceeded 10^6 cycles.

4 RESULTS AND DISCUSSION

In this chapter the results of the testing described in Chapter 3 are presented and discussed. The first section presents the results of the mechanical property evaluation of the individual lamina. The second section discusses the results of the non-destructive evaluation of the damage caused by the drop-weight testing. Next, the static testing of both the undamaged and damaged laminates is presented. Also, the calculated stress concentration factors are examined. In the fourth section the results of the fatigue testing are given. This includes a presentation of the displacement and strain results measured by the DIC system, the calculation of stress concentration factors, and S-N curves for the undamaged and damaged specimens. In the last two sections an attempt is made to apply the models of Yuanjian and Isaac [75] and Kang and Kim [76] to correlate the fatigue data.

4.1 Mechanical Property Evaluation

In this section the results from the mechanical property testing described in Section 3.3.3 are discussed. Specifically, the longitudinal compressive, transverse, and shear modulus values of the individual lamina are calculated. As stated in Chapter 3, these tests and calculations were completed in accordance with ASTM D6641 [91] for the longitudinal and transverse tests, and ASTM D7078 [92] for the shear tests.

4.1.1 Longitudinal Compressive Modulus

Five specimens of a $[0]_{16}$ laminate were tested to determine the longitudinal compressive modulus of a single ply of the carbon/epoxy material. ASTM D6641 [91] does not recommend testing unidirectional laminates until failure because high fixture clamping forces may be required to prevent end crushing. The high clamping forces can induce a stress concentration at the end of the gauge section and produce erroneously low strength values. Therefore, the test was stopped while the stress-strain relationship was still linear. The linear portion of a typical stress versus strain curve for one of the five tests is shown in Figure 4.1. The stress, S, is calculated from:

$$S = \frac{P}{wt}, \tag{4.1}$$

where S is the stress, P is the applied load, w is the specimen gauge width, and t is the specimen gauge thickness. The elastic modulus of the laminate is equal to the slope of the stress vs. strain plot.

Figure 4.1 – Stress vs. Longitudinal Strain for a $[0]_{16}$ Laminate

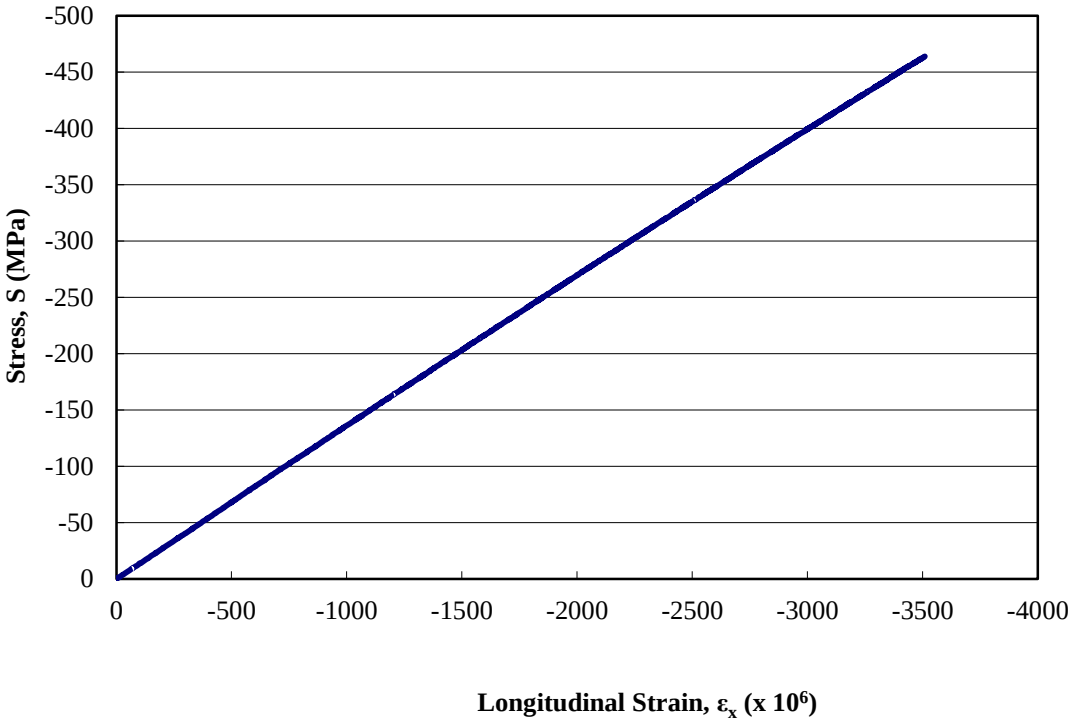

From classical laminate theory it is known that the longitudinal modulus of a single ply is equal to the longitudinal modulus of a unidirectional laminate. In order to solve for the compressive modulus and Poisson's ratio using the method outlined in ASTM D6641 [91], the applied loads at 1000 με and 3000 με were measured for five specimens. The reported strain values were the average of the strain values measured from the front and the back gauges. The longitudinal modulus, E_X, is calculated from these values as:

$$E_X = \frac{P_{3000} - P_{1000}}{(\varepsilon_{x,3000} - \varepsilon_{x,1000})wt}, \tag{4.2}$$

where $\varepsilon_{x,3000}$ is the actual measured longitudinal strain closest to 3000 με, $\varepsilon_{x,1000}$ is the actual measured longitudinal strain closest to 1000 με, and P_{3000} and P_{1000} are the applied loads at $\varepsilon_{x,3000}$ and $\varepsilon_{x,1000}$ respectively. Poisson's ratio, ν_{xy} , can be calculated as:

$$\nu_{xy} = - \frac{\varepsilon_{y,3000} - \varepsilon_{y,1000}}{\varepsilon_{x,3000} - \varepsilon_{x,1000}} , \tag{4.3}$$

where $\varepsilon_{y,3000}$ is the transverse strain that corresponds to $\varepsilon_{x,3000}$, and $\varepsilon_{y,1000}$ is the transverse strain that corresponds to $\varepsilon_{x,1000}$. The recorded load closest to 3000 and 1000 με, and the corresponding longitudinal and transverse strains are shown in Table 4.1.

Table 4.1 – Load and Strain from Longitudinal Compressive Modulus Testing

Specimen	P_{3000} (N)	P_{1000} (N)	$\varepsilon_{x,3000}$ (με)	$\varepsilon_{y,3000}$ (με)	$\varepsilon_{x,1000}$ (με)	$\varepsilon_{y,1000}$ (με)	E_X (GPa)	ν_{xy}
U1	-15465	-5233	-3001.0	68.5	-998.5	425.0	127.0	0.36
U2	-15820	-5408	-3004.0	59.0	-1003.5	432.5	131.7	0.37
U3	-15715	-5485	-3000.5	67.5	-999.5	330.0	131.1	0.36
U4	-15553	-5405	-2994.0	70.5	-1000.0	443.0	129.7	0.37
U5	-15530	-5235	-3003.5	66.5	-997.5	535.0	131.6	0.41
						Mean	130.2	0.37
						Stnd Dev	1.9	0.02
						Coeff. of Var. (%)	1.5	5.6

The average longitudinal compressive modulus of the five specimens was 130.2 GPa and the Poisson's ratio was equal to 0.37. These values, along with their corresponding standard deviation and coefficient of variation, are summarized with the other mechanical properties at the end of Section 4.1 in Table 4.4.

4.1.2 Transverse Compressive Modulus

Five specimens of a $[90]_{16}$ laminate were tested to determine the transverse compressive modulus of a single ply of the carbon/epoxy material. The linear portion of a typical stress versus strain curve for one of the five tests is shown in Figure 4.2. The applied stress to obtain a strain of 3000 με is much lower for the $[90]_{16}$ laminate shown in this figure compared to the applied stress for the $[0]_{16}$ laminate shown in Figure 4.1. This is expected since the reinforcing fibres are no longer in the direction of the applied load.

Figure 4.2 – Stress vs. Longitudinal Strain for a $[90]_{16}$ Laminate

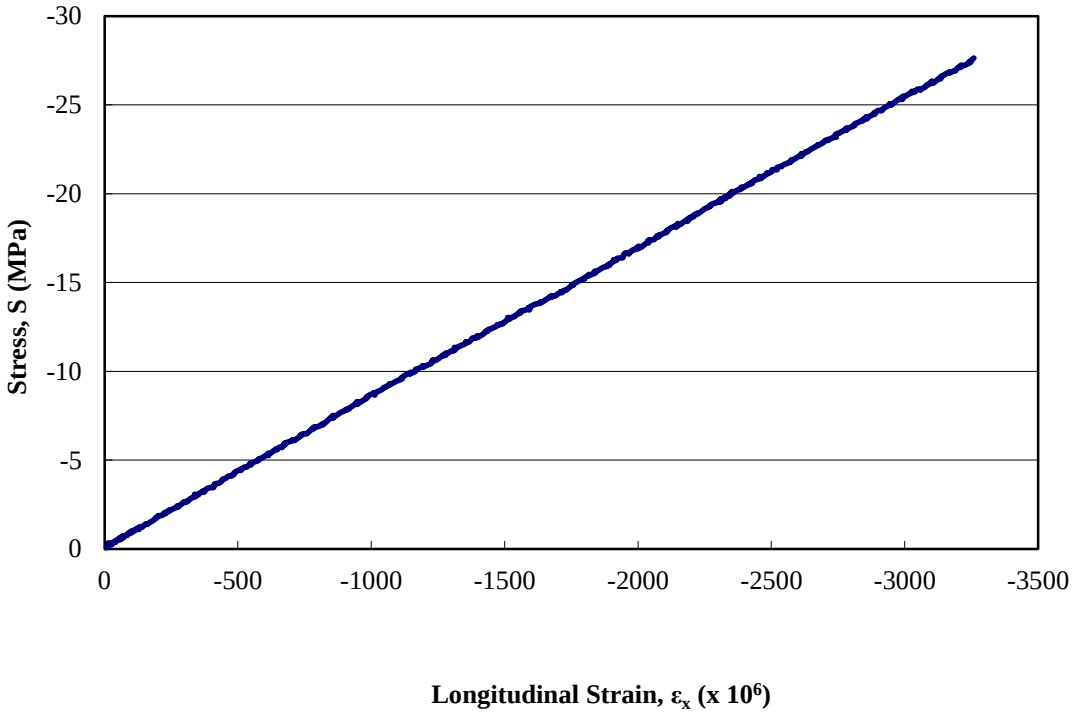

From classical laminate theory it is known that the transverse modulus of a single lamina will be equal to the longitudinal modulus of a $[90]_n$ laminate. The modulus was measured and calculated as described in Section 4.1.1 and Eqn (4.2), except that E_X was replaced by E_Y. The recorded loads closest to 3000 and 1000 με, and the corresponding longitudinal and transverse strains in the $[90]_{16}$ laminate are shown in Table 4.2. The

average transverse modulus for the five specimens was 8.4 GPa. This value, and the standard deviation and coefficient of variation for the 5 specimens, are summarized with the other mechanical properties in Table 4.4 at the end of Section 4.1.

Table 4.2 - Load and Strain Values from Transverse Modulus Testing

Specimen	P_{3000} (N)	P_{1000} (N)	$\varepsilon_{x,3000}$ ($\mu\varepsilon$)	$\varepsilon_{y,3000}$ ($\mu\varepsilon$)	$\varepsilon_{x,1000}$ ($\mu\varepsilon$)	$\varepsilon_{y,1000}$ ($\mu\varepsilon$)	E_Y (GPa)
T1	-1005	-338	-3001.0	68.5	-999.5	23.0	8.4
T2	-1005	-338	-3004.0	59.0	-1001.0	19.5	8.5
T3	-980	-333	-3000.5	67.5	-999.0	22.5	8.3
T4	-995	-338	-2994.0	70.5	-992.5	24.0	8.4
T5	-948	-323	-3003.5	66.5	-1002.0	22.0	8.2
						Mean	8.4
						Stnd Dev	0.1
						Coeff. of Var. (%)	1.3

4.1.3 Shear Modulus

Five $[0/90]_{4S}$ specimens were tested to determine the in-plane shear modulus of a single ply of the carbon/epoxy material. A typical stress-strain curve for one of the five tests is shown in Figure 4.3 below. The stress-strain relationship is linear until approximately 30 MPa of stress is applied. The shear strain continues to increase with increasing shear stress after this point, but in an increasingly non-linear fashion.

Figure 4.3 – Shear Stress vs. Engineering Shear Strain for a $[0/90]_{4S}$ Laminate

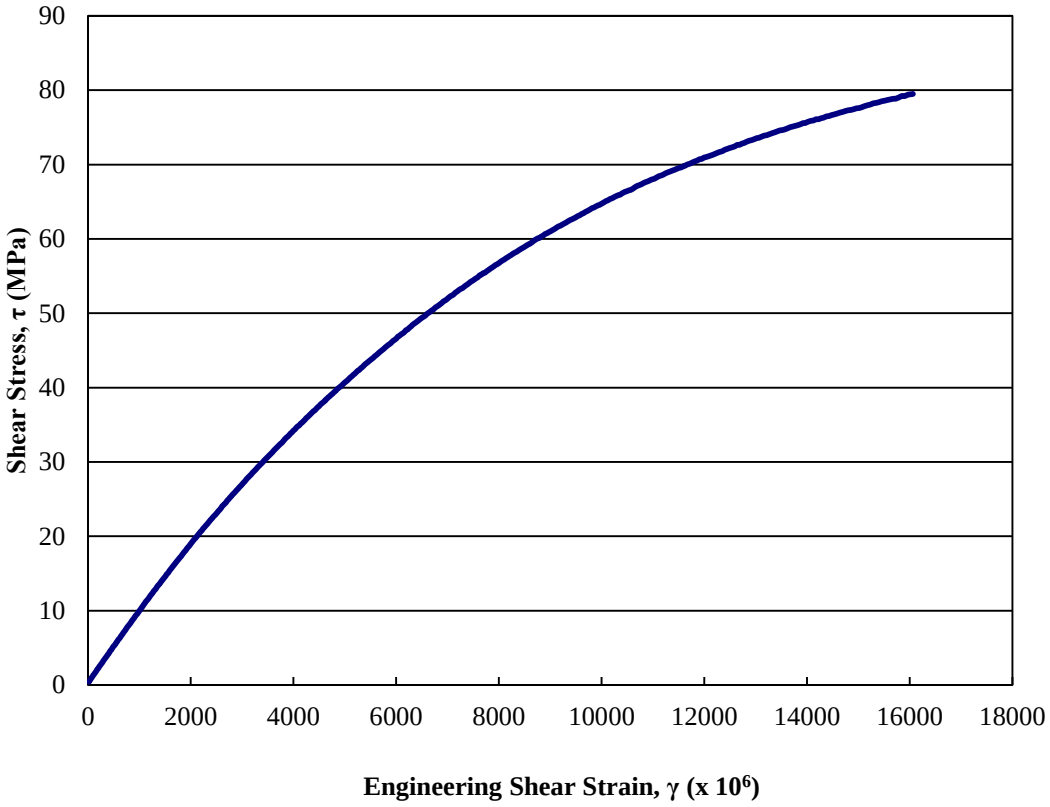

From classical laminate theory it is known that the shear modulus of a single ply is equal to the shear modulus of a $[0/90]_{nS}$ laminate. In order to solve for the shear modulus the applied load at 1500 με and 5500 με was measured for five specimens as recommended in ASTM D7078 [92]. The reported strain values were the average of the strain values measured from the front and the back gauges. The in-plane shear modulus, G_{xy} , can be calculated from the data as:

$$G_{xy} = \frac{P_{5500} - P_{1500}}{(\gamma_{5500} - \gamma_{1500})d_l t}, \tag{4.4}$$

where d_l is the width across the notch, t is the thickness of the specimen, γ_{5500} is the actual measured engineering shear strain closest to 5500 με, γ_{1500} is the actual measured engineering shear strain closest to 1500 με, and P_{5500} and P_{1500} are the applied loads at

γ_{5500} and γ_{1500} respectively. The recorded loads closest to 5500 and 1500 με, and the corresponding shear strains are shown in Table 4.3.

Table 4.3 - Load and Strain Values from Shear Modulus Testing

Specimen	P_{5500} (N)	P_{1500} (N)	γ_{5500} (με)	γ_{1500} (με)	G_{xy} (GPa)
S1	4133	1388	5491.9	1511.0	7.3
S2	4204	1374	5509.4	1497.0	7.5
S3	4148	1342	5513.0	1487.9	7.3
S4	4171	1365	5487.8	1501.4	7.5
S5	4180	1386	5495.5	1502.5	7.4
				Mean	7.4
				Stnd Dev	0.1
				Coeff. of Var. (%)	1.3

The average in-plane shear modulus was 7.4 GPa. This value, and the standard deviation and coefficient of variation for the 5 specimens, are summarized in Table 4.4, along with the longitudinal and transverse modulus results.

Table 4.4 – Lamina Mechanical Properties

Property	Mean Value	Standard Deviation	Coefficient of Variation (%)
E_X (GPa)	130.2	1.9	1.5
E_Y (GPa)	8.4	0.1	1.3
G_{xy} (GPa)	7.4	0.1	1.3
ν_{xy}	0.37	0.02	5.6

These results are similar to unidirectional carbon/epoxy prepreg mechanical properties given in MIL-HDBK-17-2F [97]. Most of the materials listed in Ref. [97] have a longitudinal modulus value between 115 GPa and 140 GPa which compare well with the test value of 130.2 GPa shown above. The transverse modulus of the

carbon/epoxy laminates in Ref. [97] were between 9.5 GPa and 10.0 GPa. The prepreg for this project had a slightly lower transverse modulus of 8.4 GPa. The shear modulus values for the materials in Ref. [97] were between 3.7 GPa and 6.3 GPa. The material for this project had a larger shear modulus value of 7.4 GPa. These values indicate that the test material for this project compares favourably with other carbon/epoxy prepregs and may have superior performance under shear loading conditions.

4.2 Drop-Weight Impact Testing

In preparation for the static and fatigue compression tests, 34 specimens were impacted at a 35 J impact energy level and another 25 specimens were impacted at a 50 J impact energy level. After impact the specimens were inspected visually, and then using ultrasonic C-scan and thermography.

4.2.1 Visual Inspection

Small cracks originating at the impact site were visible on the top ply for most of the specimens at both impact energy levels. Usually the cracks appeared in the longitudinal direction of the specimen although in some cases they appeared in the diagonal direction, or even occasionally in the transverse direction. For some specimens a crack would appear on both sides of the impact site, but in other specimens the crack would only appear on one side. Generally, the appearance of cracks was more frequent for the 50 J specimens and the cracks were usually longer when compared to the cracks in the 35 J specimens. Figure 4.4 shows a typical crack pattern observed in a specimen.

Figure 4.4 – Typical Visible Impact Damage

The depth, length, width, and maximum diameter of the indentation of the damage, not including any cracks, were measured for each impacted specimen according to Figure 4.5. The depth was measured using a dial gauge, while the length, width, and maximum diameter of the indentation were measured using calipers. The size of the visible damage was found to increase for each of the parameters as the impact energy was increased. The average value for each of the damage parameters is summarized in Table 4.5.

Figure 4.5 – Length, Width, and Maximum Diameter of Damage

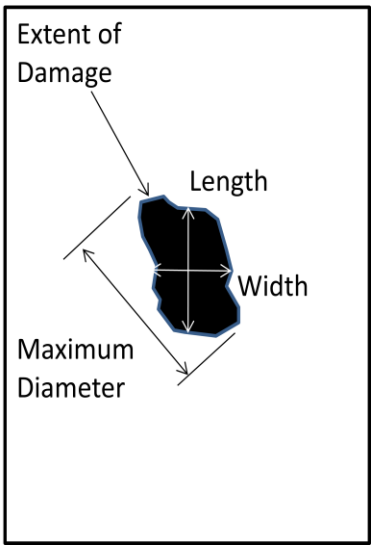

Table 4.5 – Summary of Visual Inspection Results

	Impact Energy P_E (J)	35	50
Damage Depth (mm)	Mean	0.247	0.299
	Standard Deviation	0.017	0.020
	Coefficient of Variation (%)	6.7	6.7
Damage Length (mm)	Mean	7.263	7.779
	Standard Deviation	0.202	0.284
	Coefficient of Variation (%)	2.8	3.7
Damage Width (mm)	Mean	7.368	7.878
	Standard Deviation	0.160	0.294
	Coefficient of Variation (%)	2.2	3.7
Maximum Damage Diameter (mm)	Mean	7.540	8.067
	Standard Deviation	0.130	0.223
	Coefficient of Variation (%)	1.7	2.8

It should be noted that at these impact energy levels the damage was often difficult to observe, and only became noticeable when the specimen was adjusted in order to reflect light off of the indentation. This was especially true for those specimens that had very small cracks. Damage of this size would be very difficult to detect on a large aircraft structure using only visual observation techniques.

4.2.2 Ultrasonic C-scan

Typical damage patterns detected by ultrasonic C-scan for the 35 J and 50 J specimens are shown in Figure 4.6. The maximum length, width, diameter, and area of internal damage were measured for each impacted specimen. The C-scan was able to measure the two dimensional shape of the damage, but was unable to measure how the damage shape changed through the thickness of the laminate. The results are summarized in Table 4.6.

Figure 4.6 – Ultrasonic C-scan Images of the Impact Damage

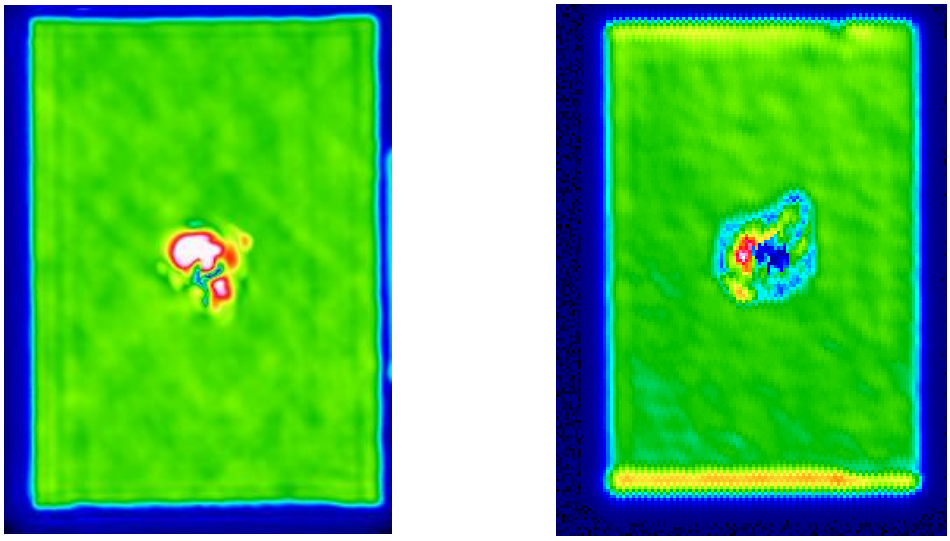

35 J **50J**

Table 4.6 – Summary of Ultrasonic C-Scan Results

	Impact Energy P_E (J)	35	50
Max Length (mm)	Mean	33.4	42.9
	Standard Deviation	3.4	4.7
	Coefficient of Variation (%)	10.3	11.0
Max Width (mm)	Mean	32.3	38.4
	Standard Deviation	2.3	1.7
	Coefficient of Variation (%)	7.0	4.4
Max Diameter (mm)	Mean	35.9	44.9
	Standard Deviation	2.9	4.4
	Coefficient of Variation (%)	8.1	9.8
Area (mm^2)	Mean	782.2	1108.6
	Standard Deviation	84.2	73.5
	Coefficient of Variation (%)	10.8	6.6

All four parameters increased in value when the impact energy was increased from 35 J to 50 J. For the 35 J specimens the average maximum length and width were very close to each other. This resulted in a circular damage area. The average maximum length and width were farther a part for the 50 J specimens, and thus an elliptical damage pattern was observed. The damage length and width measured by the C-scan was approximately 4.5 to 5.5 times larger than the values measured during the visual inspection. This indicates that the internal damage was much larger and more severe than the visually observable surface damage.

The damage area, as measured by C-scan, is plotted against impact energy in Figure 4.7. The threshold impact energy level is the impact level below which no damage occurs in the laminate because the energy is absorbed as elastic strain energy in the material [26]. When the absorbed energy exceeds this level then damage is formed. The threshold energy level for this material and lay-up is unknown at this time. In order to have a third point to plot, the threshold energy level was taken to be 0 J. That is, the damage area was plotted at zero when the impact energy was equal to zero. From this preliminary data it appears that the damage area increased linearly with impact energy. Assuming the threshold energy level is equal to zero is a conservative assumption because it will over predict the damage area for a given impact energy.

The linear relationship between damage area and impact energy agrees well with the work of Xiong et al. [23] who tested the same material and a very similar 24 ply quasi-isotropic lay-up. They found that the core damage, which refers to the area of delamination through the thickness of the specimen, increased with increasing impact energy level but at a decreasing rate. However, the total damage, which included splitting and blowout of the back surface, increased linearly with increasing impact energy level for the entire range of energy levels tested. This also agrees with the results from Ref. [3] for a woven carbon/epoxy laminate.

Figure 4.7 – Damage Area Measured by C-scan Compared to Impact Energy

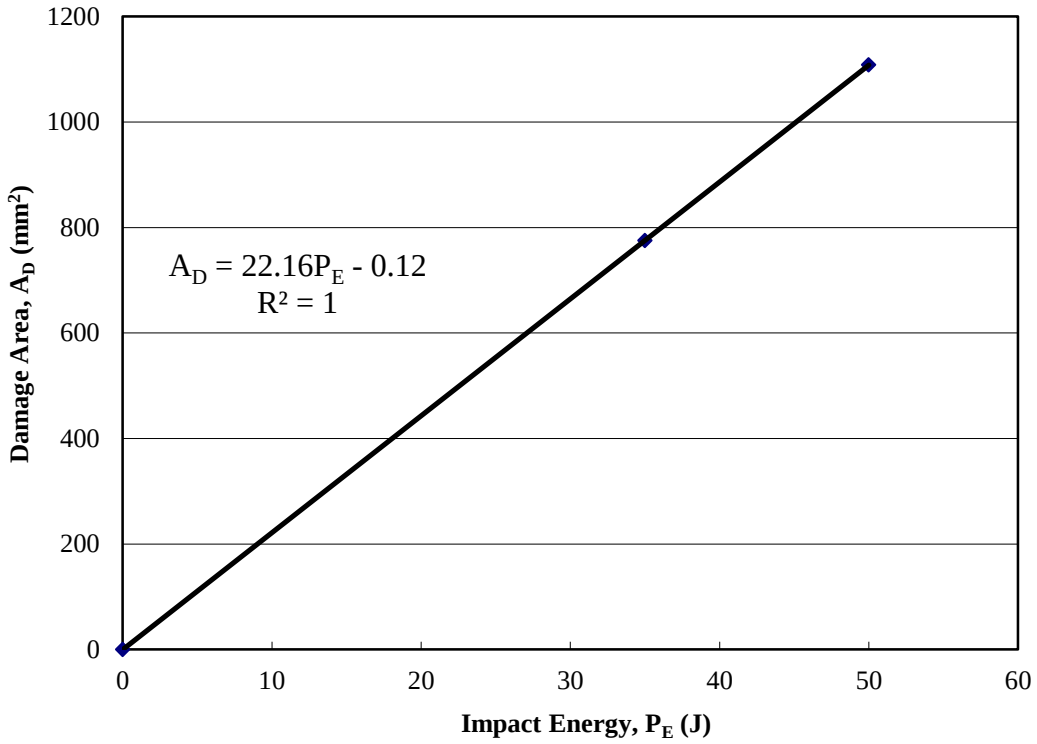

4.2.3 Thermography

Typical damage patterns as recorded by thermography are shown in Figure 4.8. Similar to the ultrasonic C-scan inspection, the maximum length, height, diameter, and damage area were measured for each of the specimens using thermography. These measurements included the length of any cracks in the specimen. Both the front and back faces were examined, providing some indication for how the damage varies through the thickness of the specimen. The results are summarized in Table 4.7.

Figure 4.8 – Thermography Images of the Impact Damage

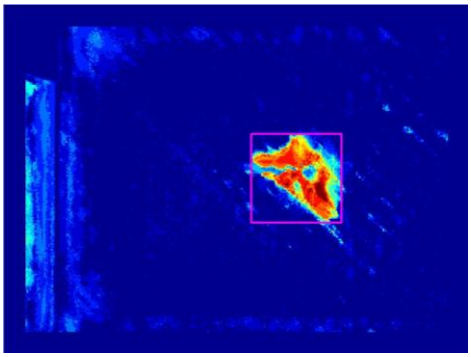

Front Image

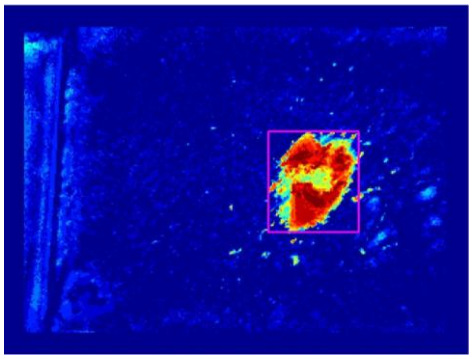

Back Image

35 J

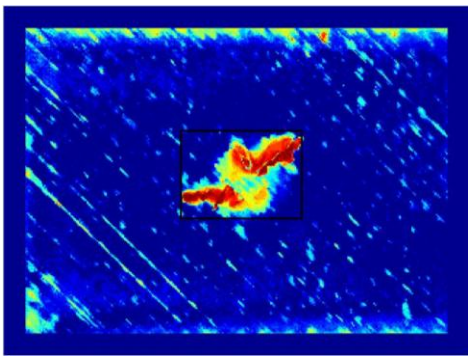

Front Image

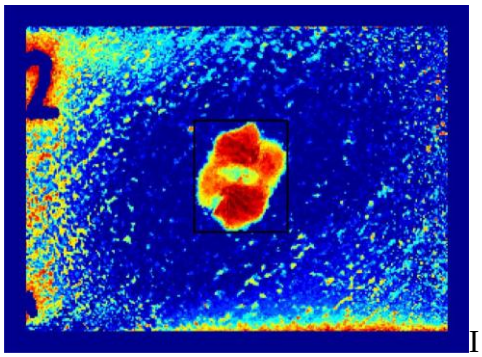

Back Image

50J

All four of the parameters increased in size when the impact energy level was increased from 35 J to 50 J. This matches with the ultrasonic C-scan results. The maximum length and width of the damage were often quite close for the 35 J specimens for both the front and back face scans. This results in a circular shaped damage area. For the 50 J specimens the shape of the damage area was more elliptical. However, the orientation of the ellipse varied from the front to the back face. On the front face the long axis of the damage was oriented along the length of the specimen. However, on the back face this trend was reversed, and the long axis of the damage was oriented along the

width of the specimen. This may be an indication of how damage area changed depending on the orientation of the fibres in a given ply. Also, the shape of the damage on the front face was more irregular, often following the shape of the surface cracks. The damage shown on the back face had a more regular elliptical shape.

Table 4.7 - Summary of Thermography Results

	Impact Energy P_E (J)	35 (Front)	35 (Back)	50 (Front)	50 (Back)
Max Length (mm)	Mean	23.0	25.9	36.0	26.3
	Standard Deviation	7.0	1.9	6.3	1.6
	Coefficient of Variation (%)	30.7	7.4	17.6	6.3
Max Width (mm)	Mean	21.7	29.8	27.6	33.4
	Standard Deviation	3.7	1.8	4.8	1.7
	Coefficient of Variation (%)	17.2	6.2	17.2	5.0
Max Diameter (mm)	Mean	26.7	30.9	37.0	34.0
	Standard Deviation	5.3	1.8	6.3	1.6
	Coefficient of Variation (%)	19.8	5.8	17.0	4.8
Area (mm^2)	Mean	262.4	485.8	494.7	556.0
	Standard Deviation	70.8	42.5	90.1	40.6
	Coefficient of Variation (%)	27.0	8.7	18.2	7.3

The coefficient of variation for all of the parameters was much higher for the front face scans compared to the scans of the back face. This is due to the inclusion of the crack length in the measurements. Cracks were visible on the front surface of most of the specimens. There was significant variation in the length and orientation of these cracks and this contributed largely to the variation in the front face results. The cracks were not usually visible in the back face scans. This resulted in much more consistent measurements of the damage.

The maximum damage area increased in size from the front to the back face. This indicates that the size of the damage increases through the thickness of the specimen. This increase was more substantial for the 35 J specimens than for the 50 J specimens. This is again most likely related to the cracks visible on the front faces. The cracks added to the total measured damage area on the front facess. Since the cracks were more common and larger for the 50 J specimens, the damage area on the front faces of the 50 J specimens had a larger increase than the damage area on the front faces of the 35 J specimens.

The maximum height, width, and length values measured by thermography are approximately 10 to 25% smaller than the values measured by ultrasonic C-scan. The maximum damage area is 40 to 50% smaller when measured by thermography. This may be related to the fact that thermography is limited in the thickness in which it can detect damage, while ultrasonic C-scan can detect the damage through the entire thickness in one scan. This indicates that results can vary when using different non-destructive evaluation techniques to characterize impact damage and care must be taken when comparing results.

As expected, the maximum damage area increased when the impact energy level was increased from 35 J to 50 J. The change in damage size between the two impact energy levels could lead to differences in the static and fatigue test results for the two sets of specimens. Both the ultrasonic C-scan and thermography results also showed that there is a large amount of variation in the damage size and orientation at a given impact energy level. This may lead to scatter within the static and fatigue test results within a given energy level.

4.3 Laminate Static Testing

The results from the static compressive tests described in Section 3.3.4 are discussed in this section. The compressive modulus and strength of the undamaged specimens are calculated first. Next, the modulus and residual strength of the damaged specimens are presented. Finally, the stress concentration factor calculated at the damage region and the increasing depth of the damage during the static testing are discussed.

4.3.1 Undamaged Specimens

The compressive modulus and ultimate compressive strength were measured for five undamaged specimens. A typical stress versus strain curve for one of the five tests is shown in Figure 4.9. The curve for the undamaged specimen remains linear for about the first half of the test and then becomes slightly non-linear at an applied stress of approximately -300 MPa as indicated in the figure. This is typical for a brittle material that will fail with little or no warning. Figure 4.10 shows the specimen after failure.

Figure 4.9 – σ-ε Curve for Static Compressive Test on an Undamaged Specimen

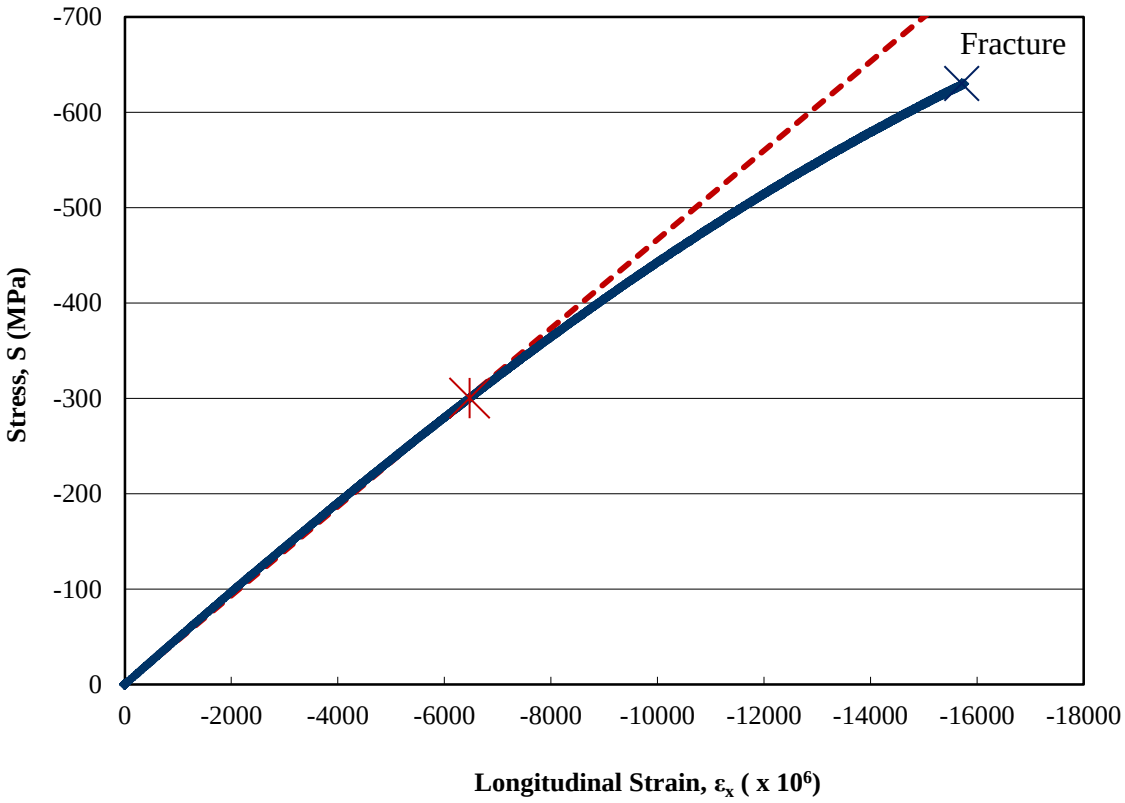

Figure 4.10 – Smooth Specimen After Static Compression Failure

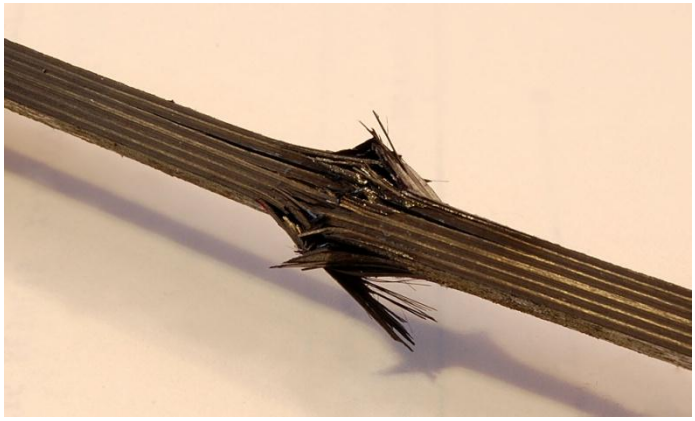

In order to solve for the compressive modulus the applied load at 1000 με and 3000 με was measured as recommended in ASTM D6641 [91]. The reported strain values were the average of the strain values measured from the front and the back gauges. Eqn (4.2) was then used to calculate the compressive modulus of each specimen. The average modulus for the five specimens was calculated to be equal to 46.6 GPa. This value is much lower than the 130.2 GPa modulus of the individual plies. This is expected since this is a quasi-isotropic laminate that contains 45° and 90° plies that reduce the longitudinal stiffness, but increase the transverse stiffness. The variation within the modulus values was very low. The results are summarized in Table 4.8.

Table 4.8 – Undamaged Compressive Modulus Results

Specimen	P_{3000} (N)	P_{1000} (N)	$\varepsilon_{x,3000}$ (με)	$\varepsilon_{x,1000}$ (με)	Modulus E_X (GPa)	Avg. Modulus E_X (GPa)	Stnd. Dev. (GPa)	Coeff. of Var. (%)
124	-8628	-2890	-3005.5	-990.0	47.6	46.6	0.6	1.2
117	-8345	-2800	-3004.0	-1005.0	46.4			
113	-8423	-2853	-3008.5	-1015.0	46.5			
107	-8233	-2698	-2998.0	-1002.0	46.1			
105	-8280	-2740	-3004.5	-996.5	46.3			

The ultimate compressive strength, S_{ult} , was calculated using the maximum force, P_{MAX} , applied to the specimen before failure as:

$$S_{ult} = \frac{P_{MAX}}{wt} \quad . \tag{4.5}$$

The average ultimate strength was equal to 621.8 MPa. The variation in the strength data, at 4.5%, was a little larger than the variation in the modulus results. Table 4.9 summarizes the compressive strength results for the undamaged specimens.

Table 4.9 – Undamaged Ultimate Compressive Strength Results

Specimen	Cross-Sectional Area A (mm^2)	Max Load P_{MAX} (N)	Ultimate Strength S_{ult} (MPa)	Average Strength S_{ult} (MPa)	Standard Deviation (MPa)	Coefficient of Variation (%)
124	59.9	-37718	-630.0	621.8	28.1	4.5
117	59.8	-36563	-611.4			
113	60.1	-36970	-614.8			
107	60.1	-35375	-588.3			
105	59.6	-39610	-664.5			

4.3.2 Damaged Specimens

4.3.2.1 Elastic Modulus

The effective compressive modulus, E_{CAI}, was calculated for five specimens at each impact energy level using Eqn (4.2) and the undamaged cross-section. The applied load was noted when the strain gauges on the specimens measured 1000 με and 3000 με as recommended in ASTM D7137 [95]. The reported strain values were the average of the strain values measured from the front and the back gauges. The results are shown in Table 4.10.

Table 4.10 - Damaged Compressive Modulus Results

Impact Energy P_E (J)	Specimen	P_{3000} (N)	P_{1000} (N)	$\varepsilon_{x,3000}$ (με)	$\varepsilon_{x,1000}$ (με)	Modulus E_{CAI} (GPa)
35	P1 11	-72575	-24478	-3000.0	-1000.0	51.0
	P1 25	-72230	-24360	-3000.5	-1001.0	50.8
	P1 38	-71093	-24163	-3001.0	-1000.0	49.8
	P1 51	-70270	-23700	-3000.5	-999.5	49.2
	P1 52	-71185	-24343	-3000.5	-1003.5	49.8
50	P1 5	-71265	-24470	-3000.0	-1000.0	49.5
	P1 7	-70870	-24345	-3000.5	-1000.0	49.3
	P2 31	-71005	-24033	-2999.5	-1000.5	49.9
	P2 35	-71265	-24473	-2999.5	-1001.0	49.5
	P2 36	-71568	-24645	-2999.0	-1000.0	49.7

The average effective compressive modulus at each of the impact energy levels, along with the results from the undamaged specimens are shown in Table 4.11. Globally, the damaged panels saw a marginal increase in stiffness compared to the undamaged panels. This is interesting to note since the local elastic modulus of the damaged area is expected to be reduced [22, 23].

Table 4.11 - Average Laminate Modulus Values

	Specimen Type	Undamaged	35 J	50 J
Modulus	Average (GPa)	46.6	50.1	49.6
	Standard Deviation (GPa)	0.6	0.8	0.2
	Coefficient of Variation (%)	1.2	1.5	0.4

4.3.2.2 Residual Strength

The compressive residual strength, S_{CAI} , of the specimens was calculated by recording the maximum force applied to the specimen before failure and the undamaged cross-sectional area as given in Eqn (4.5). Figure 4.11 shows a typical failed specimen while Table 4.12 summarizes the results.

Figure 4.11 – Damaged Specimen After Static Compression Failure

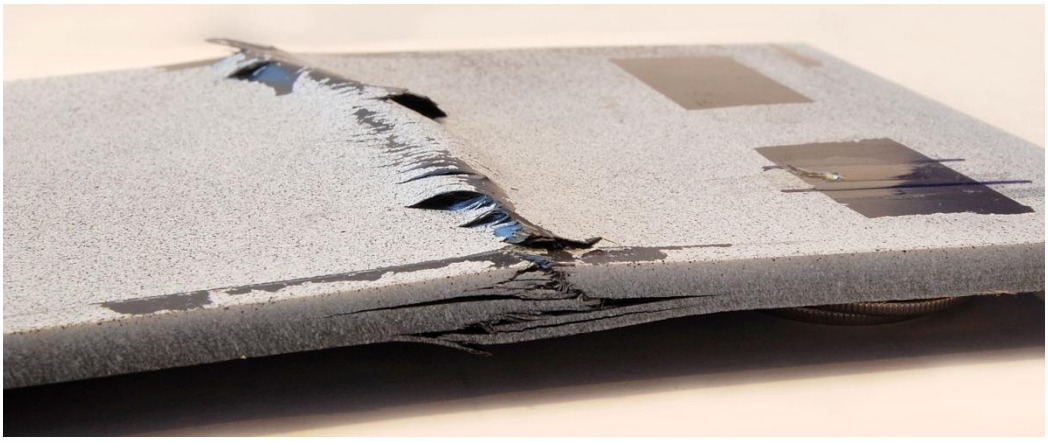

Table 4.12 – Compression After Impact Strength Results

Impact Energy P_E (J)	Specimen	Cross-Sectional Area A (mm^2)	Max Load P_{MAX} (N)	Residual Strength S_{CAI} (MPa)
35	P1 11	471.9	-144448	-306.1
	P1 25	471.2	-154613	-328.1
	P1 38	471.2	-144260	-306.2
	P1 51	473.4	-147898	-312.4
	P1 52	470.9	-149548	-317.6
50	P1 5	473.1	-137550	-290.7
	P1 7	471.5	-128958	-273.5
	P2 31	471.1	-130603	-277.2
	P2 35	472.8	-141750	-299.8
	P2 36	472.4	-130565	-276.4

The percent bending of P1 38 was below the 10% value recommended in ASTM D7137 [95] during most of the test. However, at failure the percent bending increased to 16%. The results for this test were included in the average strength calculation because the results were still within the range of the other specimens.

The average residual strength at each of the impact energy levels, along with the results from the undamaged specimens are shown in Table 4.13. The residual strengths of the 35 J and 50 J impacted specimens were only 50.5% and 45.6% respectively of the undamaged strength. This means that there is only a 5% difference in strength for a 15 J difference in impact energy. The large reduction from the undamaged strength, which matches closely with the work done by Xiong et al. [23] for a similar carbon/epoxy material and lay-up, is significant given the small geometry of the initial damage. An impact of this size may be difficult to observe, but can have a significant effect on the residual strength of the part.

Table 4.13 – Average Laminate Static Strength Values

	Specimen Type	Undamaged	35 J	50 J
Strength	Average (MPa)	-621.8	-314.1	-283.5
	Percent of Undamaged Strength (%)	N/A	50.5	45.6
	Standard Deviation (MPa)	28.1	9.2	11.3
	Coefficient of Variation (%)	-4.5	-2.9	-4.0

Figure 4.12 plots the residual strength as a percentage of the undamaged strength, against the impact energy level for both the test data provided above and for the data in Ref. [23]. It can be observed for both sets of data that the relationship is not linear. This agrees with the data from Ref. [3] for a woven carbon/epoxy material. However, it differs from the observed linear relationship in Ref. [14] for a multi-axial stitched CFRP laminate.

Figure 4.12 – Residual Strength vs. Impact Energy

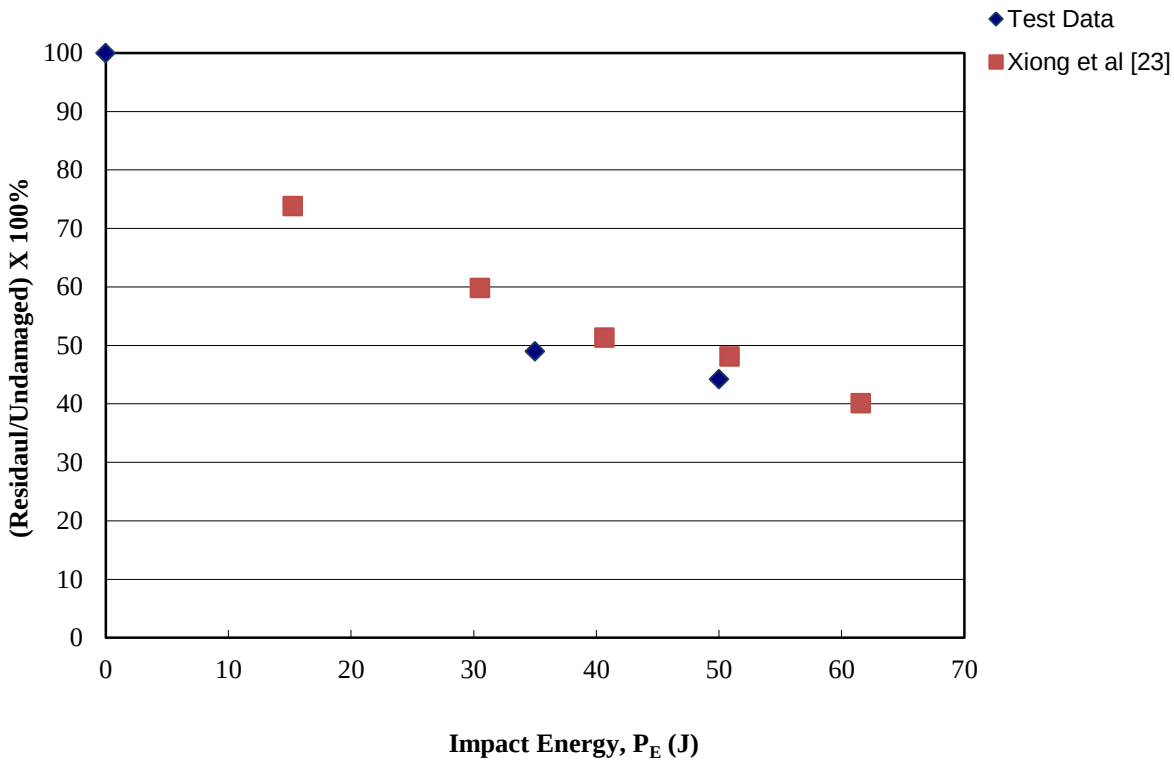

As stated in Section 4.2.2, the preliminary data suggests that there is a linear relationship between damage area measured by ultrasonic C-scan and impact energy. That information, combined with Figure 4.12 shown above, suggests that with more data points at lower impact energy levels, a relationship could be described between the damage area and residual strength as was done in Ref. [3]. This could be a valuable tool to predict the residual strength of a laminate that has been damaged by an unknown impact energy level by non-destructively measuring the damage area.

4.3.2.3 Strain and Stress Concentration Factors from Static Testing

The digital image correlation system was used to measure the axial strain field during the static tests. Figure 4.13 shows how the axial strain pattern in the specimen changes during the testing. The load is applied in the left-right direction of the figure. At the lowest load levels the strain pattern can not be determined due to the noise in the DIC signal. A small oval shaped strain concentration then appears and continues to grow as the load increases. It can be seen that immediately before failure the area of maximum strain is in an oval shape that extends in the direction perpendicular to the applied load. There is an area of strain relief that is located directly above and below the damage location.

Figure 4.13 – Axial Strain Pattern During Static Testing

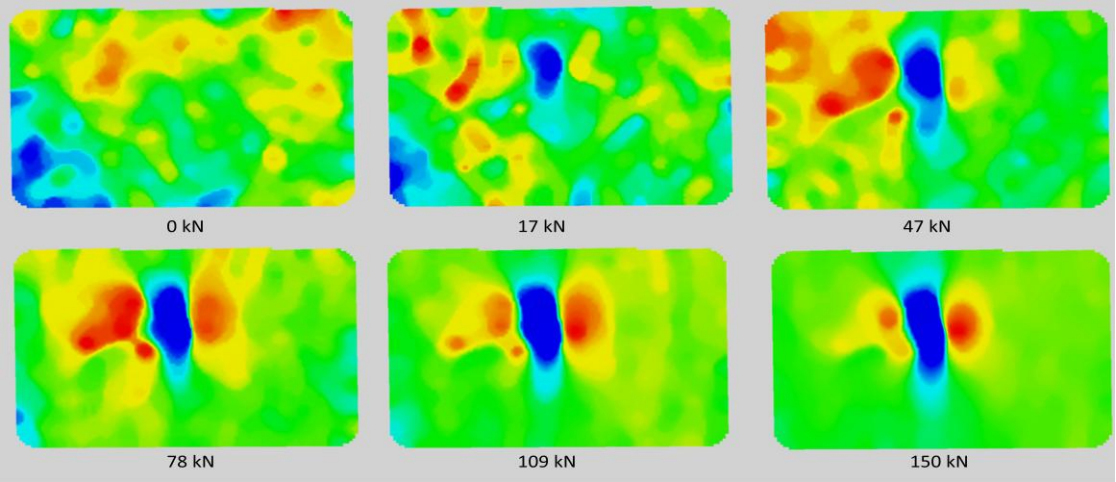

Typical stress-strain curves measured using the DIC system for the damaged specimens, and strain gauges for the undamaged specimen, are shown in Figure 4.14. The curve for the undamaged specimen, which was discussed in detail in Section 4.3.1, remains linear until a stress of approximately 300MPa is applied and then becomes slightly non-linear at higher loads. As expected, the strains in the far-field of the damaged specimens match closely with those of the undamaged specimen. The local strain at the damage location remains linear during the initial loading for both the 35 J and 50 J specimens. However, the curves quickly become non-linear due to the non-linear increase of strain in the damage regions. It can also be observed that the non-linearity of the curve is greater for the 50 J specimen than the 35 J specimen. This is due to the greater initial damage inflicted on the 50 J specimen.

Figure 4.14 – Stress - Strain Curves for Static Testing

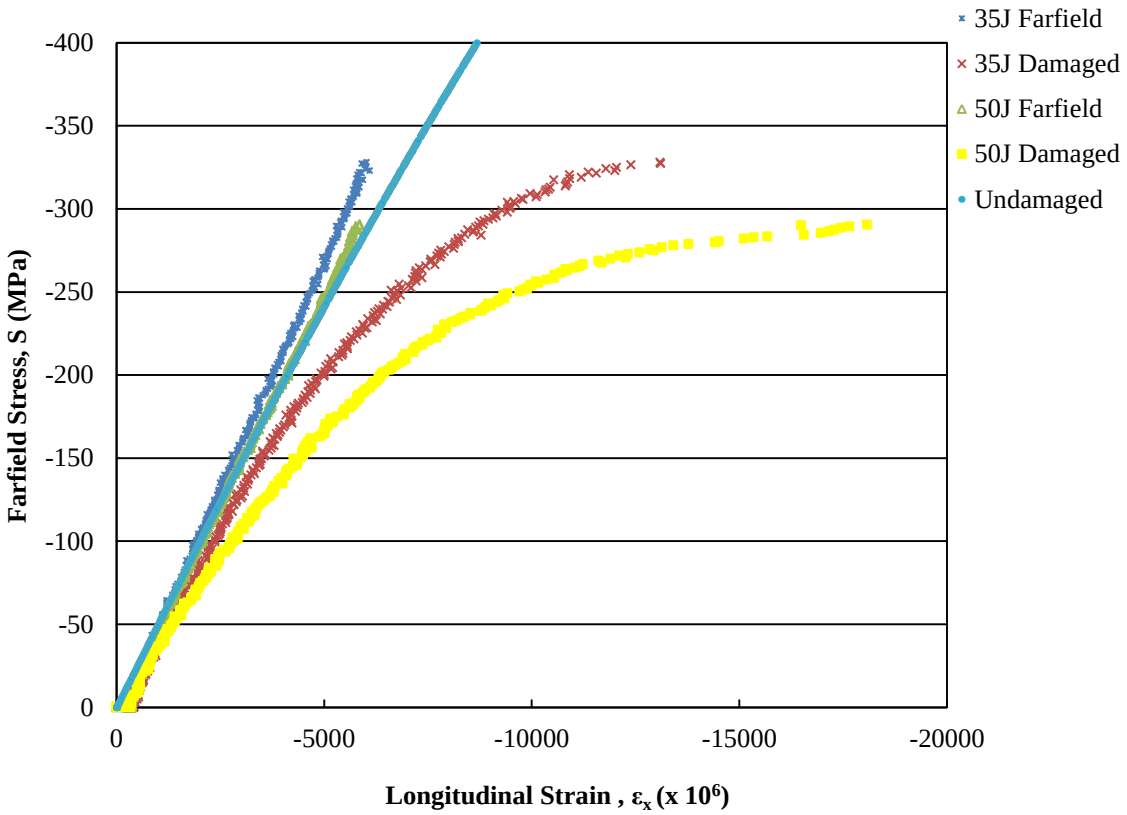

It was observed in Figure 4.13 that a strain concentration was visible at the damage location. The maximum strain at the damage location, ε_{local}, can be compared to the far-field strain as measured by the DIC system, $\varepsilon_{farfield,DIC}$. This data can be used to calculate a strain concentration factor (SCFε) for each specimen by using the equation,

$$SCF_{\varepsilon} = \frac{\varepsilon_{local}}{\varepsilon_{farfield,DIC}} . \qquad (4.6)$$

Figure 4.15 shows how the SCFε varies with applied axial stress for a typical specimen that was impacted at 50 J. The SCFε appears to increase at a non-linear rate during the first 50 MPa of applied stress. This is not a real trend but is due primarily to noise in the DIC signal at low levels of strain. The SCFε then appears to increase at a very low linear rate until a stress of approximately 200 MPa is applied. At this point the

SCFε increases in a non-linear fashion until failure. Figure 4.14 shows that the stress-strain curves for the damaged specimens have also become non-linear by an applied stress of 200 MPa. The observed non-linear increase in SCFε and non-linearity in the stress-strain curves is probably due to the creation and propagation of internal damage in the specimen.

Figure 4.15 – Changes in SCFε with Applied Stress

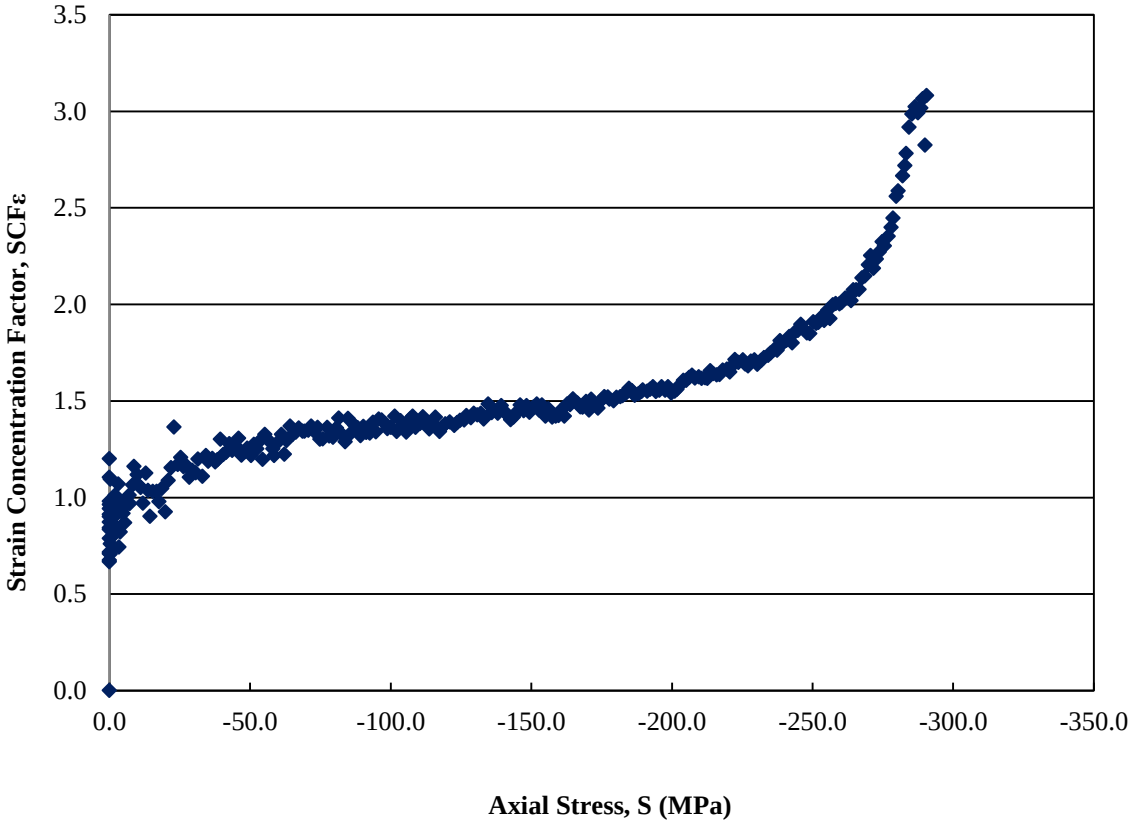

It can be observed that the SCFε varies with small changes in load due to the noise in the system. For this reason an average linear strain concentration factor ($SCF\varepsilon_{linear}$) was calculated for each specimen between loads of -85 MPa and -200 MPa. This range was chosen because at -85 MPa the noise in the DIC strain readings is minimized, and at -200 MPa the stress-strain curves of the damaged specimens have become non-linear. A summary of the $SCF\varepsilon_{linear}$ for each specimen is given in Table

4.14. The average $SCF\varepsilon_{linear}$ for the 35 J specimens was 1.28 and was 1.41 for the 50 J specimens. Given the standard deviations of the results, this is an appreciable but small difference. It also appears that the $SCF\varepsilon_{linear}$ showed less scatter at the higher impact energy level.

Table 4.14 – $SCF\varepsilon_{linear}$ Summary

Impact Energy P_E (J)	Specimen	$SCF\varepsilon_{linear}$ per Specimen	Average $SCF\varepsilon_{linear}$	Standard Deviation	Coefficient of Variation (%)
35	1-11	1.24	1.28	0.10	8.0
	1-25	1.24			
	1-38	1.31			
	1-51	1.17			
	1-52	1.44			
50	1-5	1.45	1.41	0.05	3.4
	1-7	1.46			
	2-31	1.34			
	2-35	1.41			
	2-36	1.38			

The average $SCF\varepsilon_{linear}$ was plotted against impact energy in Figure 4.16 with the assumption that the $SCF\varepsilon_{linear}$ was equal to 1 when the impact energy was zero. From this limited data it can be observed that the average $SCF\varepsilon_{linear}$ appears to increase linearly with impact energy. As discussed in Section 4.2.2, it is likely that this laminate has a threshold impact energy level below which no damage will occur. Therefore, by assuming that the $SCF\varepsilon_{linear}$ is equal to one at an impact energy of zero, the graph will over predict the $SCF\varepsilon_{linear}$ for a given impact energy level. This means that the graph is conservative in nature.

Horn et al. [81] found a similar linear relationship between impact energy and the average stress concentration factor ($SCF\sigma$) for impact damaged injection moulded

glass/polyurethane specimens. Their data is also plotted in Figure 4.16. The linear relationship is much steeper for their specimens. This is because a different material and lay-up were used. The glass specimens are less damage tolerant and it can be observed that for a given impact energy level the SCFσ is larger for the glass specimens.

It should be noted that the average damage area measured by ultrasonic C-scan also had a linear relationship with impact energy as shown in Figure 4.7. However, no direct relationship could be found when the damage area and the $SCF\varepsilon_{linear}$ for each individual specimen were plotted against each other.

Figure 4.16 – Average Concentration Factor vs. Impact Energy

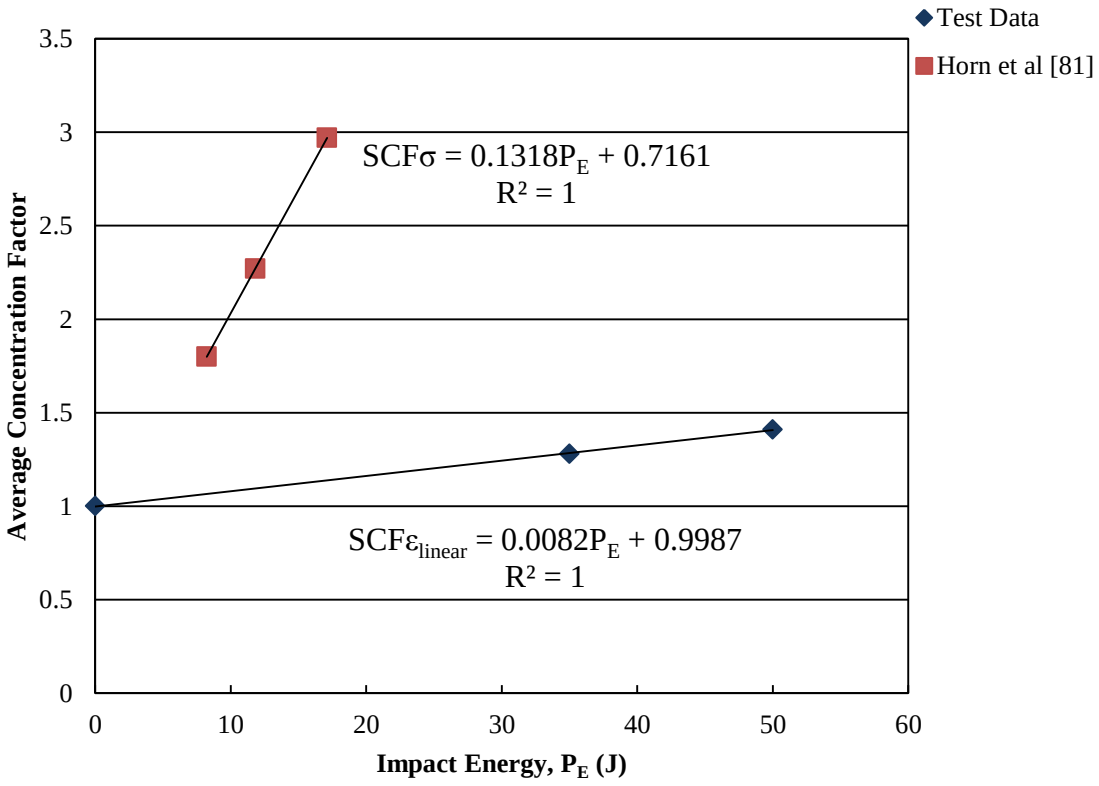

The analysis described in the following sections assumes that the strain concentration factor is equal to the stress concentration factor (SCFε = SCFσ). At low load levels, such as the linear portions of Figures 4.14 and 4.15, this is most likely a good

assumption. However, Tan [98] states that as microdamage occurs around a hole in a laminate, the local stress becomes unknown because the local stiffness is no longer the same as that of the undamaged laminate, and the stress concentration factor is no longer equal to the strain concentration factor. This means that at high load levels, as the damage starts to propagate, the SCFε and SCFσ are no longer equal to each other. There is no easy method for quantifying this difference.

In Refs. [15], [22], and [23] the authors measured the damage area of a variety of impact damaged composite laminates using ultrasonic C-scan and then modelled the damage as elliptical soft inclusions. They performed sublaminate stability analyses to find the effective reduced stiffness of the impact damage zones. Stress concentrations associated with the reduced stiffness were then calculated. With further research this may prove to be a potential method of correlating the SCFε and SCFσ data at higher load levels.

4.3.2.4 Out-of-Plane Deformation

The impact causes a permanent out-of-plane indentation on the front face of the specimen which increases in depth during the loading. The DIC system recorded the displacement in the z (out-of-plane) direction during the static testing. Melin et al. [61] referred to the out-of-plane deformation as the amplitude of buckling. They determined that predictions of static compressive failure strain and fatigue limit were improved when the buckling area as measured by digital image correlation was used instead of the damage area measured by C-scan.

Although not the primary focus of this study, the out-of-plane deformation of the specimens was examined. Figure 4.17 shows the out-of-plane displacement for a specimen impacted at 35 J. The shape of the through thickness deformation is an oval and remains relatively constant for the duration of the test. In this case the z-displacement is in the negative direction and indicates that the front surface is buckling into the specimen. The depth and size of the deformation on the front side of a typical specimen is shown in Figure 4.18 for the cross-section shown in Figure 4.17 that passes through the impact location and perpendicular to the applied load. The top line is the deformation at zero load. Each line in the graph shows the displacement for an approximate increase of 9250 N.

An exponential relationship can be found to describe the increase in the damage depth with load as shown in Figure 4.19. An exponential relationship can also be observed in the stress-strain graphs of the damaged specimens and indicates that there may be some form of relationship between the increase in strain at the damage location and the depth of the out-of-plane deformation. Further testing is required to determine if a relationship exists and what form it may take.

Figure 4.17 – Shape of Out-of-Plane Indentation During Static Testing

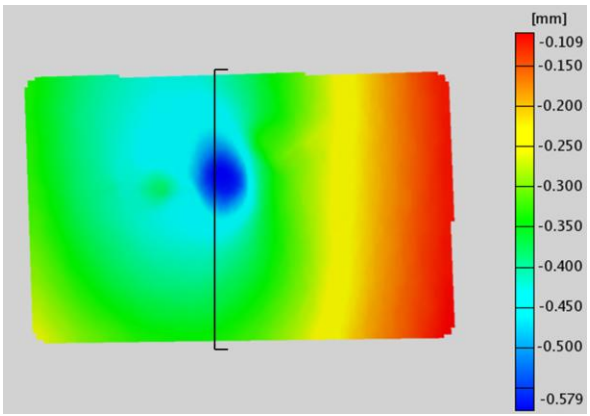

Figure 4.18 – Depth of Damage During Static Testing

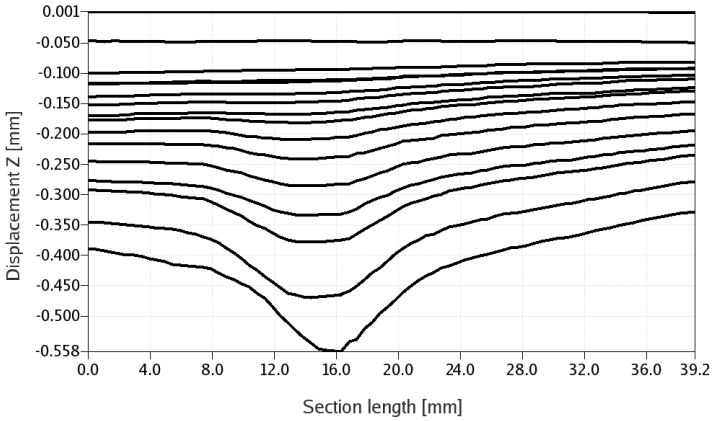

Figure 4.19 – Increasing Depth of Damage vs. Load During Static Test

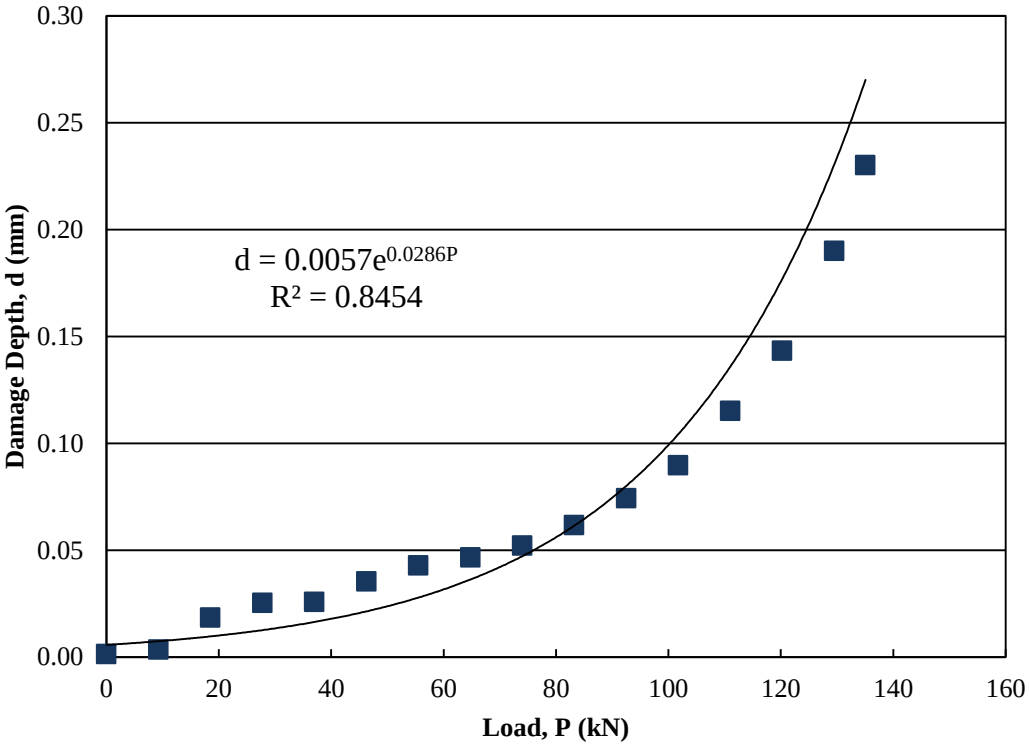

4.4 Fatigue Testing

Compression-compression fatigue testing was performed on the undamaged and damaged specimens. All fatigue tests were performed in load control at a stress ratio of R = 10 and at a frequency of 5 Hz. Seventeen undamaged specimens were tested in order to provide baseline fatigue data for this material and lay-up. Sixteen specimens were tested at each of the impact energy levels.

In this section the strain fields and depth of the damage recorded by DIC are presented, along with the stress-life curves for the undamaged and damaged specimens. Strain and stress concentration factors are calculated and applied to the data. Attempts are also made to correlate the fatigue data using non-destructive evaluation results and by normalizing the data using residual strength as was done by Yuanjian and Isaac [75]. Finally, the post-impact fatigue model developed by Kang and Kim [76] is examined.

4.4.1 Strain Field

The DIC system was used to track changes in the strain field as the fatigue test proceeded. Figure 4.20 shows a typical failed specimen after fatigue loading. For all specimens the maximum axial far-field strain remained virtually constant throughout the fatigue tests. However, three different trends in the strain at the damage location were observed for both the 35 J and 50 J specimens.

Figure 4.20 – Damaged Specimen After Fatigue Compression Failure

The first trend can be observed in Figure 4.21. The graph shows the axial strain at the damage location recorded at the peak compression load for a 50 J impacted specimen that was loaded at 79% CAI and failed at the damage region after 102972 cycles. It can be observed that the strain at the damage location increased linearly for most of the test. The strain began to increase in a non-linear, accelerating fashion close to failure.

Figure 4.22 shows the changes of the axial strain field as the test proceeds for the same specimen shown in Figure 4.21. The region of highest strain starts as a small dark oval. The longitudinal axis of the oval lies perpendicular to the direction of the applied load. As the test continues the strain concentration becomes more pronounced and the length of the oval increases. As the test proceeds the value of the strain directly above and below the damaged area decreases in an area of strain relief.

Figure 4.21 – Fatigue Test with Linearly Increasing Strain

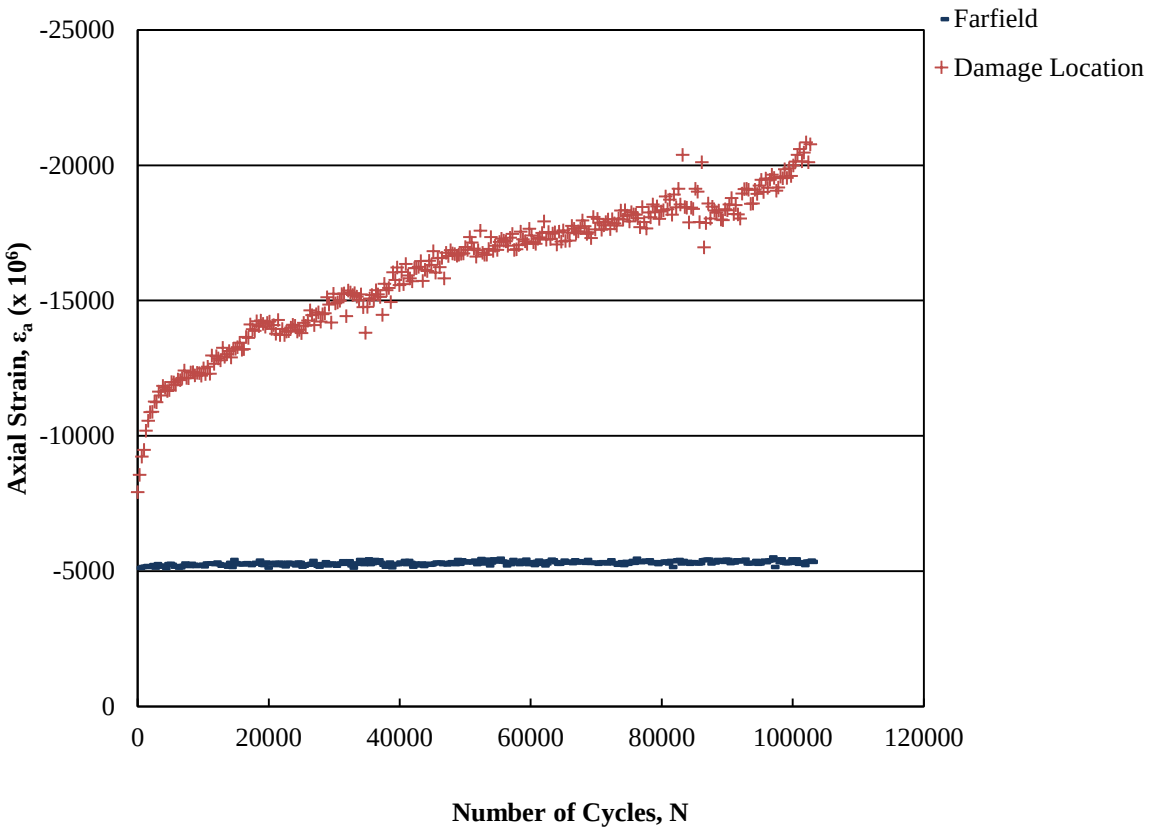

Figure 4.22 – Linearly Increasing Strain Field

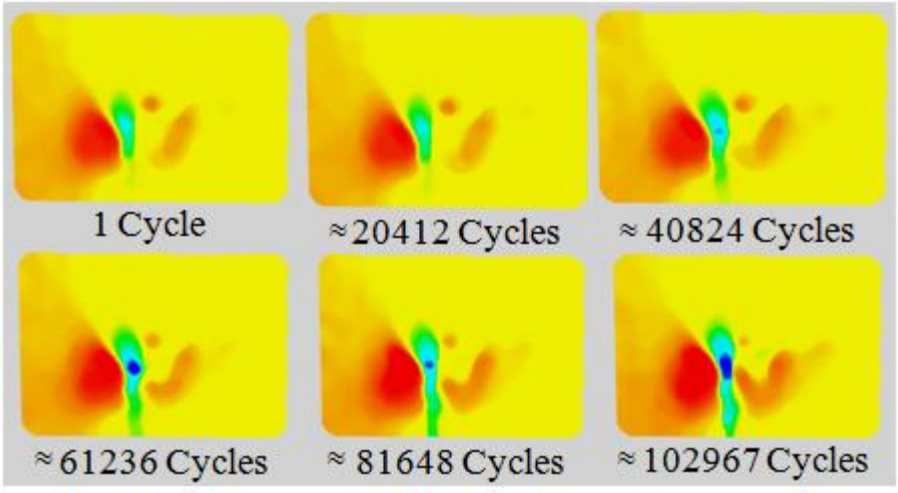

The second observed trend is displayed in Figure 4.23. This figure shows a 50 J impacted specimen that was loaded at 89% CAI and failed at the damage location after 80687 cycles. In this case the strain at the damage location remains constant for the duration of the test including up to failure.

Figure 4.24 shows that there is almost no change in the axial strain field as the test proceeds for the same specimen shown in Figure 4.23. The only noticeable change occurs directly before failure. The strain concentration remains constant, but the size of the strain relief area suddenly expands. This occurred in many of the specimens in which the strain remained constant throughout the test.

Figure 4.23 – Fatigue Test with Constant Strain

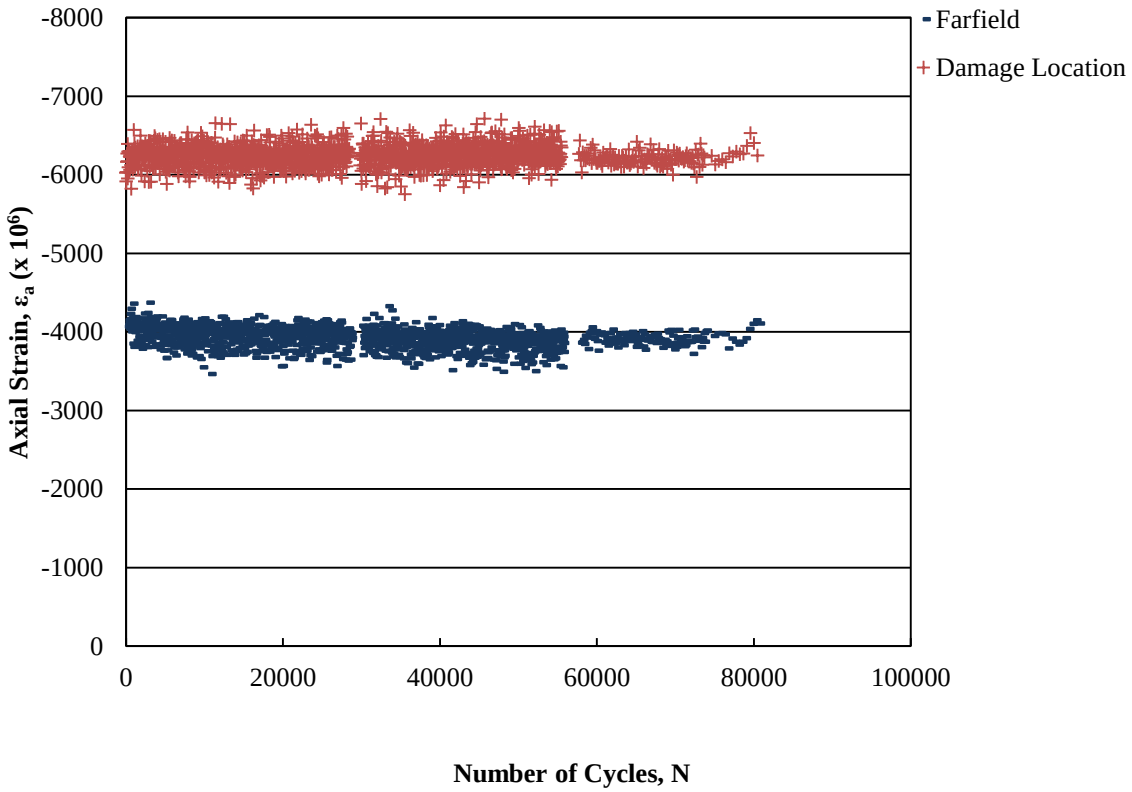

Figure 4.24 – Constant Strain Field

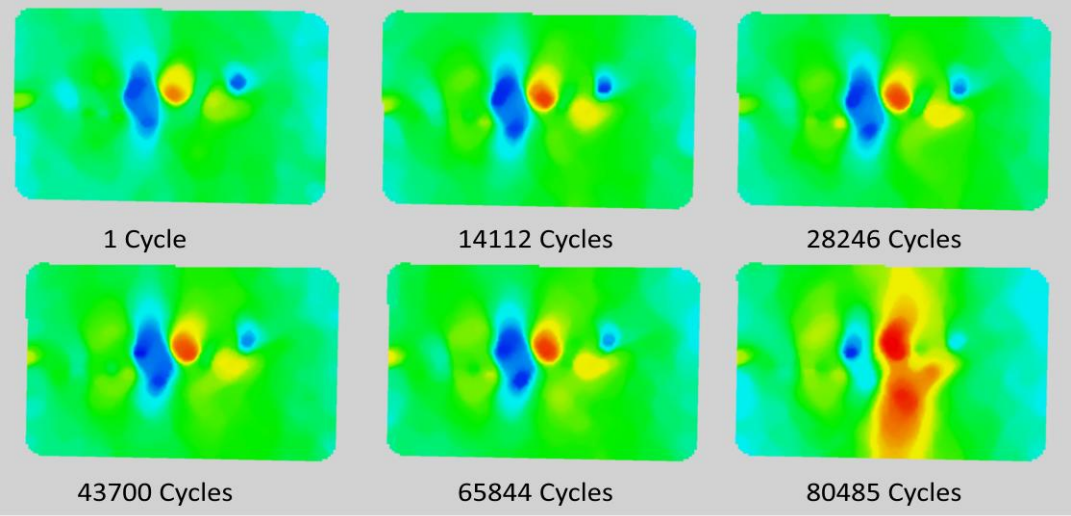

The last observed trend saw the strain at the damage location remain relatively constant until right before failure at which point the strain increased rapidly. This trend is shown in Figure 4.25 for a 50 J impacted specimen that was loaded at 79% CAI and failed at the damage location after 143603 cycles.

Figure 4.26 shows the changes of the axial strain field as the test proceeds for the same specimen shown in Figure 4.25. At the start of the test there is an oval of increased strain with the longitudinal axis perpendicular to the load and an arm projected in the loading direction. Very few changes in the strain field are noticed until the last 10000 cycles. At this point the areas of higher strain increase in size and the strain concentration becomes more pronounced.

Figure 4.25 – Fatigue Test with Increasing Strain at End of Life

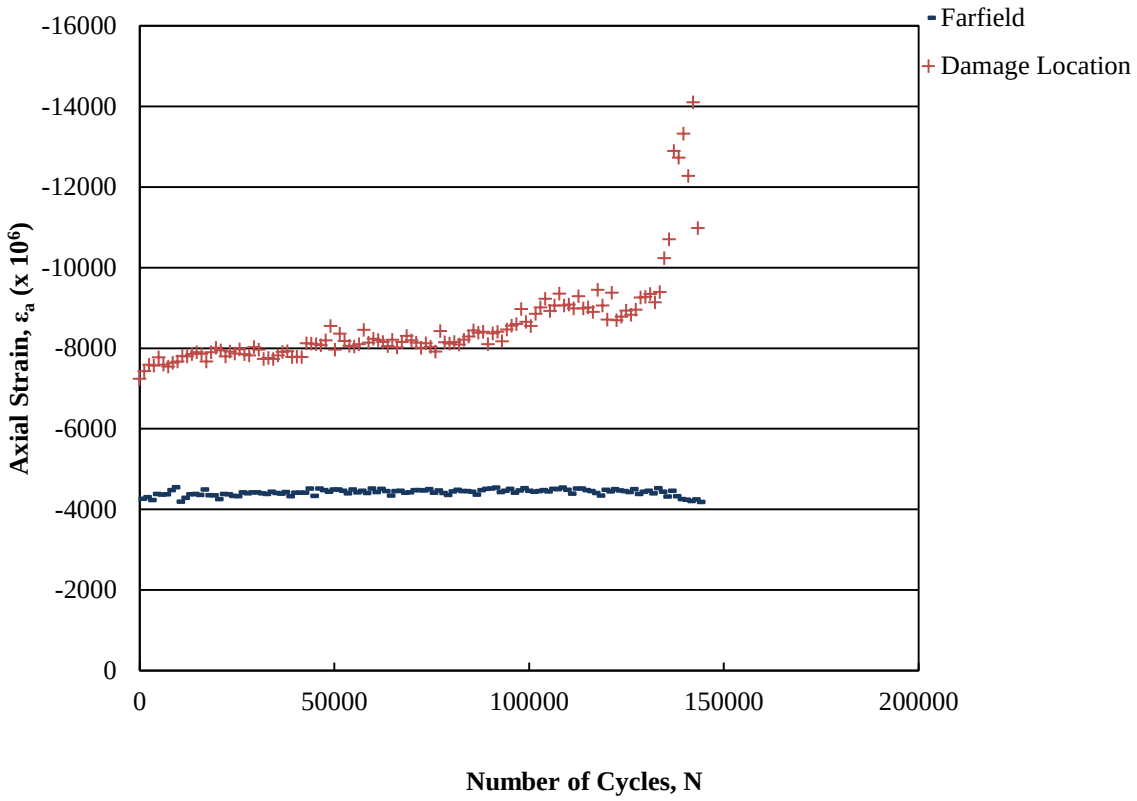

Figure 4.26 – Increasing Strain Field at End of Life

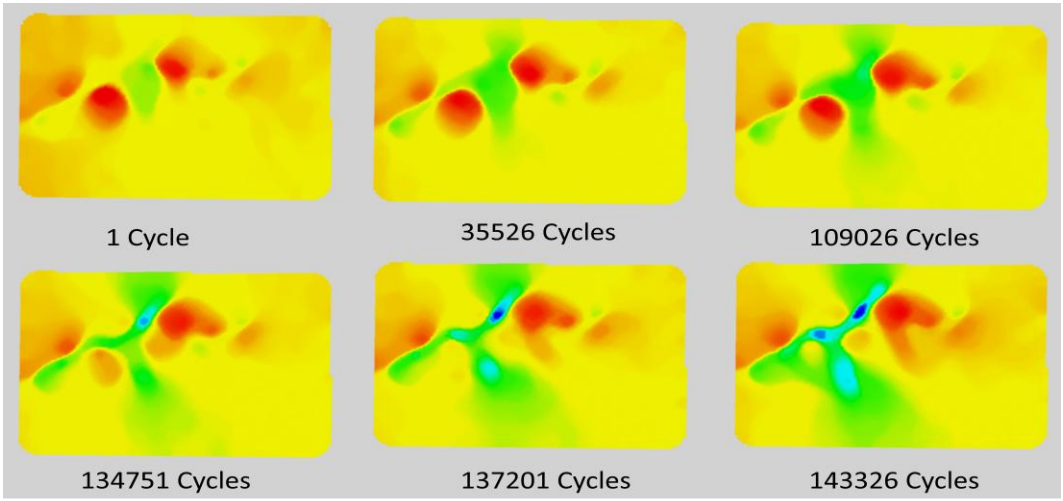

The authors in Ref. [35] and Ref. [37] divided the fatigue damage formation into two stages for undamaged composite material fatigue tests. The first stage had a decelerating rate of damage where small cracks in the matrix form and grow. The second stage demonstrates an accelerating rate of damage in which delaminations grow leading eventually to fibre breakage. The process described in Ref. [31] is very similar except that the first stage is split into two; the initial decelerating portion, and the constant growth stage. For most of the test specimens the initial decelerating stage was not present or was very small. This is due to the fact that the impact event had already created cracks in the matrix so the first part of the damage formation process had already taken place.

The strain increased non-linearly at the end of life during both the first and third trend. This result agrees well with the damage progression in undamaged fatigue tests discussed above. The constant strain observed in the third trend at low cycle numbers can be attributed to the formation and growth of matrix cracks as stated in Ref. [35] and Ref. [37]. The linear increase in strain observed in the first trend at low cycle numbers is probably due to a combination of both damage formation and propagation.

This doesn't explain why the strain does not increase at the end of life for the constant strain specimens. To investigate this further Eqn (4.6) from Section 4.3.2.3 was used to calculate a strain concentration factor (SCFε) for each of the specimens during peak loading at 50 cycles. Table 4.15 lists the SCFε for each specimen and the corresponding trend in the strain data.

Table 4.15 – Strain Trends During Fatigue Testing

Impact Energy, P_E (J)					
35 J			50 J		
Specimen	SCFε	Change in Strain	Specimen	SCFε	Change in Strain
1-32	2.37	NA	2-30	2.67	Linear
1-34	2.28	NA	2-29	2.42	Linear
2-4	1.93	Non-linear End of Life	2-38	2.40	NA
2-1	1.73	Non-linear End of Life	1-4	2.01	Non-linear End of Life
2-23	1.72	Linear	1-2	2.01	Non-linear End of Life
2-20	1.71	Non-linear End of Life	1-16	2.00	Non-linear End of Life
1-21	1.71	Non-linear End of Life	2-32	1.89	NA
2-16	1.59	Linear	1-19	1.89	No Change
2-19	1.57	Non-linear End of Life	1-44	1.82	Non-linear End of Life
2-8	1.57	Linear	1-17	1.80	Non-linear End of Life
2-2	1.52	No Change	1-8	1.77	Non-linear End of Life
2-17	1.45	No Change	1-20	1.76	Linear
2-12	1.44	No Change	2-37	1.66	No Change
2-11	1.44	No Change	2-28	1.60	Non-linear End of Life
2-9	1.41	No Change	2-33	1.42	No Change
2-25	1.40	No Change	1-22	1.41	No Change

It appears that for those specimens with a lower SCFε, the maximum strain remains constant throughout the fatigue test, as in Figure 4.23. As the SCFε increases, it is more likely to observe the axial strain increasing linearly during the fatigue test or increasingly non-linearly at the end of life. The smaller SCFε also explains why more of the 35 J specimens displayed the constant strain trend than the 50 J specimens, since the average SCFε is smaller for the 35 J specimens. Four of the specimens list the trend as not available. This was due to the DIC system capturing only a couple of pictures before failure. The data was too limited to draw any conclusions for these specimens.

One possible explanation for why the strain remains constant for specimens with lower SCFε values may be related to observed changes in the strain field close to failure.

Often the size or degree of the strain relief directly next to the strain concentration increased directly before failure as shown in Figure 4.24. This may indicate that the stiffness in the region has decreased significantly and might have caused local instability in the panel leading to failure.

4.4.2 Out-of-Plane Deformation

The out-of-plane deformation in the damage region was examined for the fatigue tests after an exponential relationship between the out-of-plane deformation and load was found during static testing. It was observed that for almost all of the specimens the z-displacement, that is a measure of the out-of-plane deformation in the damage region, increased during the fatigue test. Figure 4.27 displays the out-of-plane displacement near failure for a typical specimen. The depression at the damage location is clearly visible in the centre of the specimen.

Figure 4.27 – Negative Out-of-Plane Displacement Near Failure

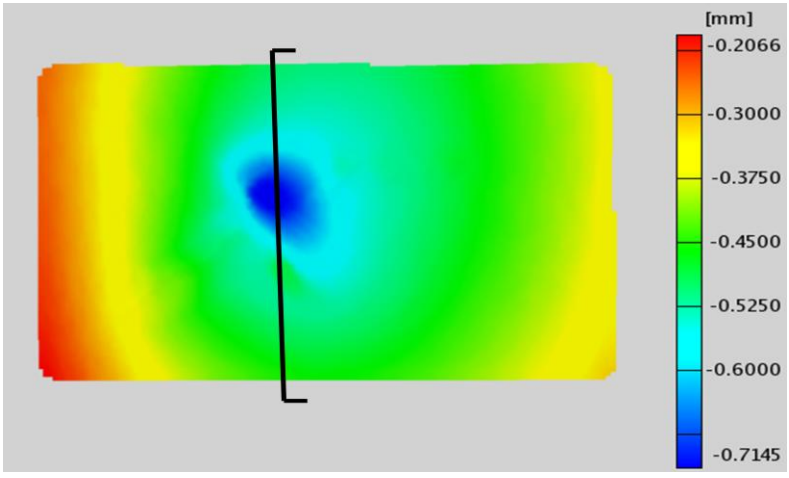

The lines in Figure 4.28 represent the out-of-plane deformation along the section line shown in Figure 4.27. The topmost line shows the deformation at 0 cycles and each

new line shows the deformation after an additional 35 cycles. The z-displacement is in the negative direction and indicates that specimen is globally bending away from the camera. It also shows that the front surface of the damage region is buckling into the specimen.

Figure 4.28 – Global Negative Bending – Increasing Damage Deformation as Fatigue Test Proceeds

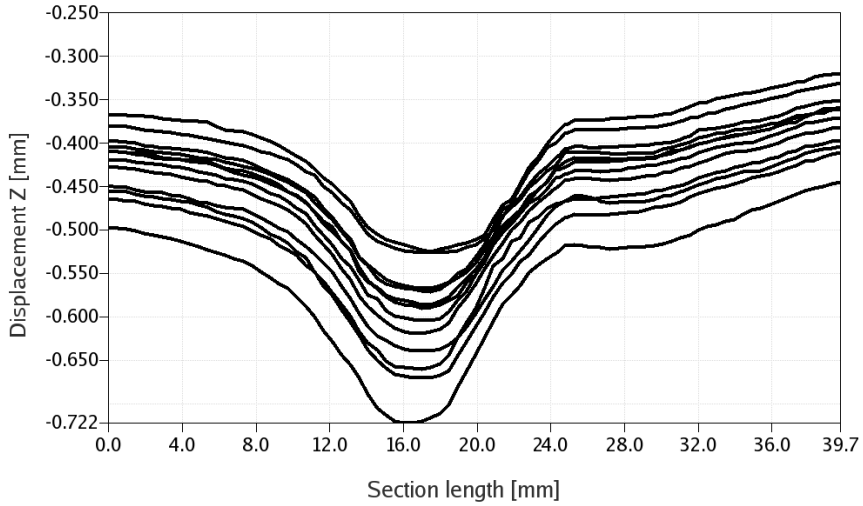

Figure 4.29 shows the out-of-plane displacement immediately before failure for another typical specimen. It can be observed that globally the specimen is bending forwards, towards the camera, but a depression is visible at the damage region.

Figure 4.29 – Positive Out-of-Plane Displacement Near Failure

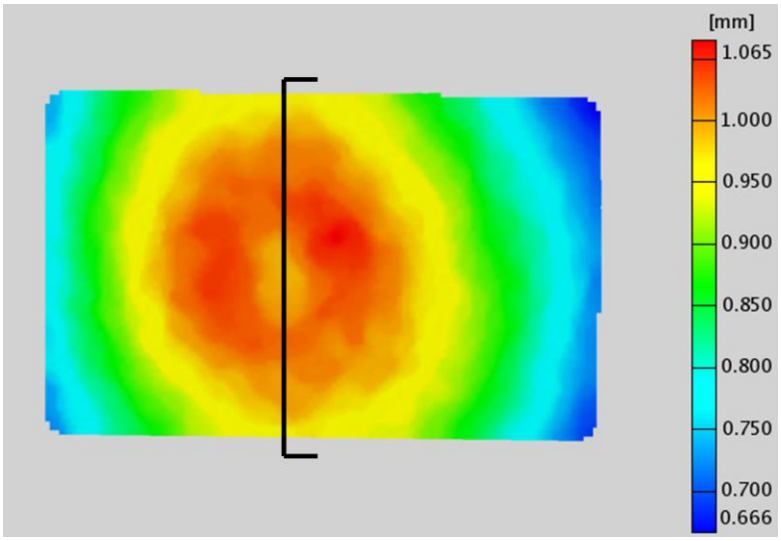

The lines in Figure 4.30 represent the out-of-plane deformation along the section line shown in Figure 4.29. The bottom line shows the deformation at 0 cycles and each new line shows the deformation after an additional 1000 cycles. Despite the global positive bending, the out-of-plane displacement at the damage location still appears to increase in the negative direction. This means that the front surface of the damage region is still buckling into the specimen.

Figure 4.30 – Global Positive Bending – Increasing Damage Deformation as Fatigue Test Proceeds

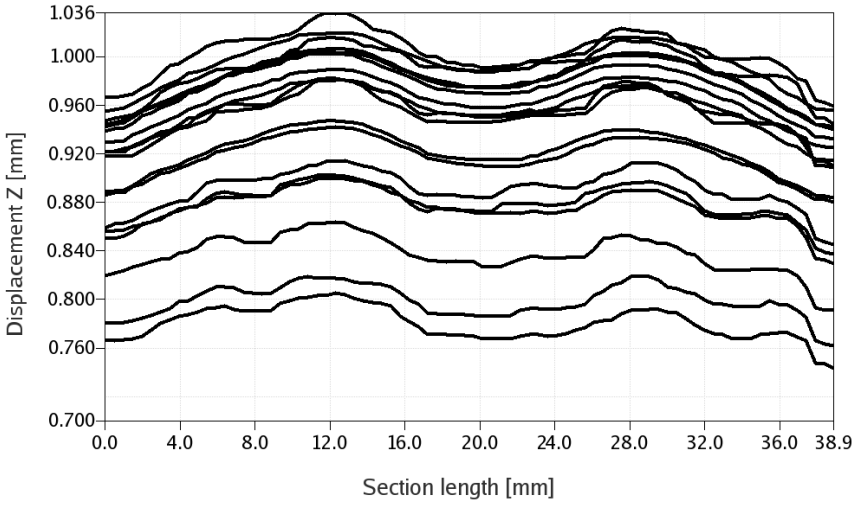

No consistent trend in either the size of the deformation or the rate of increase could be found between the specimens or impact energy levels. There did not appear to be any correlation between the out-of-plane deformation and either the SCFε or the stress amplitude. The average deformation was larger for the 50 J specimens, but the scatter between the specimens was extremely high. It appears that the out-of-plane deformation and its rate of increase are not reliable factors for predicting fatigue life. However, it is interesting to note that the out-of-plane deformation of the damage increased even for specimens where the strain did not increase at the damage location during the fatigue test, such as the specimen shown in Figure 4.23.

4.4.3 S-N Curve for Undamaged Samples

Compression-compression fatigue tests were performed on undamaged specimens by varying the applied stress amplitude. Table 4.16 shows the fatigue data including minimum and maximum applied stress, stress amplitude, and number of cycles until failure. The settings on the load frame were adjusted to try to achieve a stress ratio of R = 10. In reality the stress ratio varied between 8.8 and 10.2 with an average value of 9.7. The variation in the stress ratio was due to the capabilities of the load cell. The applied loads were at the bottom end of the load cell range and this made it difficult for the control system to consistently apply the same load throughout the test.

Table 4.16 – Fatigue Data for Undamaged Specimens

Specimen	Min Stress S_{MIN} (MPa)	Max Stress S_{MAX} (MPa)	Stress Amplitude S_a (MPa)	Cycles to Failure N
126	-48.3	-493.3	-222.5	57652
134	-49.2	-488.4	-219.6	218949
136	-50.7	-503.7	-226.5	182757
137	-52.5	-511.6	-229.5	49928
138	-55.7	-523.4	-233.9	34869
139	-47.7	-485.4	-218.9	159057
142	-59.6	-547.9	-244.2	6631
143	-63.5	-576.7	-256.6	5781
145	-61.7	-601.8	-270.1	941
146	-61.1	-609.5	-274.2	646
147	-64.0	-634.5	-285.3	264
148	-68.6	-656.7	-294.1	51
149	-53.0	-504.1	-225.6	39885
150	-67.2	-661.6	-297.2	35
151	-62.9	-581.3	-259.2	9101
152	-61.1	-534.8	-236.8	7304
154	-46.0	-467.2	-210.6	387844

Care had to be taken when tightening the bolts on the fixture during this test in order to promote acceptable failure modes. When a low torque value was applied to the bolts many of the specimens failed by end splitting in the grip section. However, when the torque value was increased, more of the specimens began to fail at the end of the gauge section where the fixture began to grip the specimen. This was due to high clamping forces inducing a stress concentration at this location. Any specimens that failed due to end splitting or at the end of the gauge section were discarded.

An attempt was made to record the temperature rise in each of the specimens during the fatigue test. This proved to be difficult due to the small gauge length and extremely high strain in the specimen. Due to the small gauge length only a small bead of epoxy could be used to attach the thermocouple to the specimen. For many of the specimens the thermocouple became detached during the testing due to the high strain and vibrations of the testing.

For those tests where temperature data was successfully recorded, the temperature rose between 4.4°C at low stress amplitudes, to 11.9°C at high stress amplitudes. This temperature rise exceeds the recommended temperature rise of 2.8°C in MIL-HDBK-17-1F [96]. The increased temperature could potentially affect the fatigue data due to creep effects. However, if creep was a factor during the tests the measured fatigue lives would be shortened, and thus the data is conservative.

The alternating stress was plotted against the number of cycles to failure for each specimen and is shown in Figure 4.31. The data follows a logarithmic trend and has a R^2 value of 0.954, indicating a good fit with the data. From the logarithmic trend the fatigue

limit for one million cycles is estimated to be -449.5 MPa, which is 72% of the measured static strength. This fatigue limit is higher than for most metals and indicates that this carbon/epoxy laminate performs well under fatigue loading conditions when there is no out-of-plane damage.

Figure 4.31 – Stress - Life Curve for Undamaged Specimens

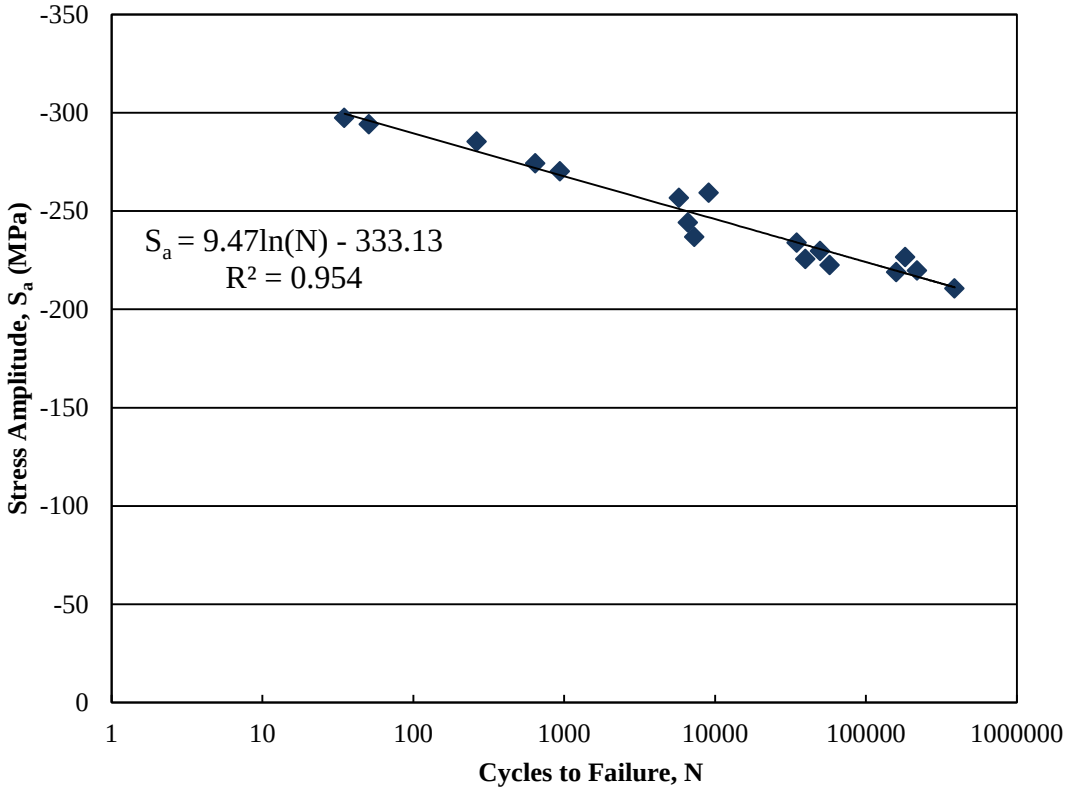

4.4.4 S-N Curves for Damaged Samples

Compression-compression fatigue tests were performed on both the 35 J and 50 J impacted specimens. Summaries of the tests are provided in Tables 4.17 and 4.18 for the 35 J and 50 J specimens respectively. The average stress ratios were 8.8 for the 35 J specimens and 8.3 for the 50 J specimens. These values were both lower than the average stress ratio of 9.7 that was applied to the undamaged specimens. The differences were due to difficulties in controlling the applied loads at high frequencies.

Table 4.17 – Fatigue Data for 35 J Impacted Specimens

Specimen	Min Stress S_{MIN} (MPa)	Max Stress S_{MAX} (MPa)	Stress Amplitude S_a (MPa)	Cycles to Failure N
2-1	-28.2	-240.6	-106.2	61730
2-8	-28.9	-245.8	-108.4	102744
2-2	-30.4	-263.4	-116.5	300854
2-20	-31.3	-269.0	-118.8	53168
2-4	-31.7	-274.8	-121.6	4919
2-9	-32.4	-280.9	-124.2	189903
2-17	-32.6	-286.5	-126.9	194157
2-19	-30.3	-266.1	-117.9	257760
2-12	-33.3	-292.1	-129.4	377751
2-11	-34.0	-298.0	-132.0	12810
2-25 *	-35.4	-305.7	-135.2	20822
2-23	-36.0	-308.2	-136.1	401
1-21	-33.9	-300.1	-133.1	10490
2-16	-35.6	-311.7	-138.0	2037
1-34	-31.3	-312.4	-140.5	4
1-32	-31.1	-294.2	-131.5	2

Table 4.18 – Fatigue Data for 50 J Impacted Specimens

Specimen	Min Stress S_{MIN} (MPa)	Max Stress S_{MAX} (MPa)	Stress Amplitude S_a (MPa)	Cycles to Failure N
2-32	-29.5	-252.8	-111.6	17050
1-20 *	-26.3	-224.2	-99.0	102972
1-19	-30.0	-252.5	-111.3	4561
1-8	-27.7	-238.5	-105.4	78459
2-29	-32.3	-266.1	-116.9	224
1-2	-29.8	-252.7	-111.4	418
1-4 *	-32.6	-265.7	-116.6	168
1-44 *	-28.6	-238.1	-104.8	7231
2-30	-32.4	-265.0	-116.3	44
1-22 *	-29.7	-252.4	-111.4	80687
2-28	-26.5	-224.4	-99.0	143603
1-17	-28.4	-237.9	-104.7	82739
2-38 *	-28.4	-232.2	-101.9	172
2-37	-31.6	-260.1	-114.2	85899
2-33	-27.4	-226.8	-99.7	685421
1-16 *	-30.7	-242.8	-106.0	14724

No standard currently exists for compression-compression fatigue testing of composite materials, but ASTM D7137 [95] recommends that the percent bending in a damaged composite specimen is kept below 10% during static residual strength testing. An attempt was made to keep the percent bending below 10% during the fatigue tests. At the start of the tests all of the specimens had percent bending values below 10%. The specimens in the above tables marked with a * had percent bending values between 10% and 12% at a later number of fatigue cycles. The exception is specimen 1-22 that had a percent bending value of 16% near failure.

As stated in the previous section, MIL-HDBK-17-1F [96] recommends that the specimen temperature rise during fatigue testing of composites remains below 2.8°C. The temperature rise in the majority of specimens at both the 35 J and 50 J impact levels satisfied this standard. There were a few specimens that exceeded this guideline, with 4.4°C being the highest temperature rise.

The temperature rise in the damaged specimens was lower than the temperature rise in the undamaged specimens because of the differences in the applied load and the location of the thermocouples. The residual strengths of the damaged laminates were only 50.5% and 45.6% of the undamaged strength for the 35 J and 50 J specimens respectively. This meant that the loads applied to the damaged specimens during fatigue testing were much lower than the loads applied to the undamaged panels, and therefore the strains were lower as well. The thermocouple was applied in the farfield region for the damaged specimens so as not to interfere with the strain measurements recorded by the DIC system. If the thermocouples had been placed nearer to the damage region,

where the strains were higher in most cases, then the temperature rise would most likely have also been higher.

S-N curves were plotted for both sets of damaged specimens and are shown in Figures 4.32 and 4.33. There is a lot of scatter in the data for both of the curves and no significant statistical trend can be calculated. The R^2 value for the 35 J specimens is only 0.34 and the R^2 value for the 50 J specimens is 0.36. It is clear that these S-N curves are not sufficient to make accurate predictions of the fatigue life of damaged specimens.

Figure 4.32 – Stress - Life Curve for 35 J Impacted Specimens

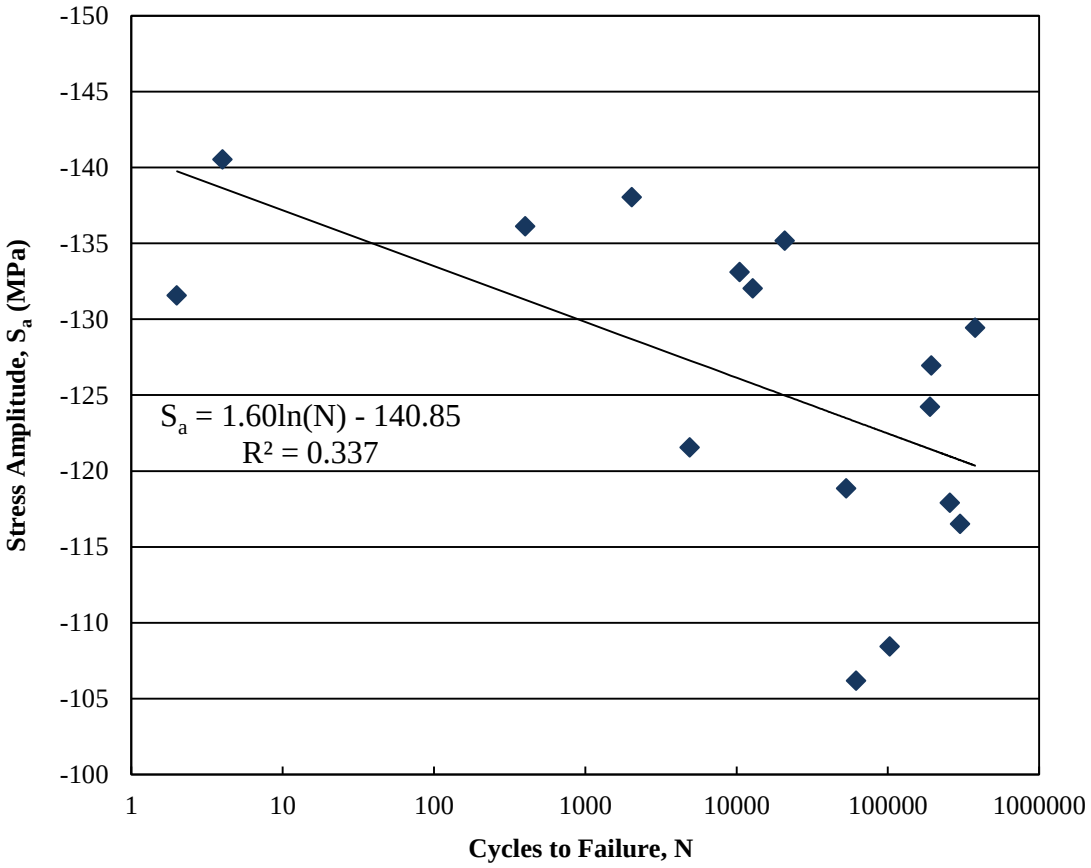

Figure 4.33 – Stress - Life Curve for 50 J Impacted Specimens

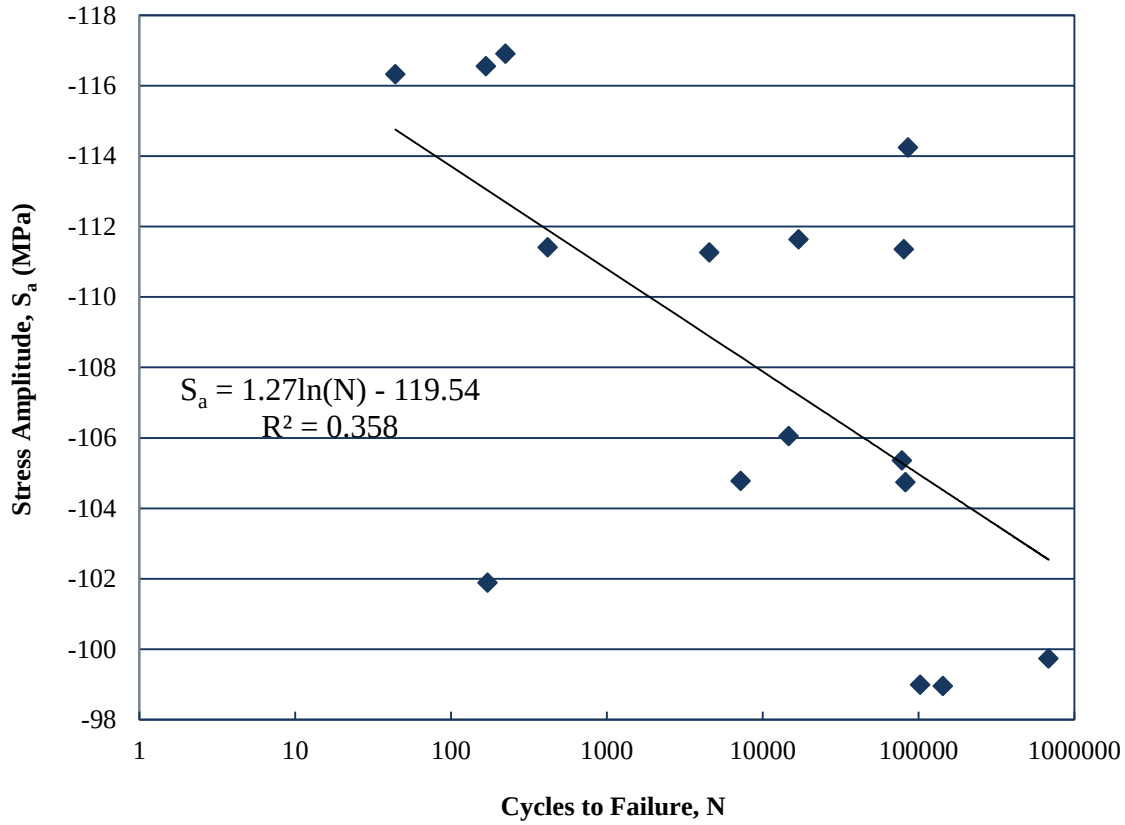

The scatter in the fatigue data of the damaged specimens is most likely related to the large variations in the damage observed by non-destructive evaluation techniques. The variation was especially large in the thermography images recorded from the front face of the specimens. The damage length and area measured using this technique included any cracks within the measurement. It is likely that the variation in crack size and orientation is a primary reason for the scatter in the fatigue data. The following sections attempt to find a suitable method to correlate the data and to make fatigue life predictions for the damaged laminates.

4.4.5 Normalizing Fatigue Data Using Residual Strength

As discussed in the literature review Section 2.4, Yuanjian and Isaac [75] found that tension-tension fatigue data of glass/polyester specimens impacted at varying energy levels could be described by a single curve by normalizing the applied stress using residual strength. An attempt was made to normalize the carbon/epoxy compression-compression fatigue data from this project using the residual strength.

Figure 4.34 shows the combined fatigue results for the undamaged specimens and both impact energy levels that were previously shown individually in Figures 4.31, 4.32, and 4.33. The slopes of the curves that describe the damaged specimens are very small compared to the undamaged slope due to the large degree of scatter in the damaged fatigue data. As well, it can clearly be observed that the fatigue strength of the damaged specimens is well below that of the undamaged specimens, with the fatigue strength of the 50 J specimens lower than the fatigue strength of the 35 J specimens.

Figure 4.34 – Unmodified S-N Curves

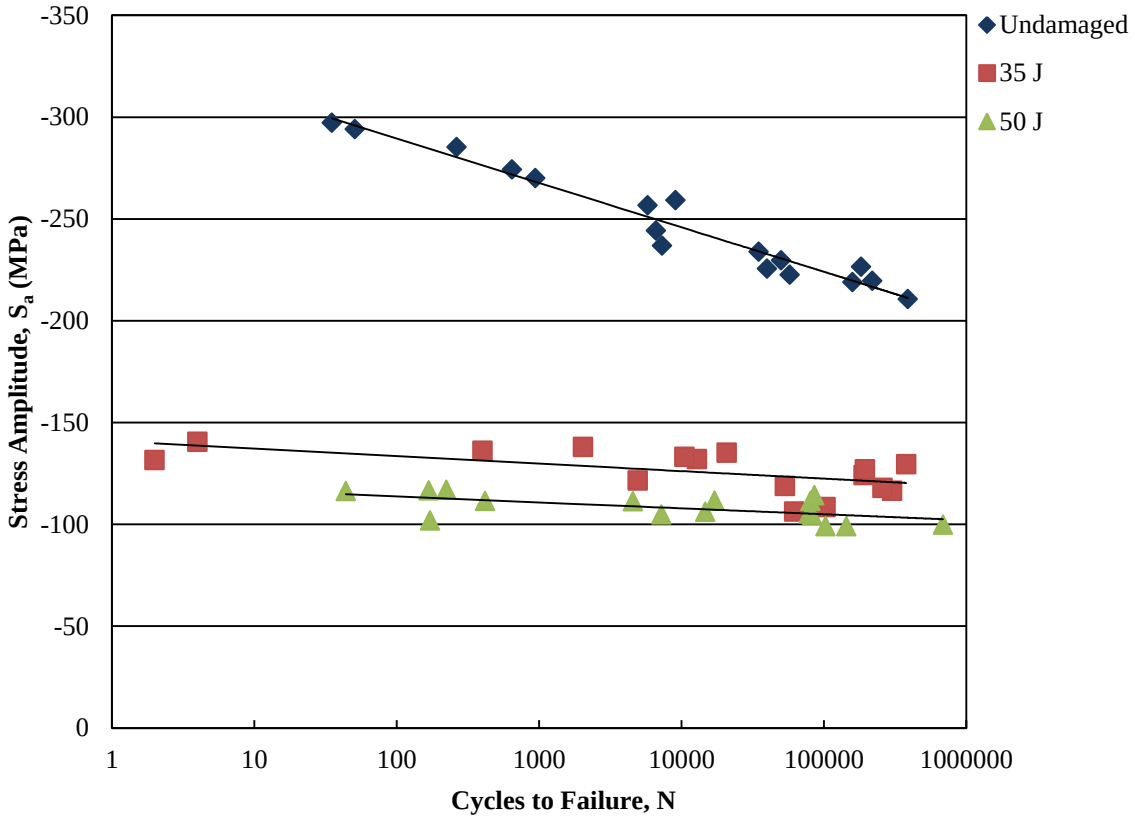

Figure 4.35 shows the S-N plot after the data has been normalized by residual strength. The damaged data now overlaps the undamaged results and a general trend that shows longer fatigue lives at lower stress values can be observed. However, at longer fatigue lifetimes the damaged data has a larger normalized stress than the undamaged data and at short fatigue lifetimes the damage data has a smaller normalized stress than the undamaged data. This is due to the small slope of the damaged data that was discussed above. The R^2 value of the data is still fairly low at 0.46 because the scatter in the damaged fatigue data has not been reduced by normalizing the data with residual strength. The normalization process simply shifts the curves upwards. If the scatter in the damaged fatigue data is smaller, then normalizing the values with residual strength could prove to be a useful method for predicting post-impact fatigue life.

Figure 4.35 – Normalized S-N Curve

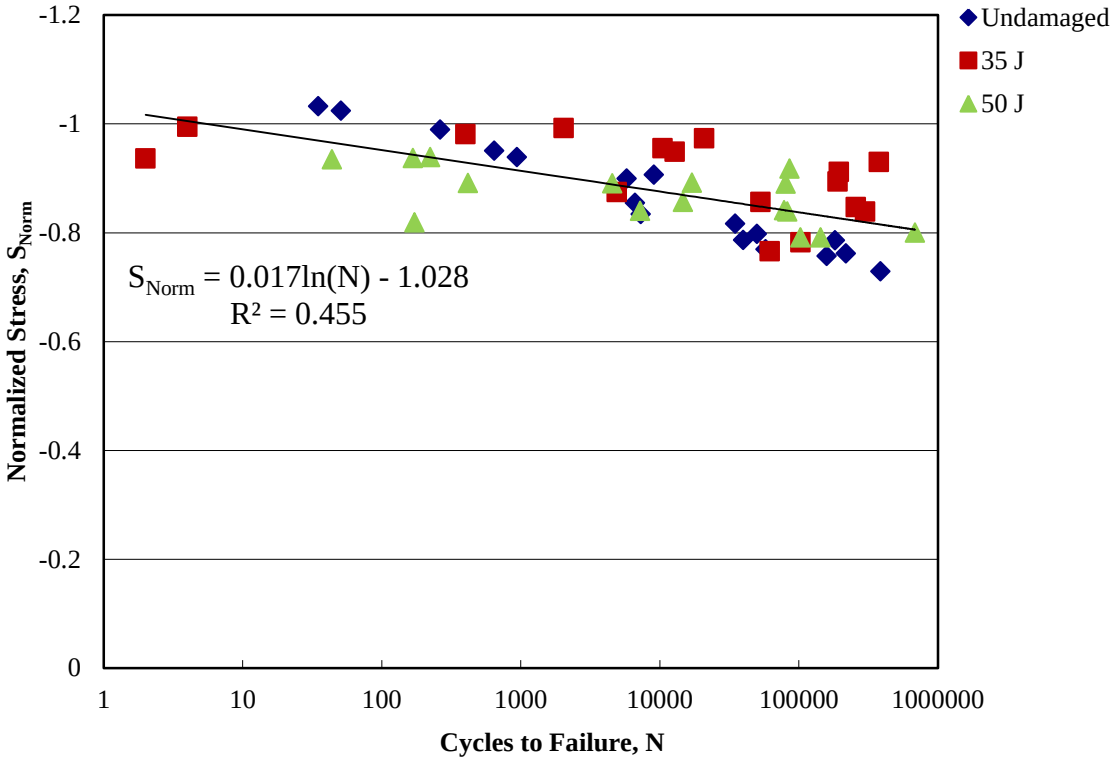

4.4.6 Kang and Kim Fatigue Life Estimation Model

Kang and Kim [76] found that the tension-tension fatigue life of impact damaged carbon/epoxy materials could be modelled using the residual strength and fatigue life of unimpacted laminates. Their paper is first discussed in Section 2.4. An attempt was made to apply their model to the experimental results of this study.

They state that the fatigue life of an impacted laminate can be calculated using the following equation,

$$N_{imp} = N_f \left[1 - \frac{\sigma_0 - \sigma_R}{\sigma_o - \sigma_{max}} \right], \qquad (4.7)$$

where N_{imp} is the fatigue life of the impacted specimen, N_f is the fatigue life of the undamaged specimen under the same loading conditions, σ_o is the strength of the unimpacted laminate, σ_R is the residual strength of the impacted laminate, and σ_{max} is the maximum applied stress level.

Kang and Kim suggest using Caprino's method [19] to predict the residual strength of the impacted specimen. To simplify the analysis, the experimental residual strength will be used directly for this study. They also suggest using Hwang and Han's method [50] to predict the fatigue life of the undamaged laminate. Hwang and Han use a form of power law to describe the undamaged fatigue life. However, the data from this project is best described using a straight-line logarithmic equation as shown in Figure 4.36 that plots the maximum applied stress and cycles to failure for the undamaged fatigue data. From this graph the equation for the undamaged fatigue life (N_f) is given by the logarithmic equation,

$$\sigma_{max} = 21.26 \ln(N_f) \; - \; 744.37 \; . \tag{4.8}$$

When the maximum applied stresses used in the fatigue tests of the damaged specimens are entered into Eqn (4.8), extremely large undamaged fatigue lives are calculated. For example, the largest maximum stress applied to the 35 J damaged specimens was -312 MPa. This results in a calculated undamaged fatigue life of 681 million cycles. When this result is entered into Kang and Kim's equation a remaining fatigue life of over 4.5e6 cycles is calculated. In reality, this specimen broke after only 4 cycles.

Figure 4.36 – Max Stress vs. Cycles to Failure of Undamaged Specimens

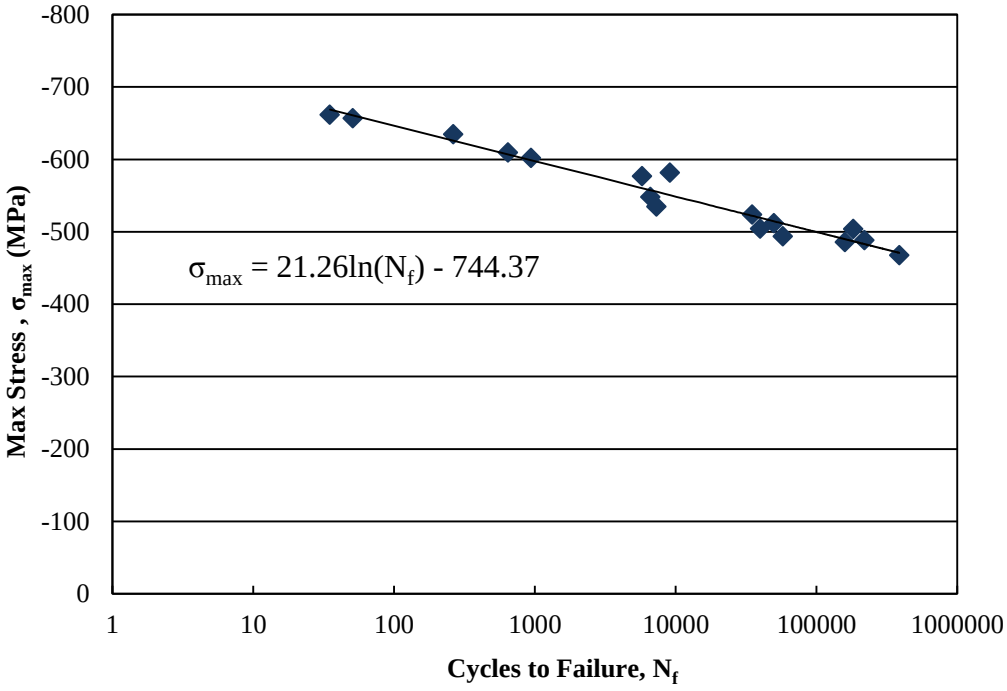

In this study the chosen impact energy levels reduced the residual strength to only 50.5% and 45.6% of the undamaged strength. It appears that Kang and Kim's equation may not be appropriate for impact levels that have significantly reduced the residual strength of the impacted specimens. If impact energy levels smaller than 35 J had been tested the results may have agreed better with Kang and Kim's model.

4.4.7 Strain Concentration Factor (SCFε)

The DIC system was programmed to record the full-field strain at the peak applied load at a set time interval for each of the fatigue tests. A typical view of the axial strain field is shown in Figure 4.37. It can be immediately observed that a strain concentration appears at the location of the damage. Areas of strain relief can be observed above and below the damage region.

Figure 4.37 – Typical Strain Field at Peak Load During Fatigue Testing

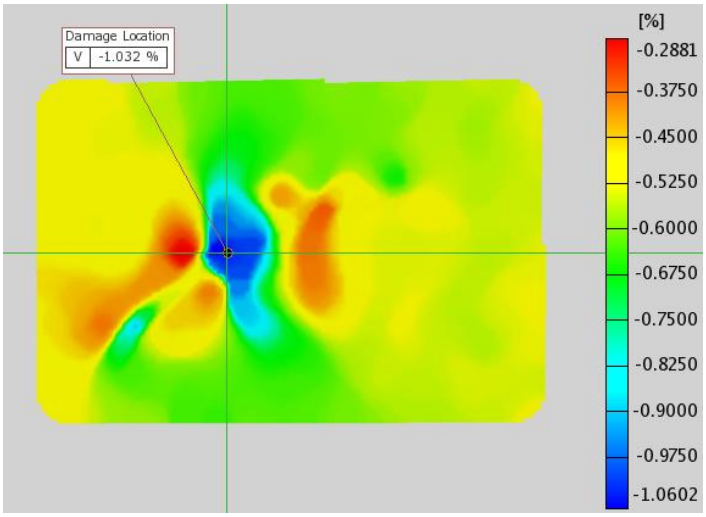

The SCFε was calculated using Eqn (4.6) when the maximum cyclic load was applied at 50 cycles. The SCFε was calculated at 50 cycles because it was observed that the strain values stabilized by this point in the tests. The only exceptions were the three specimens that broke before 50 cycles. The farfield strain measured by the DIC system was replaced by the farfield strain measured by the strain gauges to determine if there was a difference in the results. The results for the 35 J and 50 J specimens are provided in Tables 4.19 and 4.20.

Table 4.19 – Strain Concentration Factors for 35 J Specimens

Specimen	Strain at Damage (DIC)	Average Farfield Strain (Gauges)	SCFε (Gauges)	Average Farfield Strain (DIC)	SCFε (DIC)
2-1	-8498	-4868	1.75	-4922	1.73
2-8	-8244	-4927	1.67	-5266	1.57
2-2	-7613	-5419	1.40	-4993	1.52
2-20	-8515	-5398	1.58	-4975	1.71
2-4	-9972	-5624	1.77	-5179	1.93
2-9	-7258	-5803	1.25	-5148	1.41
2-17	-7506	-5884	1.28	-5192	1.45
2-19	-7941	-5306	1.50	-5061	1.57
2-12	-7766	-5930	1.31	-5396	1.44
2-11	-7093	-6189	1.15	-4929	1.44
2-25	-7710	-6181	1.25	-5508	1.40
2-23	-9872	-6248	1.58	-5748	1.72
1-21	-9043	-6103	1.48	-5301	1.71
2-16	-9276	-6374	1.46	-5843	1.59
1-34	-14323	-6191	2.31	-6296	2.28
1-32	-14513	-5892	2.46	-6119	2.37

Table 4.20 – Strain Concentration Factors for 50 J Specimens

Specimen	Strain at Damage (DIC)	Average Farfield Strain (Gauges)	SCFε (Gauges)	Average Farfield Strain (DIC)	SCFε (DIC)
2-32	-9424	-5020	1.88	-4974	1.89
1-20	-8571	-4500	1.90	-4859	1.76
1-19	-8587	-4981	1.72	-4533	1.89
1-8	-8230	-4689	1.76	-4646	1.77
2-29	-12623	-5389	2.34	-5213	2.42
1-2	-10602	-5090	2.08	-5272	2.01
1-4	-11555	-5335	2.17	-5741	2.01
1-44	-10136	-4823	2.10	-5577	1.82
2-30	-14190	-5407	2.62	-5307	2.67
1-22	-6024	-5018	1.20	-4283	1.41
2-28	-7238	-4449	1.63	-4533	1.60
1-17	-6815	-4677	1.46	-3790	1.80
2-38	-12314	-4700	2.62	-5128	2.40
2-37	-7341	-5098	1.44	-4422	1.66
2-33	-5691	-4505	1.26	-3999	1.42
1-16	-10338	-4888	2.12	-5172	2.00

On average, the SCFε calculated using the DIC farfield data was higher when compared to those calculated using the strain gauges for the 35 J specimens, but only a minimal increase was observed for the 50 J specimens. The high degree of scatter in the S-N fatigue data can most likely be attributed to the high degree of variability in the SCFε data, which in turn can be related to the large variation in the internal damage of each specimen observed by ultrasonic C-scan and thermography.

4.4.8 Modified Damaged S-N Curves

It is difficult to calculate the stress concentration factor from the lamina properties and strain at the damage region because the modulus of elasticity in the damage area changes as the damage progresses. Therefore, it is assumed in this case that the strain concentration factor is equal to the stress concentration factor, ie. SCFε = SCFσ. A local stress amplitude at the point of highest strain in the damage region, $S_{a,local}$, is calculated for each specimen by multiplying the SCFσ by the applied axial stress amplitude, S_a, as given in Eqn (4.9):

$$S_{a,local} = SCF_{\sigma} \times S_a \,. \tag{4.9}$$

In doing so, it was assumed that the material is undamaged. The results are summarized in Tables 4.21 and 4.22.

Table 4.21 – Local Stress Amplitude for 35 J Specimens

Specimen	Stress Amplitude S_a (MPa)	Stress Concentration Factor [Gauges]	Local Stress Amplitude [Gauges] (MPa)	Stress Concentration Factor [DIC]	Local Stress Amplitude [DIC] (MPa)
2-1	-106.2	1.75	-185.3	1.73	-183.3
2-8	-108.4	1.67	-181.4	1.57	-169.7
2-2	-116.5	1.40	-163.7	1.52	-177.7
2-20	-118.8	1.58	-187.5	1.71	-203.4
2-4	-121.6	1.77	-215.5	1.93	-234.0
2-9	-124.2	1.25	-155.4	1.41	-175.1
2-17	-126.9	1.28	-162.0	1.45	-183.5
2-19	-117.9	1.50	-176.4	1.57	-185.0
2-12	-129.4	1.31	-169.5	1.44	-186.3
2-11	-132.0	1.15	-151.3	1.44	-190.0
2-25	-135.2	1.25	-168.6	1.40	-189.2
2-23	-136.1	1.58	-215.1	1.72	-233.8
1-21	-133.1	1.48	-197.2	1.71	-227.1
2-16	-138.0	1.46	-200.9	1.59	-219.1
1-34	-140.5	2.31	-325.1	2.28	-319.7
1-32	-131.5	2.46	-324.1	2.37	-312.0

Table 4.22 – Local Stress Amplitude for 50 J Specimens

Specimen	Stress Amplitude S_a (MPa)	Stress Concentration Factor [Gauges]	Local Stress Amplitude [Gauges] (MPa)	Stress Concentration Factor [DIC]	Local Stress Amplitude [DIC] (MPa)
2-32	-111.6	1.88	-209.6	1.89	-211.5
1-20	-99.0	1.90	-188.5	1.76	-174.6
1-19	-111.3	1.72	-191.8	1.89	-210.8
1-8	-105.4	1.76	-184.9	1.77	-186.6
2-29	-116.9	2.34	-273.8	2.42	-283.1
1-2	-111.4	2.08	-232.1	2.01	-224.1
1-4	-116.6	2.17	-252.5	2.01	-234.6
1-44	-104.8	2.10	-220.2	1.82	-190.4
2-30	-116.3	2.62	-305.3	2.67	-311.0
1-22	-111.4	1.20	-133.7	1.41	-156.6
2-28	-99.0	1.63	-161.0	1.60	-158.0
1-17	-104.7	1.46	-152.6	1.80	-188.4
2-38	-101.9	2.62	-266.9	2.40	-244.7
2-37	-114.2	1.44	-164.5	1.66	-189.7
2-33	-99.7	1.26	-126.0	1.42	-141.9
1-16	-106.0	2.12	-224.3	2.00	-212.0

The S-N curves in Figures 4.32 and 4.33 were re-plotted using the local stress amplitude as defined in Eqn (4.9) for each specimen, and are shown in Figures 4.38 and 4.39. Similar to Horn et al. in Ref. [81], the correlation between the S-N data improves dramatically at both impact energy levels. For the 35 J specimens the R^2 value for the strain gauge concentration factors was equal to 0.87. This value improved to 0.92 for the DIC concentration factors. In contrast, the R^2 value was 0.87 for the strain gauge concentration factors for the 50 J specimens, but decreased to 0.84 for the DIC concentration factors. It can also be observed that there is a significant increase in the slopes of these two graphs when compared to the original S-N curves.

Figure 4.38 – Local Stress - Life Curve for 35 J Impacted Specimens

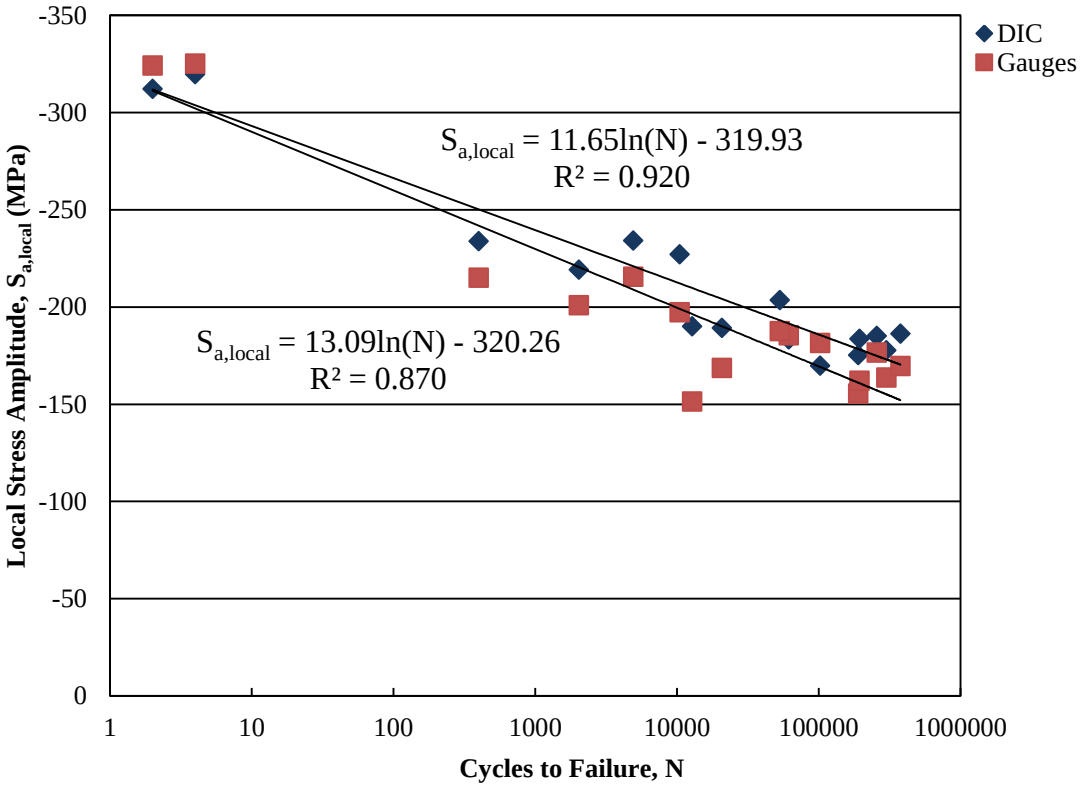

Figure 4.39 – Local Stress - Life Curve for 50 J Impacted Specimens

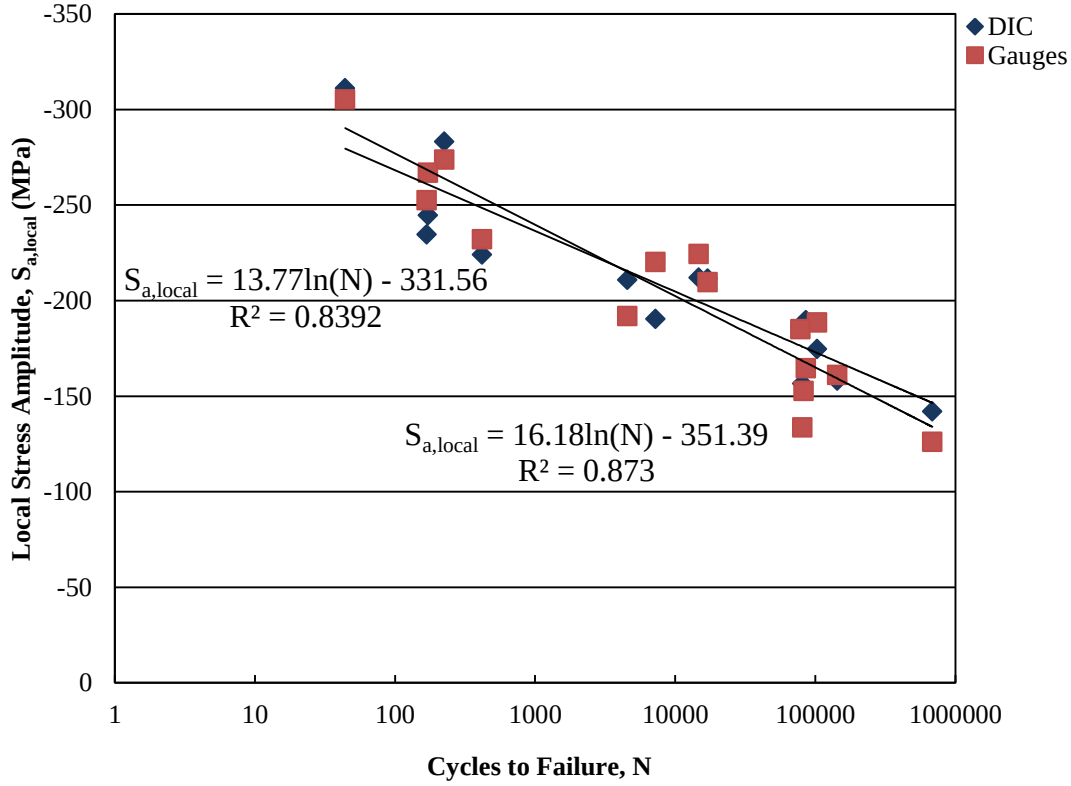

Figure 4.40 plots the S-N curves for the 35 J, 50 J, and undamaged specimens on the same chart. The stress concentrations calculated using the DIC farfield results were chosen for the 35 J and 50 J data in this chart because the results more accurately matched the undamaged results. The undamaged trend line has the smallest slope at 9.47, the 35 J line has a slope of 11.65, and the 50 J line has the steepest slope of 13.77. The intercept of the undamaged and 50 J specimens are very close at 333.1 and 331.6 respectively. The intercept for the 35 J data is slightly lower at 319.9.

Figure 4.40 – Local Stress - Life Curves

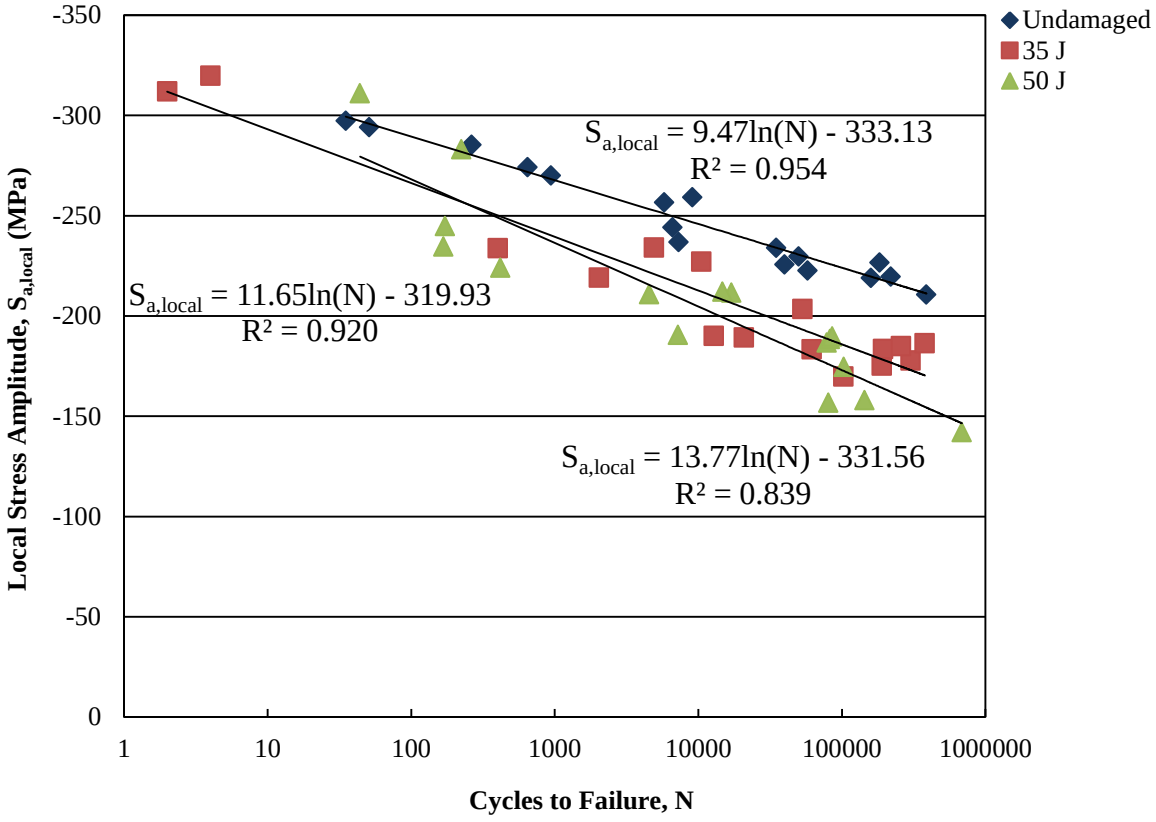

In order to make post-impact fatigue life predictions from the experimental data, the local stress amplitude of the undamaged curve needed to be altered by a damage factor to account for the initial impact damage. Regardless of the initial impact damage, the local stress amplitude at 1 cycle should be the same for all specimens. Therefore, the

local stress amplitude at 1 cycle was left unaltered. A damage factor was calculated for each impact energy level and the undamaged point at 10^6 cycles was then decreased by the corresponding factor. Three different damage factors were applied to determine which best fit the data.

The first damage factor applied was equal to the reduction in residual strength. The 35 J specimens had a residual strength of 50.5% of the undamaged strength, or in other words, a reduction of strength by a factor of 1.98. The 50 J specimens had a residual strength of 45.6% of the undamaged strength, or a reduction in strength by a factor of 2.19. The results are plotted in Figures 4.41 and 4.42 for the 35 J and 50 J specimens respectively. In both cases the prediction curve is conservative when compared to the experimental data.

Figure 4.41 – Residual Strength S-N Prediction Curve for 35 J Specimens

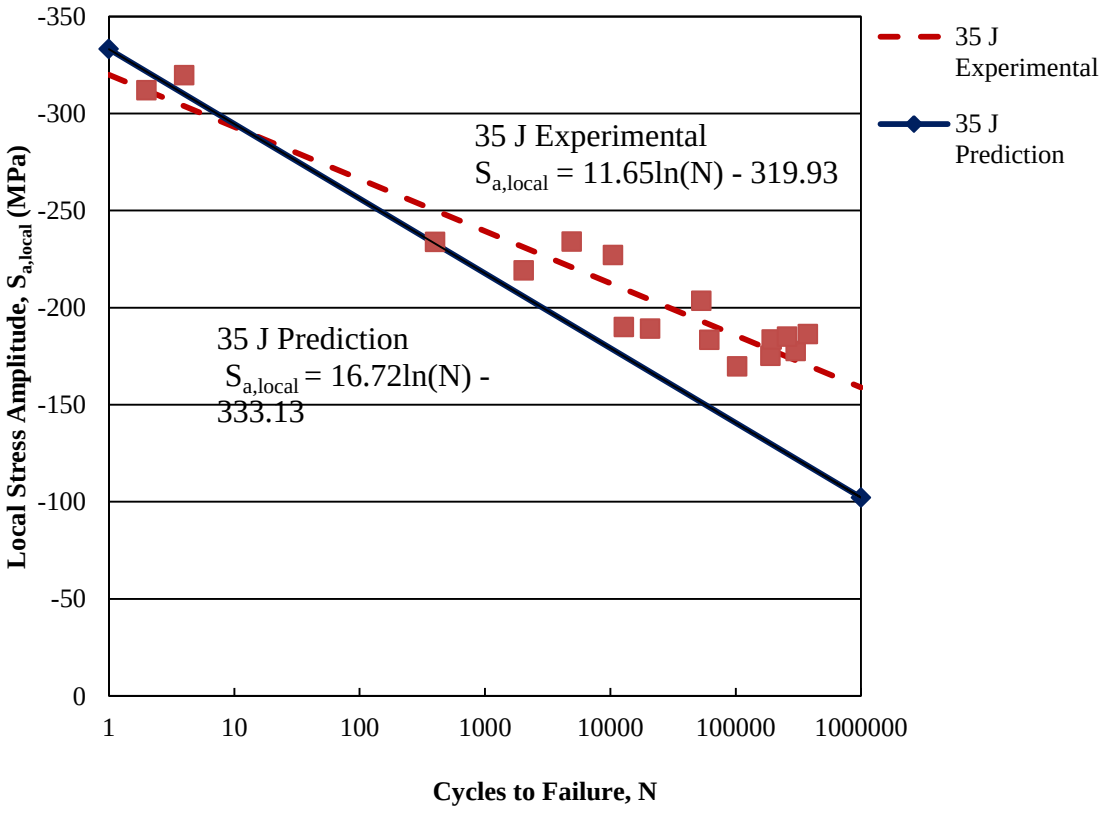

Figure 4.42 – Residual Strength S-N Prediction Curve for 50 J Specimens

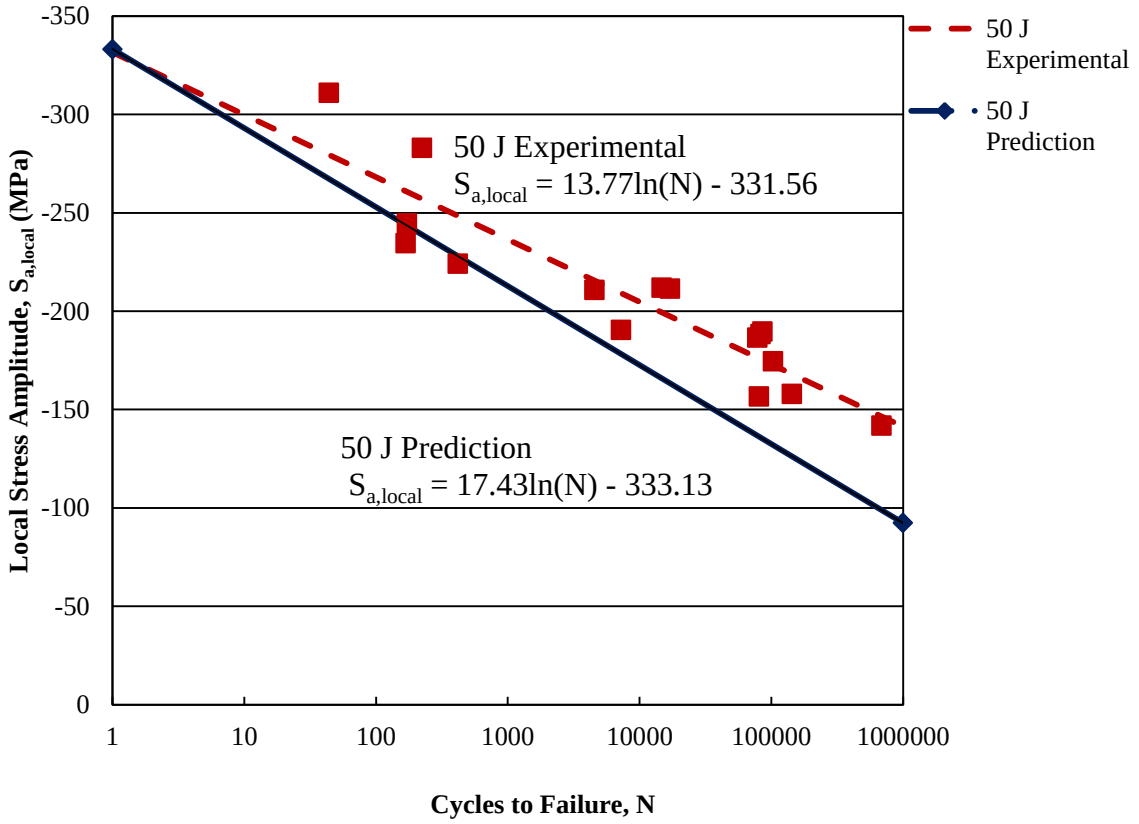

The second damage factor applied to the data was equal to the ratio of the undamaged cross-sectional area over the damaged cross-sectional area. The damaged cross-sectional area was calculated by subtracting the width of the damage as measured by ultrasonic C-scan from the total width of the specimen, and then multiplying by the specimen thickness. This resulted in a factor of 1.48 for the 35 J specimens and 1.72 for the 50 J specimens. The results for the 35 J and 50 J specimens are plotted in Figures 4.43 and 4.44 respectively. The predictions are once again conservative for both cases, although degree of conservation is diminished.

Figure 4.43 – Reduced Cross-Section S-N Prediction Curve for 35 J Specimens

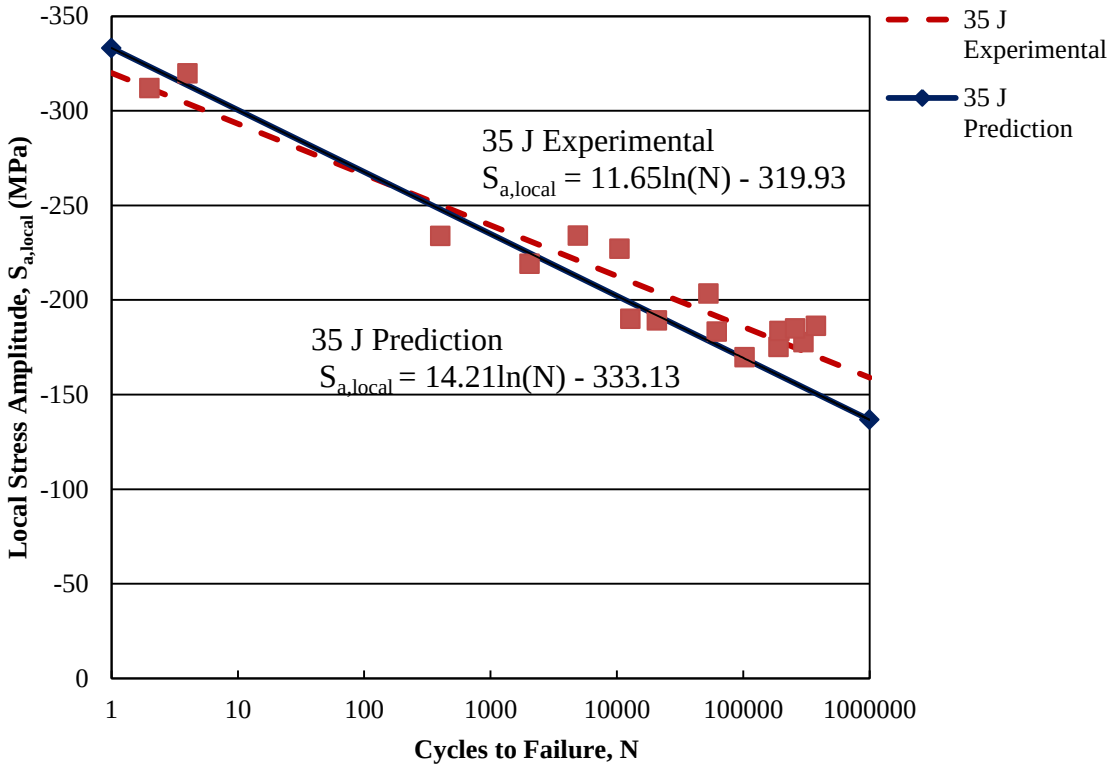

Figure 4.44 – Reduced Cross-Section S-N Prediction Curve for 50 J Specimens

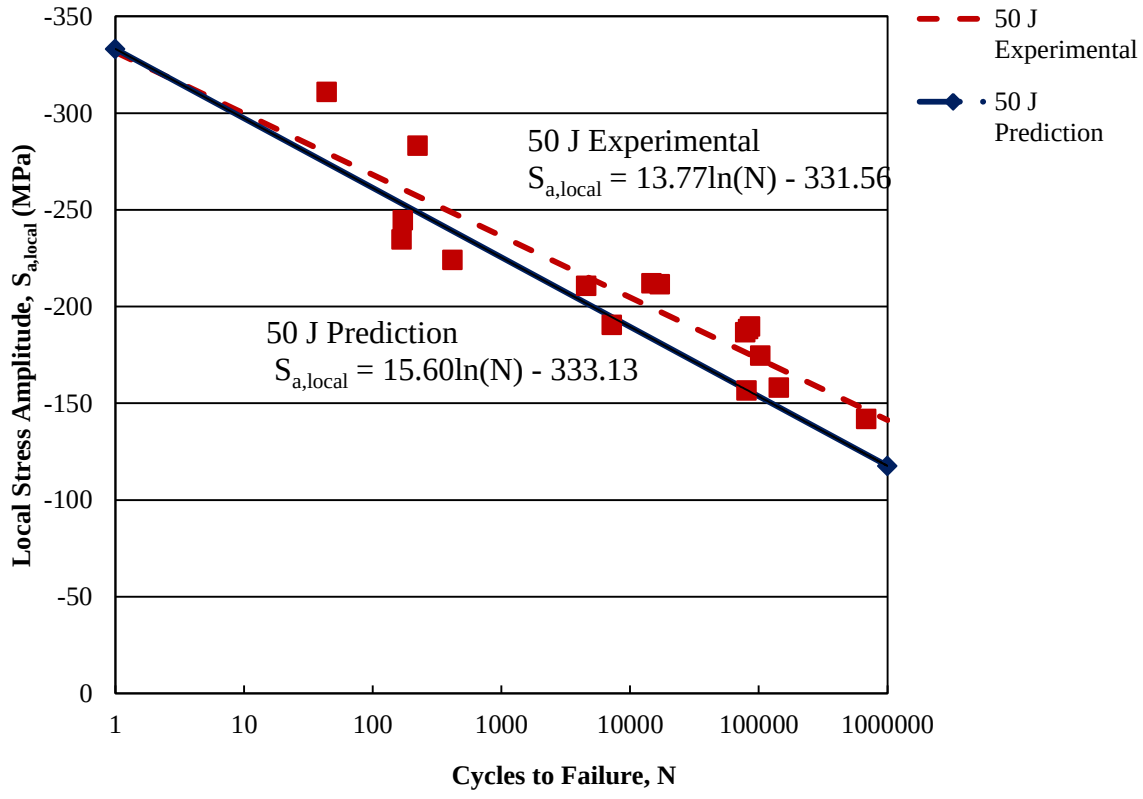

The final damage factors were the $SCF\varepsilon_{linear}$ values calculated from the static testing in Section 4.3.2.3. A value of 1.28 was calculated for the 35 J specimens and 1.41 for the 50 J specimens. The undamaged point at 10^6 cycles was decreased by the $SCF\varepsilon_{linear}$ for the corresponding impact energy level according to Eqn (4.10):

$$S_{a,local} = \frac{9.47 \ln\left(10^6\right) - 333.13}{SCF\varepsilon_{linear}} . \tag{4.10}$$

The results are plotted in Figures 4.45 and 4.46 for the 35 J and 50 J specimens respectively.

Figure 4.45 – $SCF\varepsilon_{linear}$ S-N Prediction Curve for 35 J Specimens

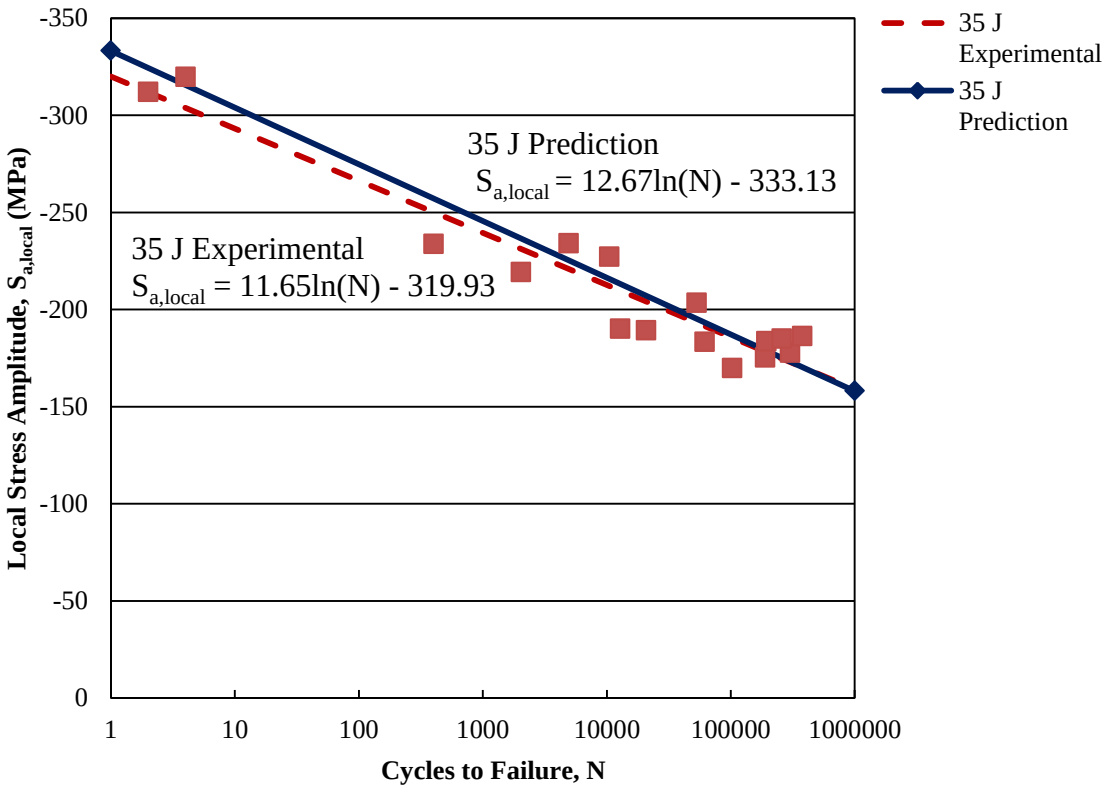

Figure 4.46 – SCFε_{linear} S-N Prediction Curve for 50 J Specimens

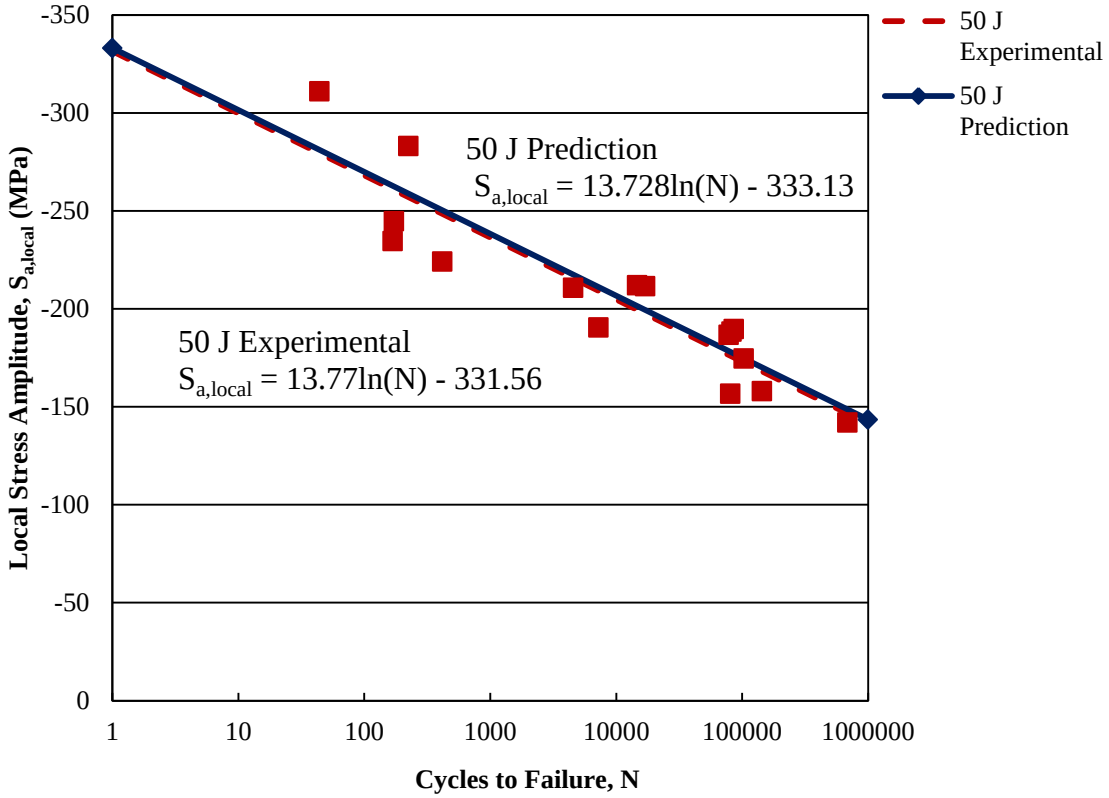

The prediction curves now match very closely with the experimental data. The slope of the 35 J experimental data is 11.65 compared to 12.67 for the prediction curve. The slopes of the 50 J experimental data and the prediction curve are almost identical with values of 13.77 and 13.73 respectively. The largest difference between the experimental data and the prediction curves is the y-intercept value of the 35 J data. The trend of the experimental data predicts fatigue failure at a stress amplitude of -319.93 MPa compared to -333.13 MPa predicted by the adjusted undamaged curve. That is, the largest percent difference is only 4%.

These findings are significant for the fact that a methodology has been developed for predicting the post-impact fatigue life of this material and lay-up. First, a damage factor is calculated using the reduction in residual strength, ratio of undamaged to

damaged cross-sectional area, or the $SCF\varepsilon_{linear}$, depending on the degree of conservation required. The residual strength is determined by conducting static tests on specimens damaged at various impact energy levels. The ratio of undamaged to damaged cross-sectional area, and the $SCF\varepsilon_{linear,}$ can be measured non-destructively using ultrasonic C-scan. The ratio of undamaged to damaged cross-sectional area is simply calculated using the damage width, while the $SCF\varepsilon_{linear}$ is predicted using the linear relationship between damage area, impact energy, and the $SCF\varepsilon_{linear}$. Once the damage factor has been determined the S-N curve of the undamaged specimens is altered using the damage factor as described above. The fatigue life of the damaged specimen can now be predicted based on this curve.

5 CONCLUSION

This chapter provides a summary of the testing that was performed during the course of this project. The results, findings, and conclusions drawn from these tests will then be discussed. Finally, recommendations for further testing and analysis will be outlined.

5.1 Summary of Testing

This project examined the post-impact static and fatigue behaviour of carbon/epoxy laminates. Longitudinal compression, transverse compression, and shear tests were performed in order to determine the lamina mechanical properties. 24-ply, quasi-isotropic laminates were then constructed with a lay-up of $[45/90/-45/0]_{3S}$. These laminates were impacted by a drop-weight impact tester at energy levels of 35 J and 50 J in order to create barely visible impact damage that was representative of a large hail strike. The surface damage was examined visually, and then the internal damage was characterized using ultrasonic C-scan and thermographic non-destructive evaluation methods.

Static compression tests were performed on undamaged and damaged specimens to gain a better understanding of the effects of the impact on the residual strength and modulus of the specimens. Finally, compression-compression fatigue tests of both the undamaged and damaged specimens were conducted. A digital image correlation system was used to measure the strain field of the damaged specimens during testing.

5.2 Summary of Results and Findings

The mechanical properties of the lamina obtained through testing were fairly typical for a carbon/epoxy pre-preg material. The longitudinal modulus of 130.2 GPa was within the normal range for this type of material. The transverse modulus was a little lower then average with a value of 8.4 GPa, while the shear modulus was a little higher than average with a value of 7.4 GPa.

The 35 J and 50 J impact energy levels created barely visible impact damage in the specimens. Although some surface cracking did appear, the indentation size would be very difficult to observe during a visual inspection. The ultrasonic C-scan and thermography data revealed that the internal damage was much greater in size and severity than the visible damage. The inspection methods showed that the 50 J impact produced a larger damage area than the 35 J impact. From the limited amount of points, the ultrasonic C-scan data indicated that the average damage area increased linearly with impact energy.

The coefficient of variation of the damage size measured by thermography from the front face was much larger than coefficient measured from the back side. Cracks were much more common on the front face and added to the variability in the damage data due to the high variability in the crack size and orientation. However, the damage size increased from the front to the back face even though the variation in the data decreased. This indicates that the size of the damage increases through the thickness of the specimen.

The stress-strain curves from the static compression testing of the undamaged specimens remained linear for about the first half of the test and then became slightly non-linear. This behaviour indicates that this is a brittle material that may break with little or no warning. The static results from the damaged specimens showed that the global compressive elastic modulus marginally increased after impact. In contrast, the residual strength was only 50.5% and 45.6% of the undamaged strength for the 35 J and 50 J specimens respectively. The reduction in strength was not linear with impact energy, but the exact relationship was difficult to determine without having more data points at lower energy levels. This is a very dramatic drop-off in strength considering the small size of the visible damage and emphasizes the importance of non-destructive evaluation methods that can detect this type of damage. It also demonstrates the importance of carefully considered design safety factors that take into account the strength reduction caused by barely visible damage.

The local and farfield strains measured by digital image correlation were used to calculate a strain concentration factor for each static test. The SCFε remained linear at low loads and then increased dramatically immediately before failure. It was found that the average SCFε_{linear} increased linearly with impact energy.

Three trends in the strain fields were observed by DIC during the compression-compression fatigue tests. In one trend the strain remained constant until failure. In another trend the strain increased throughout the test, and in the final trend the strain remained constant for most of the test and then increased rapidly near failure. It was found that the constant strain trend generally occurred in the specimens with lower

SCFε's. The non-linear increase in strain at the end of life that was observed in the other two trends was due to the propagation of damage and fibre breakage.

The size and rate of change of the out-of-plane deformation of the damage region during fatigue testing was examined, but no correlation could be found with the SCFε or stress amplitude. It was concluded that the out-of-plane deformation was not a reliable parameter for post-impact fatigue prediction.

A stress-life curve was created from the compression-compression fatigue results of the undamaged specimens. The data was successfully described using a logarithmic curve. The fatigue limit for one million cycles was predicted to be 72% of the static strength of the laminate. S-N curves were then created for the 35 J and 50 J impacted specimens. There was an extremely large amount of scatter in the data. It was concluded that these curves were insufficient to make predications of the post-impact fatigue life and that the scatter was related to the variation in the initial damage that was observed using ultrasonic C-scan and thermography.

The original S-N curves of the damaged specimens were normalized by residual compressive strength. The normalized damage fatigue data fell within the range of the undamaged specimens and showed a general trend of increasing fatigue life as stress amplitude was decreased, but the scatter was still very high. It was concluded that normalizing by residual strength may be a useful method of post-impact fatigue prediction in cases where the scatter in the damaged data is smaller. This reduced scatter may be observed in specimens that have smaller cracks due to lower impact energy levels, or in specimens that are constructed with different materials and lay-up sequences.

The post-impact fatigue estimation model presented in Ref. [76] was also examined. For this case the model did not appear to be appropriate, although it may be appropriate for impact energy levels that have a smaller effect on the residual strength of the specimens.

It was assumed that the SCFε measured by DIC during the fatigue tests was equal to the SCFσ. The local stress amplitude in the damage region was then calculated using the SCFσ. The local stress amplitude was plotted against cycles to failure and it was found that the scatter was reduced in the damaged fatigue data and correlations could be found. Damage factors were then calculated using the reduction in residual strength, the ratio of undamaged to damaged cross-sectional area, and the $SCF\varepsilon_{linear}$. One of the damage factors was then chosen depending on the degree of conservation required in the post-impact fatigue life prediction. The reduction in residual strength was the most conservative, while the $SCF\varepsilon_{linear}$ was the least conservative. The local stress amplitude at 10^6 cycles of the undamaged fatigue trend was then divided by the chosen damage factor at each impact energy level. The adjusted undamaged S-N curves could then be used for post-impact fatigue life predictions.

5.3 Final Conclusions

A methodology has been developed to predict the post-impact fatigue life for this composite material and lay-up. First, a damage factor is calculated using the results of static residual strength testing, the ratio of undamaged to damaged cross-sectional area, or the $SCF\varepsilon_{linear}$. The ratio of undamaged to damaged cross-sectional area is calculated using damage width measurements from ultrasonic C-scans, while the strain

concentration factor can be calculated due to the linear relationship between damage area, impact energy, and strain concentration factor. One of the damage factors is then chosen depending on the degree of conservation required in the post-impact fatigue life prediction. Next, the local stress amplitude at 10^6 cycles of the undamaged S-N curve is divided by the chosen damage factor. The adjusted undamaged S-N curve is then used to predict the fatigue life of the damaged specimen.

5.4 Future Work

The findings from this project present multiple avenues for further investigation. Static and fatigue testing should be performed on specimens that have been impacted at lower energy levels. The data could be used to determine the threshold impact energy level and would confirm the linear relationships between damage area, $SCF\varepsilon_{linear}$, and impact energy. It would also provide more data to determine if there is a relationship between the residual static strength, impact energy, and damage area. If a relationship is discovered this would provide a method of determining the residual strength using non-destructive evaluation techniques.

Additional fatigue tests at lower energy levels would provide valuable data to determine whether less cracking in the specimens would lead to less scatter in the fatigue results, and therefore allow for post-impact fatigue predictions by normalizing the results with respect to residual strength. It would also provide insight into whether the post-impact fatigue model presented in Ref. [76] is appropriate for lower impact energy levels that have a smaller effect on the residual strength of the specimens.

Further fatigue tests are also required to confirm that the methodology developed in this study is applicable at lower impact energy levels. The method has also only been shown to work for compression-compression fatigue at a load ratio of R = 10. More tests need to be completed at other load ratio values to determine the effect of varying mean stresses. Finally, additional testing is required to determine the suitability of the method for other materials and lay-ups.

6 REFERENCES

[1] M. Buggy and J. McNamara, "Structural integrity after impact of composite laminates," *Frontiers for Engineering Materials – Key Engineering Materials*, vol.118, pp.51-57, 1996.

[2] N.H. Tai, M.C. Yip and J.L. Lin, "Effects of low-energy impact on the fatigue behavior of carbon/epoxy composites," *Composites Science and Technology*, vol.58 (1), pp.1-8, 1998.

[3] Y.P. Siow and V.P.W. Shim, "Experimental study of low velocity impact damage in woven fiber composites," *Journal of Composite Materials*, vol.32 (12), pp.1178-1202, 1998.

[4] D.G. Moon and J.M. Kennedy, "Post-impact fatigue response of stitched composites," *Composite Materials: Fatigue and Fracture, ASTM STP 1230*, vol.5, pp.351-367, 1995.

[5] W.J. Cantwell, P.T. Curtis and J. Morton, "Impact and subsequent fatigue damage growth in carbon fibre laminates," *International Journal of Fatigue*, vol.6 (2), pp.113-118, 1984.

[6] A.M. Amaro, J.B. Santos and J.S. Cirne, "Comparative study of different non-destructive testing techniques in the characterisation and quantification of the damage effects in carbon-epoxy laminates," *Insight-Non-Destructive Testing and Condition Monitoring*, vol.46 (9), pp.559-565, 2004.

[7] M. Genest, M. Martinez, N. Mrad, G. Renaud and A. Fahr, "Pulsed thermography for non-destructive evaluation and damage growth monitoring of bonded repairs," *Composite Structures*, vol.88 (1), pp.112-120, 2009.

[8] S.S. Russell, M.A. Sutton and H.S. Chen, "Image correlation quantitative non-destructive evaluation of impact and fabrication damage in a glass fiber-reinforced composite system," *Materials Evaluation*, vol.47(5), pp.550-557, 1989.

[9] C. Bisagni and C. Walters, "Experimental investigation of the damage propagation in composite specimens under biaxial loading," *Composite Structures*, vol.85 (4), pp.293-310, 2008.

[10] G. Stelzer, A. Klavzar, M.Bos and R. Renz, “Investigation of the thermoelastic response of long-fibre reinforced thermoplastics by comparison with different non-contact strain measurement techniques,” *International Journal of Materials Research*, vol.97(12), pp.1706-1715, 2006.

[11] D. Delfosse and A. Poursartip, “Energy-based approach to impact damage in CFRP laminates,” *Composites - Part A: Applied Science and Manufacturing*, vol.28 (7), pp.647-655, 1997.

[12] H. Kim and K.T. Kedward, “Modeling hail ice impacts and predicting impact damage initiation in composite structures,” *AIAA Journal*, vol.38 (7), pp.1278-1288, 2000.

[13] K.V. Williams, R. Vaziri and A. Poursartip, “A physically based continuum damage mechanics model for thin laminated composite structures,” *International Journal of Solids and Structures*, vol.40 (9), pp.2267-2300, 2003.

[14] H. Saito and I. Kimpara, “Evaluation of impact damage mechanism of multi-axial stitched CFRP laminate,” *Composites Part A (Applied Science and Manufacturing)*, vol.37 (12), pp.2226-2235, 2006.

[15] E.F. Dost, L.B. Ilcewicz, W.B. Avery and B.R. Coxon, “Effects of stacking sequence on impact damage resistance and residual strength for quasi-isotropic laminates,” *ASTM STP 1110*, pp.476-500, 1991.

[16] S.A. Hitchen and R.M.J. Kemp, “The effect of stacking sequence on impact damage in a carbon fibre/epoxy composite,” *Composites*, vol.26 (3), pp.207-214, 1995.

[17] G.E. Husman, J.M. Whitney and J.C. Halpin, “Residual strength characterization of laminated composites subjected to impact loading,”*ASTM STP 568*, pp.92-113, 1975.

[18] V. Sarma Avva and H.L. Padmanabha, “Compressive residual strength prediction in fiber-reinforced laminated composites subjected to impact loads,” in *Proceedings of the 6th International Conference on Fracture*, 1984, pp.2897-2907.

[19] G. Caprino, “Residual strength prediction of impacted CFRP laminates,” *Journal of Composite Materials*, vol.18 (6), pp.508-518, 1984.

[20] M.S. Found, I.C. Howard and M. Oxley, “The effect of low-velocity impact damage on the fatigue performance of a woven carbon-fibre-reinforced plastic,” in *Proceedings of the Institution of Mechanical Engineers. Fourth International Conference. FRC '90 Fibre Reinforced Composites*, 1990, pp.245-252.

[21] Y.Q. Ding, Y. Yan and R. McIlhagger, “Effect of impact and fatigue loads on the strength of plain weave carbon-epoxy composites,” *Journal of Materials Processing Technology*, vol.55 (2), pp.58-62, 1995.

[22] M.S. El-Zein and K.L. Reifsnider, “On the prediction of tensile strength after impact of composite laminates,” *Journal of Composites Technology & Research*, vol.12 (3), pp.147-154, 1990.

[23] Y. Xiong, C.Poon, P.V. Straznicky, and H. Vietinghoff, “A prediction method for the compressive strength of impact damaged composite laminates,” *Composite Structures*, vol.30, pp.357-367, 1995.

[24] T. Nyman, A. Bredberg and J. Schon, “Equivalent damage and residual strength for impact damaged composite structures,” *Journal of Reinforced Plastics and Composites*, vol.19 (6), pp.428-448, 2000.

[25] C. Soutis, P.T. Curtis and N.A. Fleck, “Compressive failure of notched carbon fibre composites,” in *Proceedings of the Royal Society of London, Series A (Mathematical and Physical Sciences)*, vol.440 (1909), 1993, pp.241-256.

[26] C. Soutis and P.T. Curtis, “Prediction of the post-impact compressive strength of CFRP laminated composites,” *Composites Science and Technology*, vol.56 (6), pp.677-684, 1996.

[27] V.J. Hawyes, P.T. Curtis and C. Soutis, “Effect of impact damage on the compressive response of composite laminates,” *Composites - Part A: Applied Science and Manufacturing*, vol.32 (9), pp.1263-1270, 2001.

[28] S. Wang, L. Wu and L. Ma, “Low-velocity impact and residual tensile strength analysis to carbon fiber composite laminates,” *Materials and Design*, vol.31 (1), pp.118-125, 2010.

[29] G.C. Papanicolaou and C.D. Stavropoulos, “New approach for residual compressive strength prediction of impacted CFRP laminates,” *Composites*, vol.26 (7), pp.517-523, 1995.

[30] H. Naveb-Hashemi, M.D. Cohen, J. Zotos and R. Poormand, "Ultrasonic characteristics of graphite/epoxy composite material subjected to fatigue and impacts," *Journal of Nondestructive Evaluation*, vol.5 (3-4), pp.119-131, 1986.

[31] A. Varvani-Farahani, H. Haftchenari and M. Panbechi, "A fatigue damage parameter for life assessment of off-axis unidirectional GRP composites," *Journal of Composite Materials*, vol.40 (18), pp.1659-1670, 2006.

[32] M. Kawai and H. Suda, "Effects of non-negative mean stress on the off-axis fatigue behavior of unidirectional carbon/epoxy composites at room temperature," *Journal of Composite Materials*, vol.38 (10), pp.833-854, 2004.

[33] J.A. Epaarachchi and P.D. Clausen, "An empirical model for fatigue behavior prediction of glass fibre-reinforced plastic composites for various stress ratios and test frequencies," *Composites Part A (Applied Science and Manufacturing)*, vol.34A (4), pp.313-326, 2003.

[34] A. Poursartip, M.F. Ashby and P.W.R. Beaumont, "Damage accumulation during fatigue of composites," *Scripta Metallurgica*, vol.16 (5), pp.601-606, 1982.

[35] J.J. Xiong and R.A. Shenoi, "A two-stage theory on fatigue damage and life prediction of composites," *Composites Science and Technology*, vol.64 (9), pp.1331-1343, 2004.

[36] A. Hague, J. Krishnagopalan and S. Jeelani, "Fatigue damage in laminated composites," *Journal of Reinforced Plastics and Composites*, vol.12 (10), pp.1058-1069, 1993.

[37] A. Plumtree and G. Shen, "Prediction of fatigue damage development in unidirectional long fibre composites," *Polymers & Polymer Composites*, vol.2 (2), pp.83-90, 1994.

[38] M. Karama, L. Toubal and B. Lorrain, "Damage evolution and infrared thermography in woven composite laminates under fatigue loading," *International Journal of Fatigue*, vol.28 (12), pp.1867-1872, 2006.

[39] B.L. Lee and D.S. Liu, "Cumulative damage of fiber-reinforced elastomer composites under fatigue loading," *Journal of Composite Materials*, vol.28 (13), pp.1261-1286, 1994.

[40] H. Mao and S. Mahadevan, "Fatigue damage modelling of composite materials," *Composite Structures*, vol.58 (4), pp.405-410, 2002.

[41] K. Axouaoui, S. Rechak, Z. Azari, S. Benmedakhene, A. Laksimi and G. Pluvinage, "Modelling of damage and failure of glass/epoxy composite plates subject to impact fatigue," *International Journal of Fatigue*, vol.23 (10), pp.877-885, 2001.

[42] R. Steinberger, T.I. Valadas Leitao, E. Ladstatter, G. Pinter, W. Billinger and R.W. Lang, "Infrared thermographic techniques for non-destructive damage characterization of carbon fibre reinforced polymers during tensile fatigue testing," *International Journal of Fatigue*, vol.28 (10), pp.1340-1347, 2006.

[43] B. Liu and L.B. Lessard, "Fatigue and damage-tolerance analysis of composite laminates: stiffness loss, damage-modelling, and life prediction," *Composites Science and Technology*, vol.51 (1), pp.43-51, 1994.

[44] W. Van Paepegem and J. Degrieck, "Simulating damage and permanent strain in composites under in-plane fatigue loading," *Computers & Structures*, vol.83 (23-24), pp.1930-1942, 2005.

[45] J. Xiong, H. Li and B. Zeng, "A strain-based residual strength model of carbon fibre/epoxy composites based on CAI and fatigue residual strength concepts," *Composite Structures*, vol.85 (1), pp.29-42, 2008.

[46] S.J. Kim and I.H. Hwang, "Prediction of fatigue damage for composite laminate using impact response," *International Journal of Fatigue*, vol. 28 (10), pp.1334-1339, 2006.

[47] J.A. Epaarachchi and P.D. Clausen, "A new cumulative fatigue damage model for glass fibre reinforced plastic composites under step/discrete loading," *Composites Part A (Applied Science and Manufacturing)*, vol.36 (9), pp.1236-1245, 2005.

[48] Z. Gao, "A Cumulative damage model for fatigue life of composite laminates," *Journal of Reinforced Plastics and Composites*, vol.13 (2), pp.128-141, 1994.

[49] H.A. Whitworth, "Cumulative damage in composites," *Journal of Engineering Materials and Technology, Transactions of the ASME*, vol.112 (3), pp.358-361, 1990.

[50] W. Hwang and K.S. Han, "Fatigue of composites-fatigue modulus concept and life prediction," *Journal of Composite Materials*, vol.20 (2), pp.154-156, 1986.

[51] W. Hwang and K.S. Han, "Fatigue of composite materials – damage model and life prediction," P.A. Lagace, Ed., *Composite Materials: Fatigue and Fracture, ASTM STP 1012*, vol.2, pp.87-102, 1989.

[52] A. Conle and J.P. Ingall, "Effects of mean stress on the fatigue of composite materials," *Journal of Composites Technology & Research*, vol.7 (1), pp.3-11, 1985.

[53] Z. Gao and K.L. Reifsnider, "Strength degradation and fatigue failure of composites," *American Society of Mechanical Engineers, Applied Mechanics Division, Damage Mechanics in Engineering Materials*, vol.109, pp.179-190, 1990.

[54] A. Rotem, "The fatigue behavior of composite laminates under various mean stresses," *Composite Structures*, vol.17 (2), pp.113-126, 1991.

[55] M. Kawai and M. Koizumi, "Nonlinear constant fatigue life diagrams for carbon/epoxy laminates at room temperature," *Composites Part A*, vol.38 (11), pp.2342-2352, 2007.

[56] L.J. Broutman and S. Sahu, "A new theory to predict cumulative fatigue damage in fiberglass reinforced plastics," *Composite Materials: Testing and Design (Second Conference), ASTM STP 497*, pp.170-188, 1972.

[57] J. Noda, M. Nakada and Y. Miyano, "Fatigue Life Prediction Under Variable Cyclic Loading Based on Statistical Linear Cumulative Damage Rule for CFRP Laminates," *Journal of Reinforced Plastics and Composites*,vol.26 (7), pp.665-680, 2007.

[58] J. Andersons, M. Hojo and S. Ochiai, "Empirical model for stress ratio effect on fatigue growth rate in composite laminates," *International Journal of Fatigue*, vol.26 (6), pp.596-604, 2004.

[59] T. Fujii and Z. Maekawa, "Study on the fatigue of fiber reinforced composites based on the fatigue damage process of unit model," *Bulletin of the Japan Society of Mechanical Engineers*, vol.22 (164), pp.125-130, 1979.

[60] T.K. O'Brien, M. Rigamonti and C. Zanotti, "Tension fatigue analysis and life prediction for composite laminates," *International Journal of Fatigue*, vol.11 (6), pp.379-393, 1989.

[61] L.G. Melin, J. Schon and T. Nyman, "Fatigue testing and buckling characteristics of impacted composite specimens," *International Journal of Fatigue*, vol.24 (2-4), pp.263-272, 2002.

[62] M.S. Rosenfeld and L.W. Gause, "Compression fatigue behavior of graphite/epoxy in the presence of stress raisers," *Fatigue of Fibrous Composite Materials, ASTM STP 723*, pp.174-196, 1981.

[63] M.H. Beheshty, B. Harris and T. Adam, "An empirical fatigue-life model for high-performance fibre composites with and without impact damage," *Composites Part A (Applied Science and Manufacturing)*, vol.30A (8), pp.971-987, 1999.

[64] R. Ambu, F.Aymerich and F. Bertolino, "Investigation of the effect of damage on the strength of notched composite laminates by digital image correlation," *Journal of Strain Analysis for Engineering Design*, vol.40 (5), pp.451-461, 2005.

[65] J.C. Ha, A.T. Yokobori and H. Takeda, "The effect of fatigue damage on toughening of short-fiber-reinforced polymer composites," *Journal of Materials Science*, vol.34 (9), pp.2103-2111, 1999.

[66] D.D. Symons and G. Davis, "Fatigue testing of impact-damaged T300/914 carbon-fibre-reinforced plastic," *Composites Science and Technology*, vol.60 (3), pp.379-389, 2000.

[67] M. Mitrovic, H.T. Hahn, G.P. Carman and P. Shyprykevich, "Effect of loading parameters on the fatigue behavior of impact damaged composite laminates," *Composites Science and Technology*, vol.59 (14), pp.2059-2078, 1999.

[68] T.M. Krafchak, J-M. Petra, B.D. Davidson and G-S Chen, "Effect of impact damage on the compression fatigue behavior of composite tubes," in *Collection of Technical Papers - AIAA/ASME Structures, Structural Dynamics and Materials Conference*, vol.2, 1993, pp.859-866.

[69] D.G. Katerelos, A. Paipetis and V. Kostopoulos, "A simple model for the prediction of the *fatigue* delamination growth of impacted composite panels," *Fatigue and Fracture of Engineering Materials and Structures*, vol.27 (10), pp.911-922, 2004.

[70] N. Uda, K. Ono and K. Kunoo, "Compression fatigue failure of CFRP laminates with impact damage," *Composites Science and Technology*, vol.69 (14), pp.2308-2314, 2009.

[71] M. de Freitas and R. de Carvalho, "Residual strength of a damaged laminated CFRP under compressive fatigue stresses," *Composites Science and Technology*, vol.66, pp.373-378, 2006.

[72] G. Minak, P. Morelli and A. Zucchelli, "Fatigue residual strength of circular laminate graphite-epoxy composite plates damaged by transverse load," *Composites Science and Technology*, vol.69 (9), pp.1358-1363, 2009.

[73] O. Attia, A.J. Kinloch and F.L. Matthews, "The prediction of fatigue damage growth in impact-damaged composite skin/stringer structures. Part I: Theoretical modelling studies," *Composites Science and Technology*, vol.63 (10), pp.1463-1472, 2003.

[74] R. Butler, D.P. Almond, G.W. Hunt, B. Hu and N. Gathercole, "Compressive fatigue limit of impact damaged composite laminates," *Composites Part A (Applied Science and Manufacturing)*, vol.38 (4), pp.1211-1215, 2007.

[75] T. Yuanjian and D.H. Isaac, "Combined impact and fatigue of glass fiber reinforced composites," *Composites: Part B*, vol.39 (3), pp.505-512, April 2008.

[76] K.W. Kang and J.K. Kim, "Fatigue life prediction of impacted carbon/epoxy laminates under constant amplitude loading," *Composites Part A (Applied Science and Manufacturing)*, vol.35A (5), pp.529-535, 2004.

[77] K.W. Kang and J.K. Kim, "Fatigue life prediction for impacted carbon/epoxy laminates under 2-stage loading," *Composites Part A: Applied Science and Manufacturing*, vol.37 (9), pp.1451-1457, 2006.

[78] K.W. Kang and J.K. Kim, "Fatigue life prediction of impacted glass/epoxy composites under variable amplitude loading," *Key Engineering Materials*, vol.261-263 (2), pp.1079-1084, 2004.

[79] B. Harris, N. Gathercole, J.A. Lee, H. Reiter and T. Adam, "Life-prediction for constant-stress fatigue in carbon-fibre composites," *Philosophical Transactions of the Royal Society London, Series A (Mathematical, Physical and Engineering Sciences)*, vol.355 (1727), pp.1259-1294, 1997.

[80] M.H. Beheshty and B. Harris, "A constant-life model of fatigue behaviour for carbon-fibre composites: the effect of impact damage," *Composites Science and Technology*, vol.58 (1), pp.9-18, 1998.

[81] G.P. Horn, T.J. Mackin and P. Kurath, "Estimating the residual fatigue lifetimes of impact-damaged composites using thermoelastic stress analysis," *Polymer Composites*, vol.22 (3), pp.420-431, 2001.

[82] G. Horn, T.J. Mackin and P. Kurath, "Estimating residual life of polyurethane composites using thermoelasticity," in *Nondestructive Evaluation (NDE) and Materials Properties IV. Proceedings of the TMS Symposium*, 1999, pp.11-14.

[83] *Instron 8800 Materials Test Control System Operating Instructions*, Instron, rev.A, 2000.

[84] *Instron Fast Track 8800 Materials Test Control System*, Instron, rev.A, 1998.

[85] "Compression Platens – Fixed and Spherical Seat," [Online document]. Available: http://www.wyomingtestfixtures.com/Products/b12.htm, 2005 [April 14, 2010].

[86] *ARAMIS v6 User Manual – Software*, GOM mbh, rev.C, 2007.

[87] *System 7000 Instruction Manual*, Vishay, February 2007.

[88] "System 7000," [Online document]. Available: http://www.intertechnology.com/Vishay/pdfs/System_7000.pdf, n.d. [April 14, 2010].

[89] *ASTM Standard D7136, Standard Test Method for Measuring the Damage Resistance of a Fiber-Reinforced Polymer Matrix Composite to a Drop-Weight Impact Event*, ASTM, 2005.

[90] *ASTM Standard E1038, Standard Test Method for Determining Resistance of Photovoltaic Modulus to Hail by Impact with Propelled Ice Balls*, ASTM, 2005.

[91] *ASTM Standard D6641, Standard Test Method for Determining the Compressive Properties of Polymer Matrix Composite Laminates Using a Combined Loading Compression (CLC) Test Fixture*, ASTM, 2001.

[92] *ASTM Standard D7078, Standard Test Method for Shear Properties of Composite Materials by V-Notched Rail Shear Method*, ASTM, 2005.

[93] *793 Control Software 100-147-130B*, MTS, 2008.

[94] *SCXI Chassis User Manual and Specifications*, National Instruments, April 2006.

[95] *ASTM Standard D7137, Standard Test Method for Compressive Residual Strength Properties of Damaged Polymer Matrix Composite Panels*, ASTM, 2005.

[96] *MIL-HDBK-17-1F, Composite Materials Handbook: Volume 1.Polymer Matrix Composites Guidelines for Characterization of Structural Materials*, US Department of Defense, 2002.

[97] *MIL-HDBK-17-2F, Composites Materials Handbook: Volume 2. Polymer Matrix Composites Materials Properties*, US Department of Defense, 2002.

[98] S.C. Tan, *Stress Concentrations in Laminated Composites*. Lancaster, Pennsylvania: Technomic Publishing Company Inc., 1994, pp.126.